Investigation of *In-vivo* Integument Mechanics for Device Design at the Bio-mechanical Interface

by

Dory Y. Yang

A dissertation submitted in partial fulfillment
of the requirements for the degree of
Doctor of Philosophy
(Mechanical Engineering)
in the University of Michigan
2023

Doctoral Committee:

Assistant Professor K. Alex Shorter, Chair
Assistant Professor Jesse Austin-Breneman
Associate Professor Kira Barton
Assistant Professor Jon Estrada
Professor Susan E. Parks

Ya-Yu Yang
yangyayu@umich.edu
ORCID iD: 0000-0001-8390-8935

DEDICATION

To my husband, Ken, who has walked every step of this journey with me;
and Tokitae, whose courageous and resilient spirit keeps me going.

ACKNOWLEDGMENTS

The past seven and a half years at the University of Michigan have constituted a profoundly invaluable period in my life. Reflecting back to the spring of 2015 when I first received the admission letter from the Mechanical Engineering Department, I could not have foreseen the extent of personal and academic growth that awaited me. Through these years, Ann Arbor has seamlessly transformed into a second home.

In this regard, I extend my sincere acknowledgment to my esteemed committee members: Assistant Professor K. Alex Shorter, Assistant Professor Jesse Austin-Breneman, Associate Professor Kira Barton, Assistant Professor Jon Estrada, and Professor Susan E. Parks. I am immensely grateful for your unwavering support and insightful guidance. Your invaluable suggestions and counsel have consistently refined and polished my work. A special note of appreciation goes to Alex and Kira for fostering an environment of openness and support within the laboratory, enabling me to cultivate independence and confidence.

The journey has been arduous, compounded further by the global pandemic that transpired midway. I extend heartfelt gratitude to Alex for consistently reminding me to infuse a sense of enjoyment into research despite the challenges and frustrations.

I extend my gratitude to all the collaborators who have been part of this journey. To Xiran and Will, your foundational work on the PDIC project is deeply appreciated. I am thankful to Andy, Riley, and Daniel, the members of the suction cup squad, for their invaluable assistance on the suction cup kinetic project. A special mention to Gabriel for your indispensable knowledge and support in constructing the pressure tag; the project's rapid progress owes much to your contributions. Ethan and Rodney, your aid in the manufacturing and assembly of the pressure tag is deeply acknowledged. Joaquin, your support in conducting tow tank experiments and sharing your wisdom about the essence and duty of an engineer is truly appreciated. I must also express my gratitude to the wonderful labmates from ESTAR and BRG – your camaraderie has been an invaluable asset.

Finally, my heartfelt gratitude extends to my husband, Ken. Your unwavering presence throughout this incredible journey has been my anchor, providing both stability and courage to push boundaries and pursue my aspirations. Words fall short in describing the scale of support you have provided. To my four-legged companions, Nori, Uni, and Ikura, your presence has brought immeasurable joy and solace to my days.

TABLE OF CONTENTS

LIST OF FIGURES

FIGURE

LIST OF TABLES

TABLE

LIST OF APPENDICES

LIST OF ABBREVIATIONS

CFD computational fluid dynamics

COM center of mass

CT computerized tomography

DIC digital image correlation

DMA dynamic mechanical analysis

EMG Electromyography

FBD Free body diagram

FFT fast Fourier transform

FPS frames per second

IFFT inverse fast Fourier transform

IMU inertial measurement unit

PDIC portable digital image correlation

SD standard deviation

SLS standard linear solid

SSCup static suction cup

wrt with respect to

LVDT linear variable differential transformer

UAV unmanned aerial vehicle

ABSTRACT

The term ”bio-mechanical interface” describes a surface where a living biological system comes into contact with a mechanical apparatus. Due to the force interaction and impedance mismatch between the two, the biological counterpart can often experience varying levels and duration of discomfort. To lessen discomfort, the two major approach is to either adjust contact condition or adapt behaviors. Among bio-mechanical interfaces, wearable sensors are increasingly gaining public attention. As the technology continually improves, these embedded systems that can be fixed directly to the body are getting smaller, more powerful, efficient, and present in our everyday lives.

Bio-logging tags are a specific category of wearable sensors used to track and study animals across different habitats, which have been especially valuable for behavioral observation of cetaceans, animals who spend the majority of their lives under water and range widely in the open ocean. For the last 20 years, suction cups have been used widely to attach short-term bio-logging tags to marine animals including whales, dolphins, and turtles. Suction attachments are especially excellent in cases where the recording longevity of the tag, the size or state-of-health of the study animal, or the need to recover the tag, make long-term invasive tagging inappropriate. These suction cup tags can be applied to free-swimming animals using poles or ballistic delivery, and the uniformly smooth surface of many marine mammals make suction cup attachments ideal for these animals. The lack of integument penetration at the attachment site, and the capability to deliver tags to many species without the need for capturing individuals, make suction cup tags a critical tool for minimally invasive research.

However, in both field studies and from the collected data, tag issues such as early detachment, sliding from the original spot, or animals actively trying to get rid of the tag are common. These phenomena not only significantly affect the reliability of the collected data, but also raise questions about how much disturbance these tags cause and how the suction cup design can be improved.

This dissertation focuses on the following research questions: **Q1**: *How does cetacean skin response to vacuum loading?* **Q2**: *What are the reasons that cause a suction cup to fail?* **Q3**: *How to improve suction cup design to achieve 24-hour attachment, minimal relative motion and lessen discomfort?*

As a bio-mechanical experimentalist, I tackle these research questions in my PhD work. I

begin by creating a custom optical measurement instrument called the PDIC (Portable Digital Image Correlation) system, which enables *in-vivo* investigation of cetacean integument. Using this system, I extract the viscoelastic properties of the skin and identify the parameters necessary for a viscoelastic model that can accurately capture the skin's deformation response under vacuum loading.

Following this, I establish a generalized kinetic model for suction cups and characterize their attributes, including linear stiffness and area composition. I then conduct experiments to test different suction cup designs and determine their corresponding loading limits before failure.

Utilizing the new knowledge gained from the in-lab investigation, I integrate pressure transducers into bio-logging tags to create a new device, pressure-logging tag, that can monitor suction cup states in the real world.

My work will conclude with a proposed suction cup design framework, which includes key decision variables, environmental parameters, and performance indices that can serve as a foundation for improving suction cup design for the future.

CHAPTER 1

Introduction

1.1 Contact Surfaces and Human Civilization

Force interaction and impedance mismatch are two shared features which found between most of contact surfaces. These two features, while seemingly ordinary and taken for granted, have been key to the development of human civilization.

Carving with stones, the *Homo ergaster* ('Working Man') lived 1.5 million years ago created the pioneering awls and polished bone points excavated from the Blombos Cave, Africa [28, 29, 30, 31] (Figure 1.1 (A)). Grinding grain with Olynthus Mill (Figure 1.1 (B)) in ancient Greece enabled the food processing and preservation which allow humans to flourish under agriculture-based permanent settlements [32]. Mastering the metal forging technique with experiences accumulated over the span of thousands of years, medieval blacksmiths applied fire and hammer to reshape stiff metal to create the iconic plate armor made of jointed sheet metals which complied to human body shape for protection (Figure 1.1 (D)). Quickly rolling forward to the Industrial Revolution in the 18^{th} century, steam driven belt and pulley systems (Figure 1.1 (C)) powered factories and modernized that generation. Now with human history passing the 2^{nd} millennium, we live in the era where space travel is no longer a plot in sci-fi movie. With computers doing the precise and complex modeling and simulation on the hydrodynamic impulses generated during landing between the rocket and launch station, Falcon 9 (Figure 1.1 (E)), the first-ever reusable rocket, marks a magnificent milestone of human civilization.

All the achievements above would not be possible without understanding the force interaction and impedance difference between objects in contact. Studying and utilizing the knowledge of contact surfaces provides the foundation for the technology today and the new chapter for tomorrow.

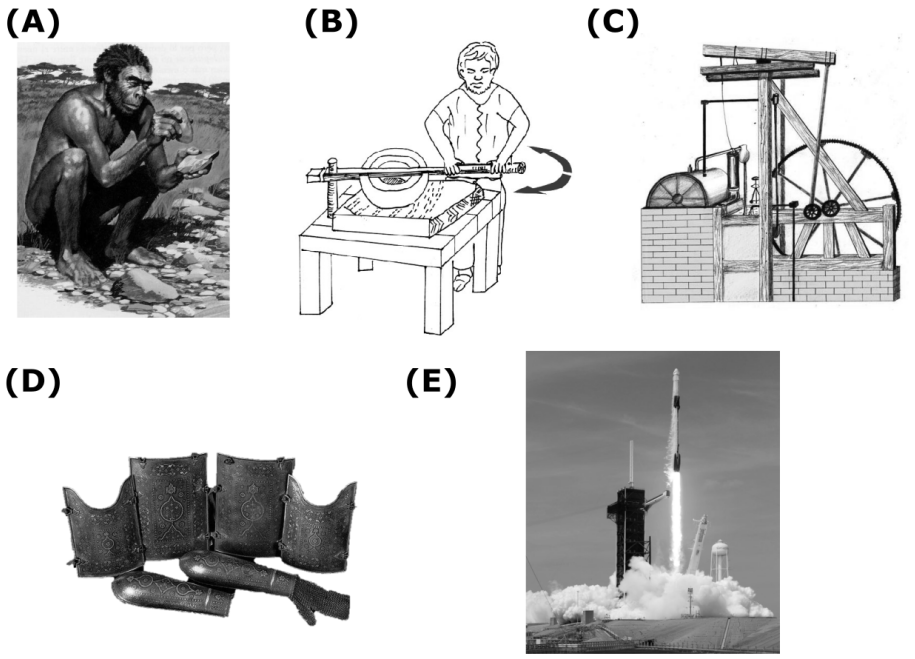

Figure 1.1: Contact surfaces examples: (A) *Homo ergaster* ('Working Man') using bone awls and points [1]; (B) Olynthus Mill invented in ancient Greece [2]; (C) Plate armor in medieval era [3]; (D) Steam driven belt and pulley systems widely used to power factories during Industrial Revolution[4]; (E) Falcon 9 launched [5].

1.2 Bio-mechanical Interfaces

Among all types of contact surfaces, bio-mechanical interface is a specific category where a living biological system interacts with a mechanical apparatus. Examples can be found everywhere in the daily life, including: the interface between our feet and the shoes we wear, the plaster cast around a broken arm (Figure 1.2 (B)), and dental implants surrounded by the gingival tissue, to name just a few. Animal examples including horseshoe and horse hoof (Figure 1.2 (E)), ear tags on livestock (Figure 1.2 (D)), or as simply as the Elizabethan collar our pets wear after the spay/neuter surgery. For these bio-mechanical interfaces, force interaction and impedance mismatch are particularly critical since they can oftentimes cause discomfort to the biological side of the system.

The level and longevity of discomfort vary depending on the characteristics of each bio-mechanical interface. It can be as minor as the itchiness caused by a clothing label rubbing against our neck or the temporary pain our pets feel when vets inject microchips into their bodies. Or it can be severe and chronic, like the irritation and ruptured skin of an amputee due to repetitive movements between their compliant residual limbs and the much stiffer prosthetic sockets (Figure 1.2 (C)), or the infectious and even fatal fishhook injuries on sea animals (Figure 1.2 (F)). In short, the

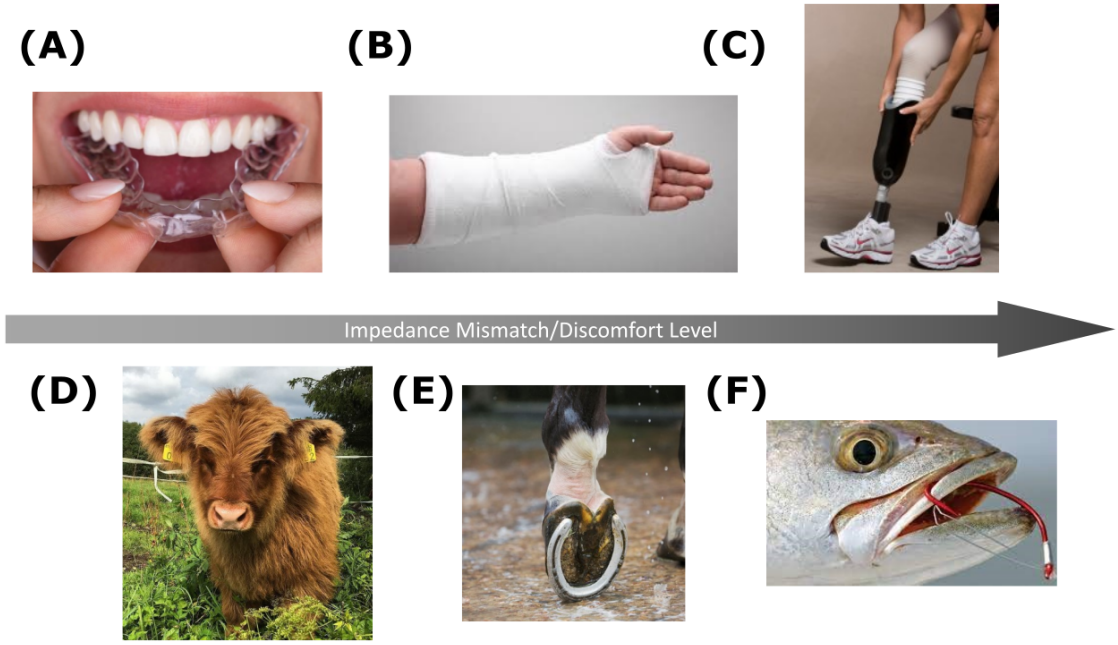

Figure 1.2: Bio-mechanical interface examples for humans: (A) Teeth aligner and teeth [6]; (B) Plaster cast around a broken arm [7]; (C) Prosthetic socket versus residual limb [8] and animals: (D) Livestock wears ear tags [9]; (E) horseshoe on horse hoof [10] (F) Fish hook injury [11].

combination of an impedance mismatch at the bio-mechanical interface between a hard device and soft tissue, and forces created by relative movement between the surfaces can create discomfort and damage tissue.

To lessen discomfort, humans often try to change the conditions at the bio-mechanical interface, for example, we can use shoe stretcher, add padding, wear socks, or just change to a half-size larger when we find the fit of our new boots are a bit off. As for animals, they adjust their behavior intuitively to lessen discomfort, which explains why our dogs roll on and move on the ground in a variety of ways just to get a raincoat off of themselves. Nevertheless, adapted behaviors are undesirable for the case of wearable sensors, a specific type of bio-mechanical interfaces where the main purpose is to monitor the natural behaviors of the subjects.

Wearable sensors are increasingly gaining public attention. As the technology continually improves, these embedded systems that can be fixed directly to the body are getting smaller, more powerful, efficient, and present in our everyday lives ((Figure 1.3)). While it might take an hour or two for us human to get used to the extra gadgets on our bodies. It's another story when scientists try to put these tracking devices on to animals, who oftentimes intuitively adjust their behaviors to remove the external disturbances applied on them, which in turns greatly influence the relia-

bility of the collected data. Therefore, studying and understanding the bio-mechanical interfaces between the device and animal is particularly important in the current era where wearable sensors are prospering.

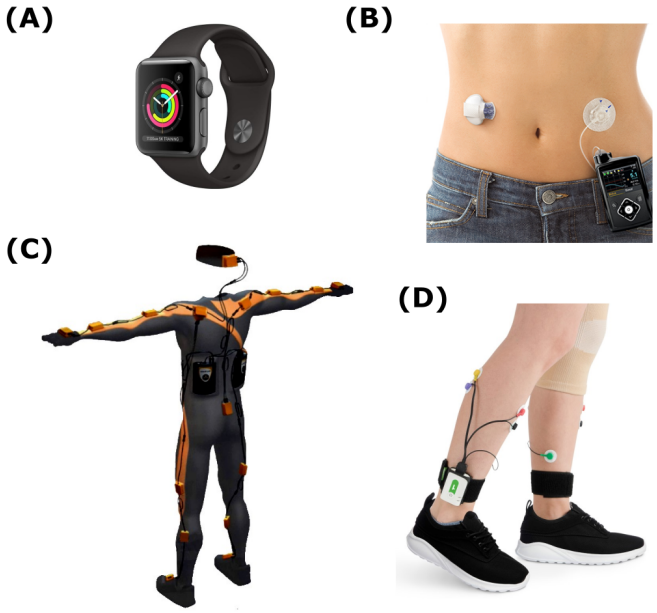

Figure 1.3: Wearable sensor examples for human (A) Apple watch incorporates fitness tracking, health-oriented capabilities, and wireless telecommunication [12]; (B) Continuous glucose monitor (CGM) measures the interstitial glucose level, which is the glucose level found in the fluid between the cells [13]; (C) Xsense MVN is a full-body human motion capture suit equipped with IMU, biomechanical models and sensor fusion algorithms [14]; (D) NeuroSoft Steadys is a gait assessment tool based on IMU and EMG [15].

1.3 Suction-based Bio-logging Tags for Cetaceans

Bio-logging tags refer to animal-borne wearable sensors that are used to record and/or transmit data about animal movement, physiology, or the environment [33]. They have become an increasingly popular tool for the investigation of animal behavior and locomotion in their natural habitat over the past decades [34]. The sensors on board including but not limited to GPS [35, 36], accelerometer [37, 38, 39], gyroscope [40, 41], magnetometer [42], thermometer [43, 44], pressure transducer [45], heart rate monitor [46], light sensor [47], and hydrophone [48]. Bio-logging tags come in different shapes and forms which create bio-mechanical interfaces with distinctive characteristics. Figure 1.4 showcases some examples, such as the collar-type used on terrestrial animals (koala and wolf in Figure 1.4 (A)) and harness and backpack-style worn by flying animals (bat and bird

in Figure 1.4 (B)). As for marine animals, it can be further divided into short-term tags secured non-invasively to the animals via glue or suction (seal in Figure 1.4 (C) top), and long-term tags that require invasive methodology to anchor the tag onto animals (squid in Figure 1.4 (C) bottom).

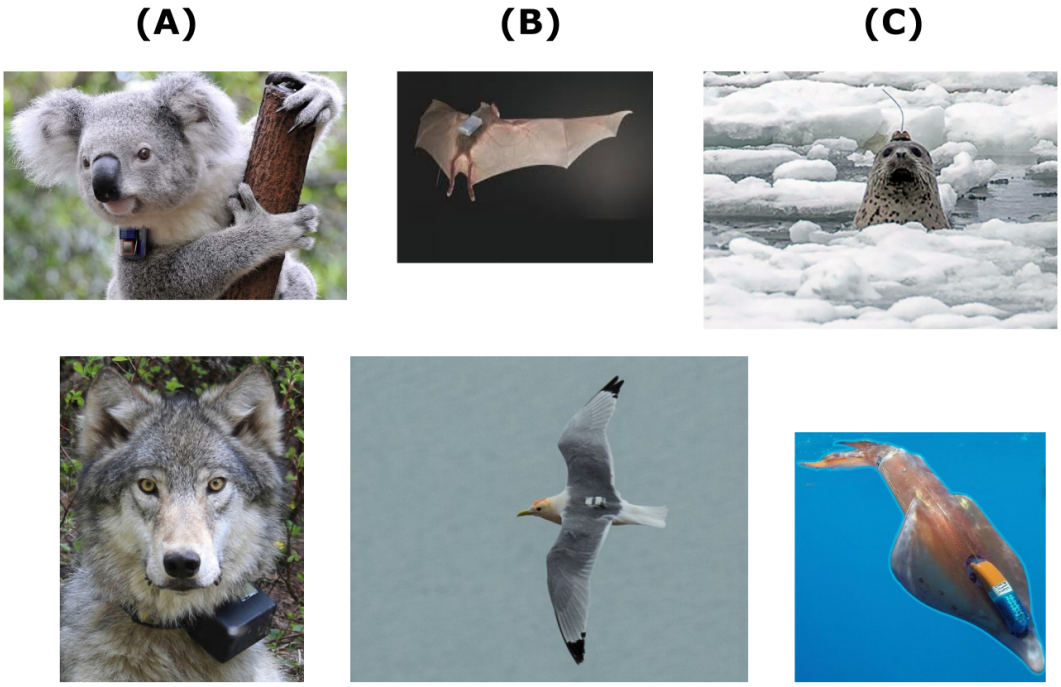

Figure 1.4: Bio-logging tag examples: (A) Terrestrial animals wearing collar-type bio-logger [16, 17]; (B) Aerial animals with harness and backpack-style trackers [18, 19]; (C) Bio-logging tags for aquatic animals can be either short-term (non-invasive) [20] or long-term (invasive) tracking [21].

Bio-logging tags have been especially valuable for behavioral observation of cetaceans, animals that spend the majority of their lives under water and range widely in the open ocean. Various types of bio-logging tags have been developed to collect and store high-resolution sound, image and motion data for intervals of hours to days [49, 50, 51]. Figure 1.5 (C) showcases a bottlenose dolphin (*Tursiops truncatus*) wearing a representative bio-logging tag, Mtag, which was designed and manufactured by our research group, Embedded System for Tracking and Robotics (ESTAR), at the University of Michigan, to monitor dolphin kinematics, and is secured to the animal using four suction cups.

Suction cups have been used widely for the last 20 years to attach short-term bio-logging tags to marine animals including whales, dolphins, and turtles [52, 53]. Suction attachments are especially excellent in cases where the recording longevity of the tag, the size or state-of-health of the study animal, or the need to recover the tag, make long-term invasive tagging inappropriate. These tags can be applied to free-swimming animals using poles (Figure 1.5 (B)) or ballistic delivery, and the

uniformly smooth surface of many marine mammals make suction cup attachments ideal for these animals. The lack of integument penetration at the attachment site, and the capability to deliver tags to many species without the need for capturing individuals, make suction cup tags a critical tool for minimally invasive research.

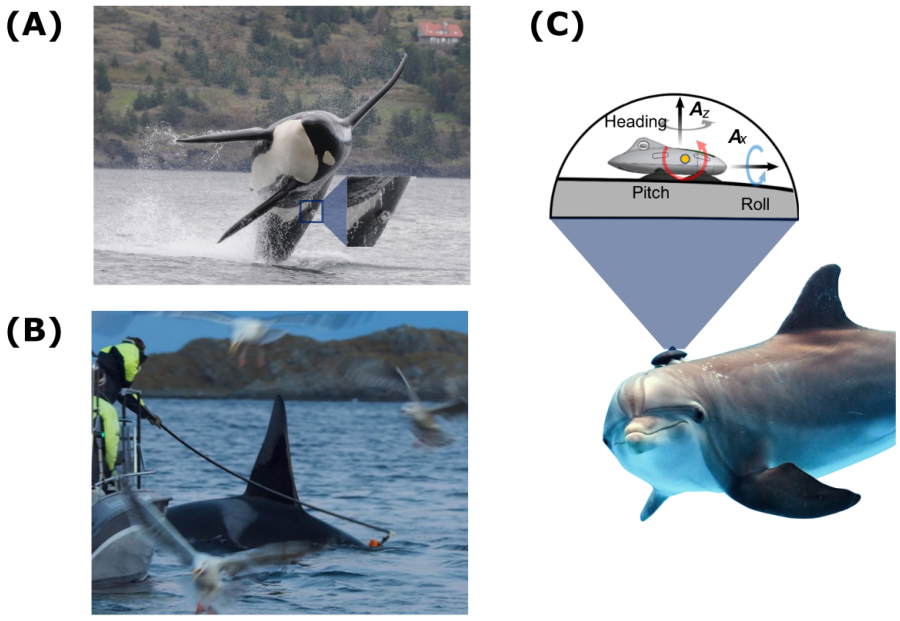

Figure 1.5: Suction cup bio-logging tag: (A) An orca wearing a suction cup bio-logging tag [22]; (B) A biologist using a pole to attach a suction cup bio-logging tag [23]; (C) A bottlenose dolphin (*Tursiops truncatus*) wearing a M-tag with an enlarged view of the tag.

Suction cups used with bio-logging tags attach to an animal's integument (compliant substrate) by generating a pressure differential (ΔP) between the environment (p_o) and the cup interior (p_v), to create the vacuum force (F_V) that holds the tags in place. Figure 1.6 illustrates how a cup is attached. Initially, an external setup force (F_{setup}) is applied to deform the cup and expel most of the fluid inside by flattening the cup body on to the substrate (Figure 1.6 (Middle)). The elastomeric material and the shape deformation of the cup act like a spring and store energy. Once F_{setup} is removed, the stored energy will act to restore the cup to its undeformed configuration. At the same time, the lip acts as a check valve preventing ingress of the surrounding fluid. The seal at the lip and the increasing internal volume resulting from cup body relaxation create a reduced p_v and correspondingly increase ΔP as well as F_V.

Meanwhile, on the biological side of the system, subjected to the influence of ΔP, the compliant substrate (integument) deforms into the suction cup, reducing the internal volume of the cup. This

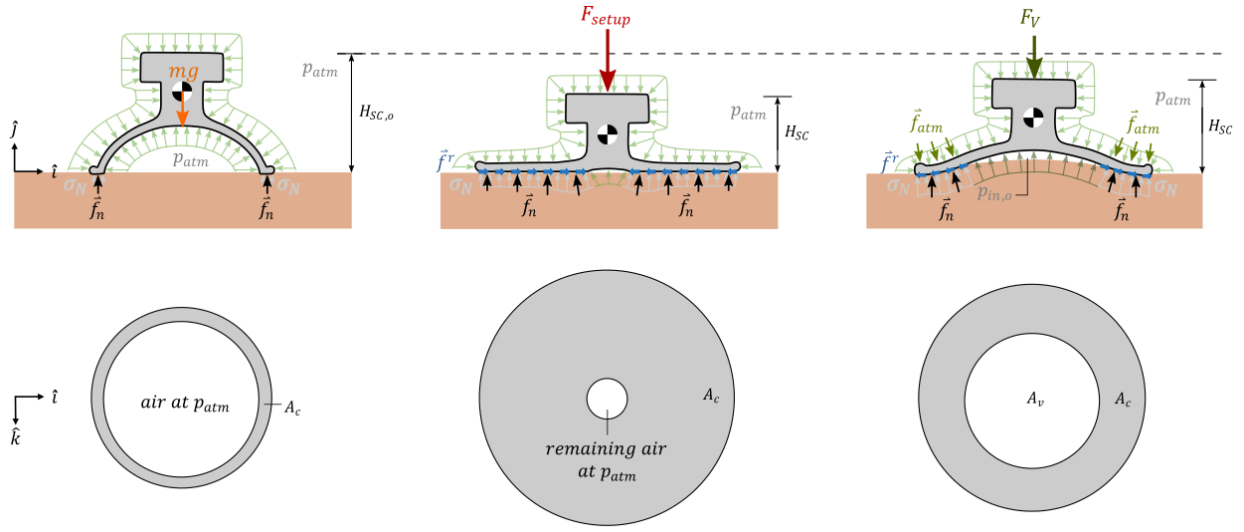

Figure 1.6: The procedure of setting up a suction cup on a compliant substrate contains the three following steps: **(Left)** Place the suction cup on the substrate, the weight of suction cup (mg) is supported by the normal force (N) from the initial contact area; **(Middle)** Apply setup force (F_{setup}) to expel most of the air inside suction cup; and then **(Right)** Release F_{setup}, while suction cup works on recovering its' original shape, the expansion of the cavity on the interface generates pressure differential (ΔP) which results in a vacuum force (F_V) (attachment force, F_A) pushing suction cup down and preventing it from further restoration. A_v and A_c refers to the vacuum area in the middle and the surrounding contact area, respectively.

results in a smaller pressure differential (ΔP) and a reduced attachment force (vacuum force, F_V). The internal volume of the cup continues to change until the bio-mechanical interface between the suction cup and substrate reaches a force equilibrium, which we defined as the initial setup state (Figure 1.6, right). The contact surface is divided into the circular vacuum area (A_v) in the middle where the integument is deformed and the surrounding contact area (A_c) where the integument is in contact with the suction cup lip. At this state, a force equilibrium is reached between F_V acting on A_v and the normal stress ($\overrightarrow{f}_n$) and atmospheric force ($\overrightarrow{f}_{atm}$) on A_c. Figure 1.6 presents the schematic showcasing the setup procedure of a suction cup on compliant substrate.

1.4 The Material Science of Integument (Skin)

The performance of a suction cup is greatly affected by the properties of the integument. Formally called "integumentary system", by anatomy definition, it refers to the set of organs which forms the outermost layer of an animal's body which comprises the skin (epidermis and the dermis) and its appendages (hypodermis).

From inside out, hypodermis, also known as the subcutaneous layer, sits under the skin. It acts as an energy reservoir and heat insulator. For cetacean, this layer contains blubber and fat for thermoregulation. Above hypodermis is skin, a composite organ, made up of at least two major layers of tissue: the dermis and the epidermis [54]. Dermis is above hypodermis, which contains connective tissues, vessels, glands, follicles, hair roots, sensory nerve endings, and muscular tissue [37]. On the top is epidermis (stratum corneum/ spinosum/ germinativum), which is the outermost layer serving as the initial barrier to the external environment. This is the layer that suction cups are in direct contact with. For cetacean, their epidermis features ridged texture [24] and can fully slough off every 2-4 hours, which pose a big challenge for suction-based attachment. For simplification, the term "integument" and "skin" will be treated equally and used interchangeably in this dissertation.

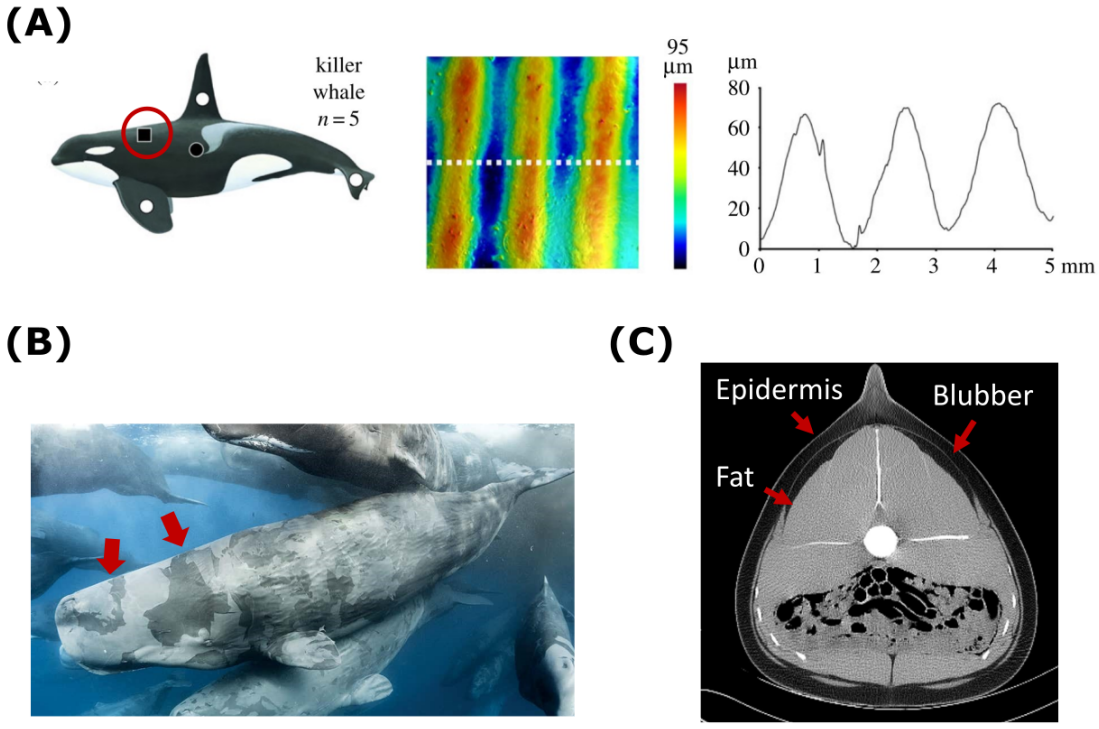

Figure 1.7: Cetacean Integument features **(A)** ridged texture [24] and **(B)** constant shedding [25]; (C) CT scan of a dolphin, showcasing the layer compositions of its' integument.

The skin possesses both viscous and elastic (viscoelastic) properties [55, 56] which exhibits a nonlinear stress-strain relationship during loading [57]. With different tissues non-uniformly distributed and highly integrated into layers, skin is a complicated composite which may simultaneously features anisotropicity, nonhomogeneousity and viscoelasticity. Meaning its material

properties might be directional, non-uniform and time dependent. These material properties affect how cetacean skin responds to vacuum loading and will impact suction cup performance accordingly. The ability to characterize viscoelastic properties of cetacean skin is therefore critical for both gaining a better understanding of the basic anatomy of these animals and facilitating the design of bio-logging tags that are placed in direct contact with their skin [58, 59, 60].

1.5 Challenges on the Suction Cup - Skin Interface

Suction cups are widely used for securing bio-logging tags onto compliant cetacean skin for its easy-to-apply/retrieve and non-invasive features. These suction cups are made of various types of elastomer materials which are much stiffer than the skin substrate. When a stiffer suction cup attaches to a compliant skin, it generates F_V by creating ΔP via its own shape change, which in turns load and deform the viscoelastic skin composite to reach a force equilibrium of the coupled system (Figure 1.6 (Right)). The dynamics of the bio-mechanical interface is therefore resulted from the force interaction and the impedance mismatch between the suction cup and the skin. To better illustrate the dynamics between the two, the suction cup – skin coupled system can be simply-analogized as two springs in series. The suction cup has a larger spring constant, meaning it is stiffer, whereas skin is more compliant with a smaller spring constant (Figure 1.8 (A)). The magnitude of F_V has a positive correlation to the stiffness of the suction cup. In the case of a two-spring-in-series system, the less stiff spring (skin) will take on most of the deformation, which will lead to the major drawbacks of the suction-based attachment approach.

If F_V created by the cup is continuing to deform skin substrate to a certain level, it may cause discomfort and result in modified animal behaviors. This includes the animals actively working to remove the bio-logging tags by breaching or rubbing the tag off on other animals or the ocean floor. The continued loading and skin deformation could also lead to capillary rupture and bruising. As shown in Figure 1.8 (B), there is a visible skin irritation mark at each cup site after an 8-hour tag deployment. These cup 'foot-prints' are composed of two areas introduced in the Figure 1.6, A_v, the center circular area where F_V acts and A_c, the surrounding area where the skin is in contact with the cup lip. Discoloration at the cup sites has been observed for more than 48 hours after day scale tag deployments. On the flip side, if F_V is too small, hydrodynamic forces (induced by animal locomotion) acting on the tag become large enough to push the tag down the length of the body and off the animal. Both cases are undesirable since they result in a premature detachment of the tag from the animal or the unreliable behavior data.

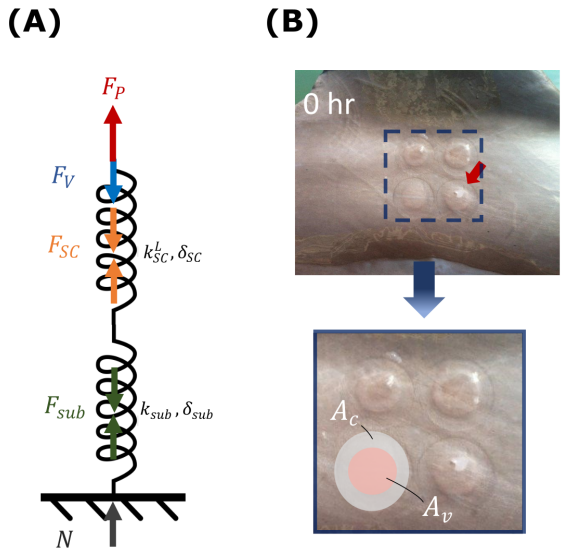

Figure 1.8: Biomechanical interface between suction cup and compliant skin (integument) can be simply analogized as (A) Two-spring-in-series system, with the suction cup has a larger spring constant (k_{SC}^L), meaning stiffer, than the integument underneath (k_{sub}); (B) Skin irritation, the suction cup footprint" is composed of two areas: A_v where F_V acts on and the surrounding A_c where the skin is in contact with the cup lip.

1.5.1 Suction Cup: Evolution, Variations and Applications

Suction cups have existed in human history for a very long time, with the first one said to be originally invented by Hippocrates in 3_{rd} century B.C as an important tool for the practice of medicine. Made of gourds, these suction cups were attached to patients' skin and believed to supposedly draw bad blood away from diseased organs to the surface of the body. Similar medical practices were developed across multiple cultures and time spans, which evolves into a part of modern myofascial treatments called cupping therapy [61]. In addition to its benefits in medicine, human use suction cups for a wide range of applications, such as vacuum hook, breast milk pumping, toilet plunger, glass suction lifter... etc. To fulfill functions of each application, suction cups come in various designs, including shapes, materials, and surface textures... etc., as shown in Figure 1.9 (A).

Apart from the variation in design, suction cups work under the same principle, which is generating a negative pressure differential (ΔP) between the environment (p_o) and inside cavity (p_v) to resist external loading. Based on this, a suction cup can be structurally divided into three components. First is "bell", the deformable hollow architecture which can be compressed to create ΔP either actively or passively. Second is "lip", which refers to the outer edge of the cup and the partial interior wall of the bell in contact with the substrate (A_c) which greatly influences the

forces generated on the interface. Last is the "neck", the connector between the suction cup and other devices, it is usually where the external loading is applied (Figure 1.9 (B)).

Figure 1.9: Although suction cups come in various material, shape, and design ((A) [26]) to fulfill specific functionalities, they share three common structures, which are bell, lip and neck ((B)).

In contrast to the abundant history and the variety of suction cups, the related research is surprisingly scarce due to many of them are merchandise protected by patents. Among the published suction cup-related studies, the dominant research interest surrounds using suction cup with robots. For example, the arrangement of vacuum grippers in manufacturing/ packaging robots [62] and the end-effecter of wall climbing robots [63, 64, 65, 66]. Both cases are using active vacuum to maintain ΔP to interact with low-compliant non-biological objects/ systems where impedance difference and force interaction aren't the major concerns, and thus unfortunately shares no common ground with our case of using suction cup on cetacean integument.

Cupping therapy massage (a.k.a. myofascial decompression) is the only case found in literature which explores the application of suction on compliant substrate (skin) [61, 67, 68]. Nevertheless, this therapy is meant to induce skin irritation and bruises as part of the treatment. Therefore, the related studies are more medical-oriented, rather than investigating the bio-mechanical interaction between skin and suction cup. To conclude, our application of using suction cup to secure bio-logging tag (a mechanical object) on fast swimming cetaceans (compliant biological system) is unlike the existing applications and studies from many perspectives.

To conclude, there is no existing model describing the interaction between suction cup and compliant substrate, and the relationship between suction cup deformation with respect to its' ability to resist external loading are not fully understand nor quantified. Therefore, in order to improve future suction-based bio-logging tag design for cetacean behavior studies, characterizing

suction cup performance on compliant substrate and building a generalized suction cup-skin kinetic model become essential tasks.

1.6 Scope and Structure of This Dissertation

The work presented in this dissertation aims to create a new framework on how to approach these bio-mechanical interface design problems in a systematic and comprehensive manner. The application addressed in my PhD work is the suction-based bio-logging tag on cetacean integument (skin). The research objective is to generate new knowledge about *in-vivo* skin mechanics and apply these insights to better understand the bio-mechanical interface between cetacean skin and minimally invasive bio-logging systems. This improved understanding will lead to new designs for the suction cup attachment systems used to secure the bio-logging tags to cetaceans and other marine mammals alike.

Three research questions are addressed in this work:

Q1: *How does cetacean integument (skin) response to vacuum loading?*

Q2: *What are the reasons that cause a suction cup to fail?*

Q3: *How to improve suction cup design to achieve 24-hour attachment, minimal relative motion and lessen discomfort?*

To gain the knowledge to fulfill my research objectives, this work spans three areas (initial investigation on both cetacean integument and suction cup, skin characterization and modeling, suction cup examination) showcased in the flowchart (Figure 1.10). Specifically, in this dissertation I will:

Firstly, showcase the preliminary experimental insights regarding cetacean integument features and suction cup performance against different substrate compliance in Chapter 2. Followed by the further investigation of the response of cetacean skin to vacuum loading using a novel experimental approach I developed. The custom instrumentation will be used to quantify the viscoelastic properties of the skin, and to identify parameters for a viscoelastic model that captures deformation response under vacuum loading. The system and the pilot study results will be illustrated in Chapter 3. With the new knowledge about cetacean skin, the generalized suction cup kinetic model I proposed is presented in Chapter 4. Along with the 2 pioneering suction cup characterization studies and 3 sets of quantitative experiments analyzing suction cup performance versus substrate impedance and loading conditions from both the kinematics and kinetics perspectives. Next, Chapter 5 will introduce the real-world loading boundary (performance envelope) identification under

hydrodynamic setting using a novel pressure-logging device assisted with computational fluid dynamics (CFD) modeling. Finally, combine knowledge gained from the above two research areas (*in-vivo* cetacean integument investigation and suction cup kinetic/kinematic modeling & analysis), the dynamics of the skin-suction coupled system is better understood. As succeeding work, with the identified key design variables, I proposed a framework to tailor and improve suction cup performances to achieve specific desired requirements. The dissertation wraps up with synthesis of research contributions and broader impacts as well as discussion of future directions in Chapter 6.

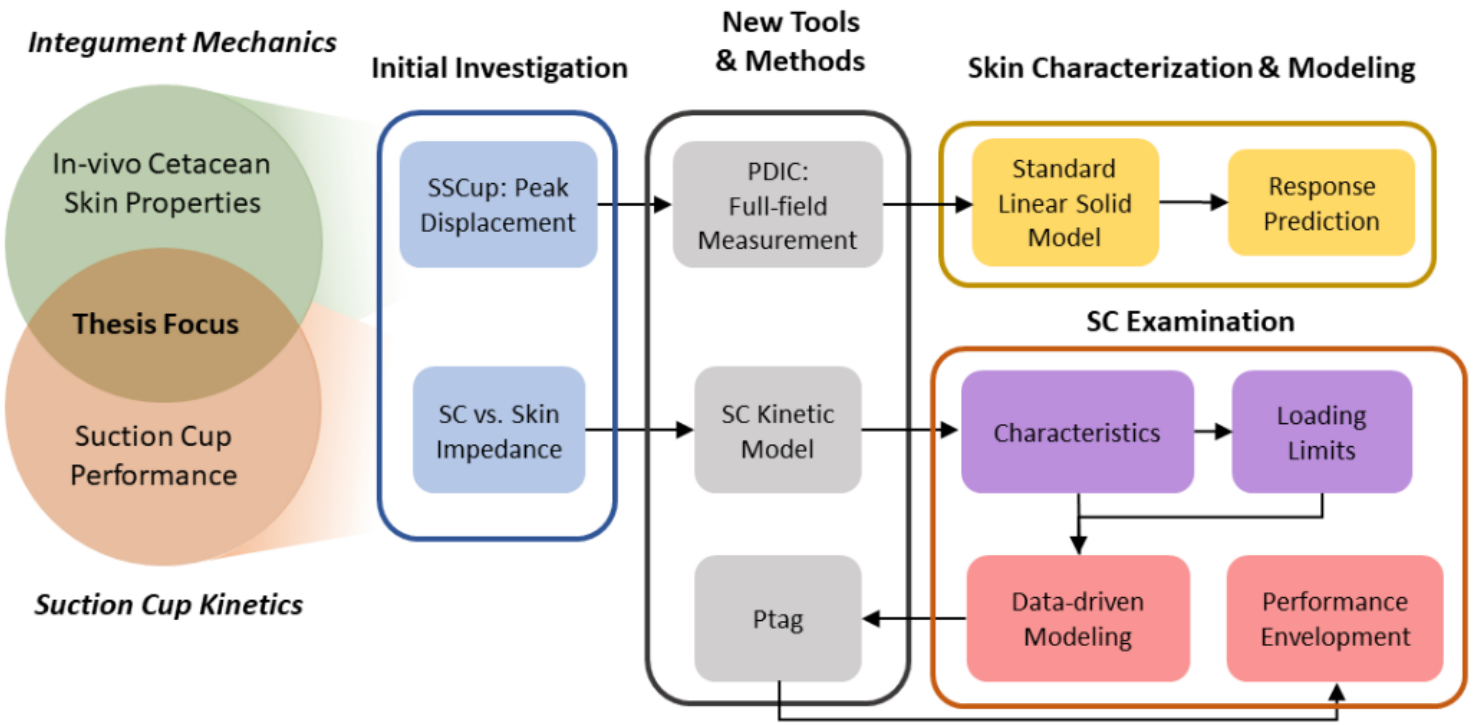

Figure 1.10: The schematics showcases the scope (Left) and the structure (Right) of this dissertation. This dissertation is at the intersection of *in-vivo* cetacean integument investigation and suction cup performance examination. The work leverages new tools and methods to model the kinetics and kinematics on the biomechancal interface between cetacean integument and the suction cups of bio-logging tag. This work brings us one step closer to the further goal of improving and tailoring the suction-based adhesion device design against compliant integument. Arrows indicate the flow and connections between each sub research topic.

CHAPTER 2

Cetacean Integument and Suction Cup Performance

2.1 Background

For animals, like cetaceans, that spend most of their lives underwater, body-fixed instruments (biologging tags) are essential for monitoring the behavior, movement, and surrounding environment of the animals during daily-life. These devices can be broadly divided into two categories: 1) low-power tags that make measurements (GPS, temperature, salinity, depth) over periods that range from weeks to months at relatively low sampling rates, and 2) higher-power tags that make high resolution measurements (kinematics, acoustics, video) over the hour to day range. Attachment methods used to secure these tags vary between the two categories [69]. Devices deployed for weeks to months (category 1) are typically attached using skin-penetrating barbs or bolts, typically transmit sparse dive and movement data via telemetry, and tend not to be recovered. For devices that combine a wider range of sensors (e.g., sound or video) sampled at higher resolution, telemetry is seldom an option and data must be stored in on-board memory. These tags (category 2) must be recovered, and the resulting increased memory and battery consumption generally constrain the operating duration to a few days, making a skin-penetrating attachment ethically difficult. The smoothness of cetacean skin facilitates the use of suction cups for category 2 tag attachment [52, 53]. Suction cup tags are applied to free-swimming animals using hand-held poles, an unmanned aerial vehicle (UAV), or a ballistic delivery, and can be released at a programmable time using corrosive wire links, leaving no equipment on the animal [51, 70]. The force created by the cup for attachment inevitably weakens as fluid leaks into the sealed volume over time, making the cups increasingly vulnerable to dislodgement when external forces are created by high-speed swimming, contact with other animals or with the sea floor.

Leakage rates are variable and may be exacerbated by poor skin condition, e.g., due to sloughing, scarring or biofilm growth. Unpredictable longevity of tag attached is particularly problematic for controlled exposure experiments that require set durations of pre-exposure, exposure and post-exposure conditions [71]. Several types and sizes of suction cups have been used on cetaceans,

from large stiff rubber cups designed to attach roof-racks to cars [Schneider, 1998], through to small soft silicone cups [51], raising the question of whether the material and shape of cups influence their attachment tenacity. While an analysis of in-vivo cup performance on cetaceans is not available, cup mechanics have been explored for applications in the packaging industry [72] and for robots designed for climbing on engineered surfaces [73, 63, 74, 66, 75, 62]. These experimental studies have been complemented by models used to estimate adhesion and friction force of a deformed cup [74, 76]. However, these studies focus on systems that actively create attachment forces using pumps. For cetaceans, the weight, power consumption and complexity of a vacuum pump are difficult to accommodate leading almost exclusively to the use of passive suction cups in bio-logging tags.

Passive suction cups attach to a surface by creating a pressure differential (ΔP) between the ambient environment (p_o) and the interior volume of the cup (p_v), Figure 2.1. During attachment, an external force deforms the cup, flattening the lip onto the surface and expelling most of the fluid (air) within the interior volume. The shape deformation and the elastomeric material of the cup store energy during attachment, and after the external force is relaxed, work to restore the cup to its undeformed configuration. As the cup attempts to return to its original shape, the lip acts as a check valve preventing ingress of the surrounding fluid. The seal at the lip, and the increasing internal volume (V) resulting from cup relaxation, create an increased pressure differential (ΔP)) and corresponding increased attachment force (F_A). The internal volume of the cup continues to expand until a balance is reached between the attachment force and the other forces acting on the cup, Figure 2.1 (A). This analysis assumes that the substrate under the cup is perfectly rigid which is a realistic assumption for the surfaces typically used in engineering applications of cups. But the outer surface of cetaceans is compliant leading to a more complex mechanical interaction between the cup and the skin (Figure 2.1 (B)). In this case, the attachment force in the cup pulls the surface into the cup, deforming the substrate and reducing the internal volume of the cup. This reduces the force generated by the cup potentially making the attachment weaker and more liable to be dislodged. Strong deformation of the skin surface can also cause edema that may discomfort the animal and change the local material properties. Thus. the mechanical properties of the substrate may have an important impact on the attachment duration of a suction-cup tag.

In cetaceans, cups are attached to the animal's integument, an organ comprising [58, 59, 60] skin, blubber, blood vessels, nerves, connective tissue and pelage. This system provides protection, thermoregulation, buoyancy, and drag reduction for the animal [77]. Cetacean integument is arranged in epidermal, dermal and subdermal layers that possess both viscous and elastic (viscoelastic) properties [55, 56], and may exhibit a nonlinear stress-strain relationship during loading [57]. The elements of the integument are non-uniformly-distributed and highly-integrated, Figure 2.2. While imaging (ex. CT scan in Figure 2.2 (A)) has been used to characterize this organ sys-

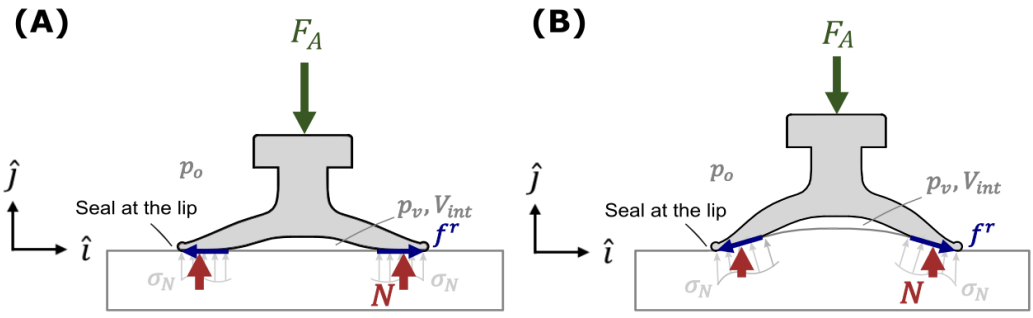

Figure 2.1: An illustration of suction cup mechanics on a rigid (A) and compliant (B) substrate. The material properties of the cup and substrate both contribute to the initial configuration and forces generated by the cup. In the diagram, p_o is the environmental pressure acting on the cup, p_v and V_{int} are the internal pressure and the internal volume of the cup, respectively. $f^r$is the tangential resistive contact force between the cup and substrate. Changes to the internal volume (V_{int}) influence the internal pressure (p_v) and the pressure differential ($\Delta P = p_v - p_o$), which in turn determines the magnitude of the attachment force (F_A). σ_N is the normal stress between the lip of the cup and the attachment surface.

tem, there is scant information on the mechanical properties of this material directly relevant to suction cup design, like *in-vivo* deformation of the organ system under vacuum loading. Studies of cetacean integument mechanics have instead relied on material properties measured from *ex-vivo* samples of the composite tissues collected from cadavers [60]. However, removing the sample from the body inevitably compromises the structural integrity of the composite tissue. As such, *ex-vivo* measurements may provide a biased representation of the behavior of living integument.

To date, *in-vivo* methods to characterize cetacean integument have been lacking. For human integument, researchers have used a variety of meters (indenter [78], and twistometer [79, 80]), ultrasound [81, 82, 83, 84], and multiple optical instruments (light intensity [85, 86, 87], optical coherence topography (OCT) [88], and digital image correlation (DIC) [89, 90]) to capture mechanical responses under various loading conditions. Loading has included indentation [78, 89, 90], torsion [79, 80], acoustic inputs [81, 82, 83] and suction [84, 85, 86, 87, 88]. Using data from these in-vivo experiments, different models have been established [91, 78] to estimate bulk material properties for human integument, such as extensibility and Young's modulus [79, 80].

Here we build on results in the literature by first characterizing *in-vivo* integument compliance, and then through an experimental investigation of passive suction cup performance on compliant substrates. The following questions were used to guide the work: 1) How do the bulk mechanical

properties of cetacean integument vary at potential tagging locations on the body? and 2) How is the performance of a suction cup affected by a compliant substrate? To enable our investigation, we developed a system to measure in-vivo dolphin tissue mechanics and then used the resulting characterizations to inform the interpretation of suction cup performance on engineered substrates with, and without, compliance. The results indicate ways in which a suction cup can be engineered to improve performance on cetacean integument, potentially leading to increased attachment durations with a lower impact on the animal.

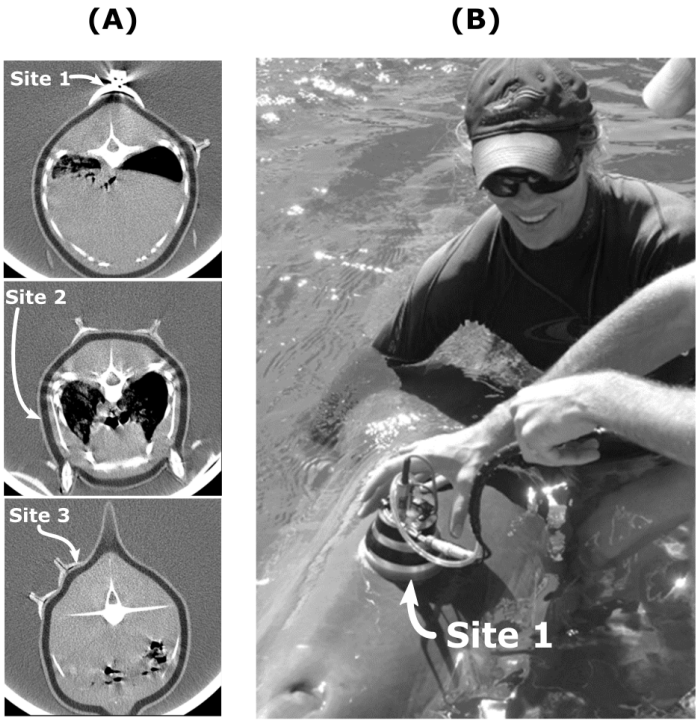

Figure 2.2: (A) Cross sectional CT images from a common dolphin cadaver at the three sites measured with the SSCup. Site 1) Anterior to the blowhole, a location with significant subcutaneous fat; Site 2) above the pectoral flipper, which overlies muscle on the blade of the scapula; and Site 3) near the dorsal fin insertion, which has increased blubber fiber content as part of the dorsal fin saddle. (B) The SScup is shown secured to Site 1 on a representative animal stationing for the data collection.

2.2 Methods

We quantified the response of *in-vivo* bottlenose dolphin integument under vacuum loading using a custom-designed measurement device, the SSCup. This portable system was used to make mea-

surements on animals in human care that were trained to station for the data collection (Figure 2.2 (B)) and on wild dolphins briefly restrained for health assessments. The SSCup was used to mimic forces generated by suction cups by loading integument with a partial vacuum. Viscoelastic properties were then quantified using deformation measurements. We then investigated suction cup performance as a function of substrate compliance using a uniaxial extension machine to load cups to failure when secured to surrogate surfaces. The study protocol for the work conducted with the animals was approved by Woods Hole Oceanographic Institutional Animal Care and Use Committee. Research with wild dolphins in Sarasota Bay was performed under National Marine Fisheries Service Scientific Research Permit No. 20455.

2.2.1 Experimental Integument Characterization

The static suction cup, SSCup (Figure 2.3 (A)), was used to measure integument deformation under vacuum loading in-vivo. A rigid acrylic half-dome body and a molded silicone lip created a sealed volume for the vacuum loading. A LVDT (LT0617, Active Sensors, USA) measured peak integument displacement during loading. A peristaltic pump (200 series, Williamson Manufacturing, UK) created the controllable vacuum loading inside the chamber via flexible tubing to the SSCup. A pressure transducer (US300, Measurement Specialties, USA) measured the differential pressure inside vs outside the chamber, and two thermistors (192-102DEW-A01, Honeywell, USA), one located near the tip of the displacement sensor and the other in the lip of the cup, measured integument temperature during loading. All data were logged using a notebook computer and a USB analog to digital converter (U6, LabJack, USA). The system was battery powered and enclosed in a splash-proof case for portability.

The experiments were conducted with bottlenose dolphins at Dolphin Quest Oahu (Honolulu, HI, USA) and during catch-and-release dolphin health assessments conducted by the Chicago Zoological Society's Sarasota Dolphin Research Program (Sarasota, FL, USA) [92, 93]. Data were collected from 5 animals at Dolphin Quest and 11 animals in Sarasota Bay. The average body mass, length (from the tip of rostrum to the medium notch of fluke), and girth (at the dorsal fin insertion, where the trunk is the widest) of the animals were 198.8 kg (SD 54.2), 2.54 m (SD 0.18), and 1.39 m (SD 13.8), respectively (Table 2.1). At Dolphin Quest, animals were trained to station in the water, and maintain a static posture during data collection (Figure 2.2 (B)). Dolphins in the Sarasota Bay health assessments were resting on a shaded and padded boat deck for veterinary examinations. Displacement measurements were made at three sites on the animals: Site 1: anterior to the blowhole; Site 2: above the pectoral fin; and Site 3: at the dorsal fin insertion, Figure 3A. Bio-logging tags are often placed at or near these three sites, but they have distinct anatomical substructures, with varying amounts of sub-dermal fat, bone and muscle, Figure 2.2 (A).

Table 2.1: Physical Parameters of the Animal Subjects in SSCup Experiment: Data were collected from 5 animals at Dolphin Quest and 12 animals in Sarasota Bay (13 Males and 4 Females). The body mass, length (from the tip maxilla to fluke notch) and girth (max anterior insertion of the dorsal fin) of the animals were listed

Dolphin Quest	Mass (kg)	Length (cm)	Girth (cm)	Sex
TT01	179.0	252.1	127.6	MALE
TT02	243.5	273.1	146.7	MALE
TT03	191.9	261.0	142.2	MALE
TT04	170.9	245.7	132.1	MALE
TT05	165.7	254.0	128.8	MALE
Sarasota Bay	Mass (kg)	Length (cm)	Girth (cm)	Sex
TT06	299.6	273.0	163.5	MALE
TT07	157.4	240.0	131.0	FEMALE
TT08	238.8	271.0	147.0	MALE
TT09	176.0	248.0	135.0	FEMALE
TT10	279.0	260.0	162.0	MALE
TT11	169.0	240.0	134.5	MALE
TT12	121.4	216.0	122.0	FEMALE
TT13	143.2	234.0	126.0	MALE
TT14	256.8	281.0	155.0	MALE
TT15	131.1	234.0	122.5	MALE
TT16	192.4	264.0	134.5	MALE
TT17	264.4	281.0	159.0	MALE
Average	198.8	254.6	139.4	
SD	54.2	18.4	13.8	

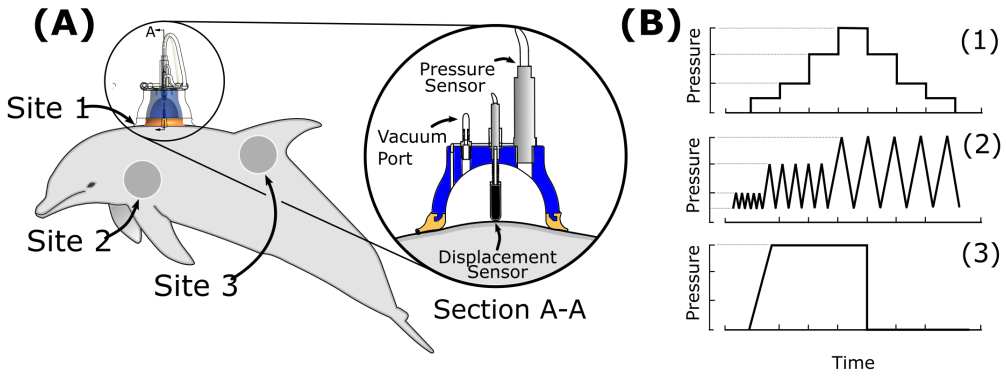

Figure 2.3: (A) SSCup was used to create vacuum loading on the integument during the experiment. Integument deformation was measured with a LVDT. Three sites on the animals with varying substructure were examined during each trial. (B) Three loading profiles were used with the SSCup during each assessment: (1) A static step loading and unloading profile where each load was held for 45 seconds; (2) a repetitive loading profile over three pressure ranges; and (3) a creep-relaxation loading where the load was applied and then held for 95 seconds before release.

Three loading profiles were applied at each site: static step, repetitive, and creep-relaxation loading, Figure 3B. During the static step loading, pressure differential was increased to 0.3 bar and then decreased to 0 bar in steps of 0.1 bar (100 kPa) [actual pressure sequence: 0, 0.05, 0.1, 0.2, 0.3, 0.2, 0.1, 0.05, 0 bar]. The pressure differential at each step was held for 45 seconds to allow the deformation response to reach steady state. Three levels of repetitive loading were used to dynamically load the integument: low [0.05 to 0.1] bar (100 kPa), medium [0.05 to 0.2] bar (100 kPa), and high [0.05 to 0.3] bar (100 kPa). 25 cycles of each loading level were conducted at each site, starting with the low-level and finishing with the high-level loading. A creep-relaxation loading profile was also used to characterize the time-dependent response of the integument, where pressure was first increased from 0 to 0.3 bar (100 kPa) at a constant loading rate (0.012 bar/s), then held at 0.3 bar (100 kPa) for 95 seconds, before the pressure was released. Results from the three loading profiles at the three sites were then used to quantify the viscoelastic behavior of the integument [94].

2.2.2 Suction Cup Testing

Suction cup mechanics during normal loading were experimentally examined using a uniaxial extension testing machine (4301, Instron, USA). Cups were attached to both a rigid acrylic sheet and a compliant integument phantom and loaded until failure (i.e., cups were no longer attached to

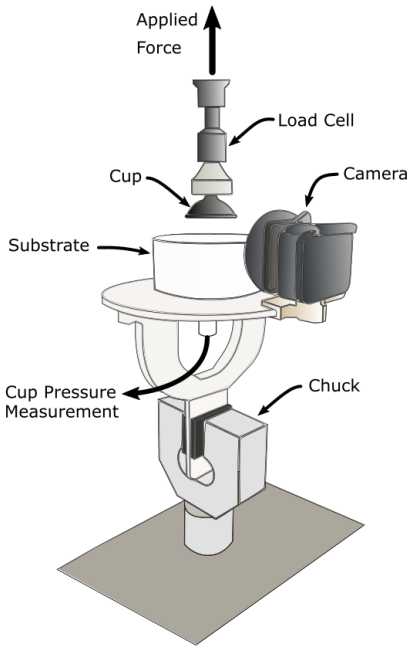

Figure 2.4: A schematic of the experimental setup used to evaluate suction cup performance under normal loading. A universal tester (4301, Instron, USA) was used load the cup at a constant rate ($60mm/min$) until failure. Force, displacement and the pressure differential between the cup and the ambient were all measured during the experiment.

the substrate). In both cases, the surface was cleaned and wetted with water before cup attachment. The cylindrical integument phantom had diameter 95.3 mm and thickness of 44.5 mm and was made from platinum-cured silicone rubber with shore hardness as 00-10 (Ecoflex 00-10, Smooth-On, Inc., USA), Figure 2.4. A constant displacement rate of 60 mm/min was used to load the cups, with the resulting applied normal force (F_P) recorded for each trial. A fixed camera (HERO 5, GoPro, USA) recorded cup deformation during the experiment at 25 FPS, and a pressure transducer (PX3 Series, Honeywell, USA) measured the differential (ΔP) between ambient environment and the internal cup pressure. Data were logged using a USB microcontroller (ARDUINO UNO REV3, Arduino, Italy) and a notebook computer. Water was applied to the substrate surface before the cup was attached by hand. 10 silicone rubber cups (45 mm diameter, 10.4 mm internal height, custom design manufactured by Da/Pro Rubber, Inc., USA) were tested 10 times each on both substrates.

2.2.3 Data Analysis

2.2.3.1 Experimental Integument Characterization

The loading force (F) created by the SSCup during the trials was calculated using the measured pressure differential (ΔP) and the area at the interface between the instrument and the animal ($A_S = 45.6cm^2$) for the static step, repetitive, and creep-relaxation loading trials.

$$\bar{F} = \Delta\bar{P} \times A_S \tag{2.1}$$

Steady state (D_{ss}) deformation and the corresponding pressure differential (ΔP) were calculated using data from the final 25 % of each step during the static step loading trials. Mean displacements ($\bar{D}$) and loading force ($\bar{F} = \Delta\bar{P} \times A_S$) were calculated by averaging values across all trials and all animals. Force vs displacement curves for both loading and unloading were calculated for the static step loading trials. Linear approximations were used to estimate the stiffness of the integument during both loading ($\hat{F}_L$) and unloading ($\hat{F}_U$) periods (k^L and k_U respectively):

$$\hat{F}_L = k^L\bar{D} + c_l \quad whereD \in [\bar{D}_o, \bar{D}_p] \tag{2.2}$$

$$\hat{F}_U = k^U\bar{D} + c_u \quad whereD \in [\bar{D}_p, \bar{D}_f] \tag{2.3}$$

where $\bar{D}_o$,$\bar{D}_p$,and $\bar{D}_f$ correspond to the average initial, peak, and final displacement measured during the trial. The equivalent compliance (C_{eq}) for the three sites was estimated by calculating the reciprocal of the average stiffness ($\bar{S}$) of the loading and unloading curves.

$$\bar{S} = \frac{1}{2}(k^L + k^U) \tag{2.4}$$

$$C_{eq} = \frac{1}{\bar{S}} = \frac{2}{k^L + k^U} \tag{2.5}$$

Equivalent compliance (C_{eq})represents the overall steady state response of the integument during the static step loading experiment, with smaller values corresponding to a stiffer integument.

For the repetitive loading trials, tissue displacement (D) along with the corresponding measured pressure differentials (ΔP) were recorded and segmented into individual cycles for the three conditions. Data for each cycle (loading and unloading) were then normalized to 100 points representing equal intervals from 0 % to 100 % using the spline function in MATLAB (Natick, MA USA). Initial (D_o), peak (D_p), and final (D_f) deformation were identified for each cycle, along with

the corresponding pressure differentials (ΔP). Mean displacements ($\bar{D}$) and pressure differential ($\Delta \bar{P}$) were calculated by averaging for all trials and all animals. Average Force vs Displacement curves were also calculated using the normalized data. Energy loss by the integument was estimated by calculating the area of the hysteresis loop present in the Force vs Displacement curves during cyclic loading:

$$E_{cycle} = \int_{D_o}^{D_p} F^L dD - \int_{D_f}^{D_p} F^U dD \tag{2.6}$$

Where F_L and F_U are the forces during the loading and unloading, and D is the displacement of the tissue. D_o, D_p, D_f correspond to the initial, peak, and final displacement measured during the trial. Energy loss was calculated for each cycle and then averaged to account for nonrecoverable integument deformation that may occur during the loading [95].

Creep and relaxation are time-dependent behaviors of viscoelastic material characterized by progressive material deformation under constant stress [96]. Tissue response during the creep-relaxation loading were parameterized using the settling time required to reach 5% of the steady-state displacement value during both loading (t_c) and unloading (t_r).

2.2.3.2 Suction Cup Analysis

Suction cup shape and attachment force (F_A) were used to characterize performance on both rigid and compliant substrates. Video data were used to parameterize deformation of the cup during loading. The projected area under the cup was divided into two parts, the circular vacuum area (A_v) and the area of the ring of material in contact with the substrate (A_c) [76]. Vacuum area was estimated using the measured cup diameter (D_{lip}), Figure 2.8. Normalized vacuum area ($\bar{A}_v$) was calculated by dividing the vacuum area estimated during the trial (A_v) by the area of the undeformed cup ($A_{v_neutral}$). Contact angle (θ_c) was defined as the angle between the bottom edge of the lip and the tangential line of the bell, and the height of the suction cup was measured from the lip to the top of the cup (H_{SC}), Figure 2.8. Peak displacement of the substrate (D_p) was calculated as the maximum distance between the loaded substrate profile (H_s) and the initial setup height.

Initially, the attachment force (F_A), the normal force (N), and the resistance force (f^r) tangent to the contact between the cup lip and the substrate are balanced as shown in Figure 1.6. The vacuum force ($\overrightarrow{F}_V$) created by the pressure differential (ΔP) between atmospheric pressure and the lower internal pressure in the cup is:

$$\overrightarrow{F}_A = [\Delta P \cdot A_v + P_{atm} \cdot A_c]\, \hat{\jmath} \tag{2.7}$$

The vertical forces acting on the cup (assuming the resistance force (f^r) is negligible) during the constant rate loading are:

$$\hat{\jmath}: \; F_V = F_A - N \tag{2.8}$$

Where F_P is the magnitude of the applied load and N is the magnitude of the normal force acting on the cup at the contact area. To simplify the analysis, the force generated by the ambient pressure ($P_{atm} \cdot A_c$) was assumed to be small enough to neglect, and the vacuum area (A_v) was estimated using the diameter of the cup (D_{lip}) measured from the video, Figure 2.8. The vertical component of the normal force was then estimated as the difference between the estimated vacuum force ($\Delta P \cdot A_v$) and the applied force:

$$\hat{\jmath}: \; N = F_V - F_P \; \rightarrow \Delta P \cdot \frac{\pi (D_{lip})^2}{4} - F_P \tag{2.9}$$

Suction cup performance was evaluated on two substrates: a rigid acrylic sheet and the 00-10 silicone integument phantom. Force, pressure and image data were collected during the trials, and used to characterize cup performance starting at the initial setup and continuing to failure under normal loading. Data were then normalized to percentage of the trial using the time the loading was initiated (0%) to the time at failure (100%).

2.3 Results

In vivo tests of dolphin integument demonstrated viscoelastic behavior, but the response varied among sites. The responses at Site 1 (anterior to the blowhole) and 2 (lateral above the pectoral fin) were comparable, while the integument at Site 3 (at the dorsal fin insertion) was stiffer and dissipated less energy. Results from the cup testing on the rigid and compliant substrates indicate that a compliant substrate reduces cup performance.

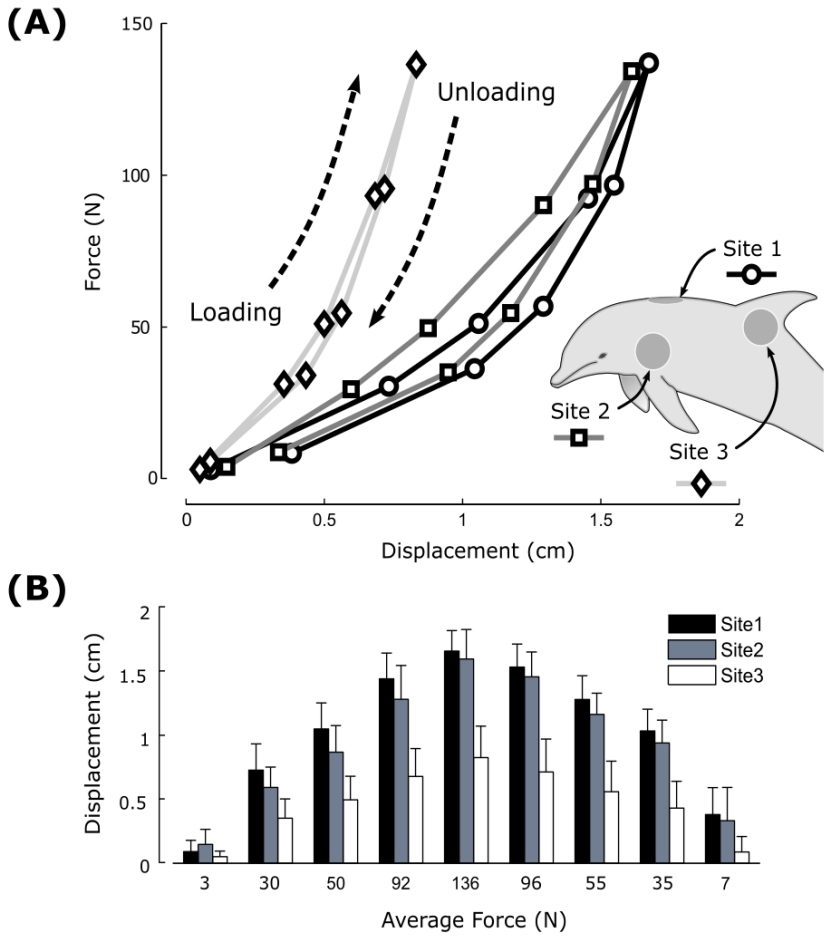

Figure 2.5: (A) Average steady state force vs displacement curves for the three loading sites. Sites 1 and 2 showed more compliance and hysteresis then Site 3. (B) Average steady state deformation at the nine loading conditions, along with standard deviation. The deformation at Sites 1 and 2 were larger than those measured at Site 3 at all loading conditions.

2.3.1 Integument Testing Results

2.3.1.1 Static-Step Loading

Figure 2.5 (A) presents average steady state force vs displacement curves calculated using data collected during the static step loading trials. Each data point represents the average integument response at the 9 loading steps across all the trials from all the animals. The average deformation at each load, along with standard deviation of the measurements are also shown in Figure 2.5 (B). A nonlinear stiffness response was observed at the three sites, with the data at Site 3 indicating the stiffest response with the least hysteresis. The integument response at Sites 1 and 2 were comparable both in terms of the peak deformation and the hysteresis during the loading cycle. At

the highest loading condition (136 N) the integument deformation was twice as large at Sites 1 and 2 than at Site 3 (1.5 cm vs 0.75 cm). These trends were reflected in the calculated equivalent compliances (C_{eq}), which were 0.012, 0.011, and 0.006 cm/N, at Sites 1, 2 and 3 respectively, Table 2.2.

2.3.1.2 Repetitive Loading

Figure 2.6 presents average integument deformation (C) and the average loading force (B) during the dynamic loading trials. Standard deviations at each percentage of the trial are presented as shaded regions around the average. Average force and displacement were used to plot work loops during the repetitive loading, Figure 2.6 (A). The integument at Site 3 has the stiffest response with maximum displacement of around 0.7 cm at a peak load of 135 N. The work loops at Sites 1 and 2 were comparable and had approximated maximum deformations of around 1.4 cm at peak loading. Nonlinear stiffening was present at all three sites during the loading phase of the cycle indicating that the stiffness of the integument increases at larger deformations. The energy lost during the cyclic loading was comparable at Sites 1 and 2, and much larger than the energy loss calculated at site 3, Table 2.2.

2.3.1.3 Creep-Relaxation Loading

Results from the creep-relaxation loading were used to characterize the temporal response of the integument to loading, Figure 2.7. The average and the standard deviation (shaded) of the loading and unloading profiles (Figure 2.7 (A)), along with the corresponding integument response (Figure 2.7 (B)) from the three sites are presented. The integument was loaded at a constant rate and then held at 0.3 bar before release. The stars denote the data points when the deformation is first within 5 % of the steady-state value during loading as well as unloading. Values of the corresponding settling time for creep (t_c) and relaxation (t_r) were also compared (Figure 2.7 (C), Table 2.2). During loading, maximum pressure was reached 40s after the start of the trial, and the tissue at Site 1 had the fastest response with a creep time of 41.4 ± 8.6s. During unloading, pressure was released from the chamber in less than 1 s. Sites 1 and 2 had comparable relaxation times of 1.7 ± 1.1s and 1.8 ± 0.7s respectively, both of which were faster than Site 3 (3.0 ± 2.2s).

2.3.2 Suction Cup Testing Results

2.3.2.1 Suction Cup Kinematics

The deformation of the suction cups on the two substrates was visibly different. Figure 2.8 presents image data from 0, 25, 50, 75, and 100 % of a representative trial with the rigid (A) and compliant

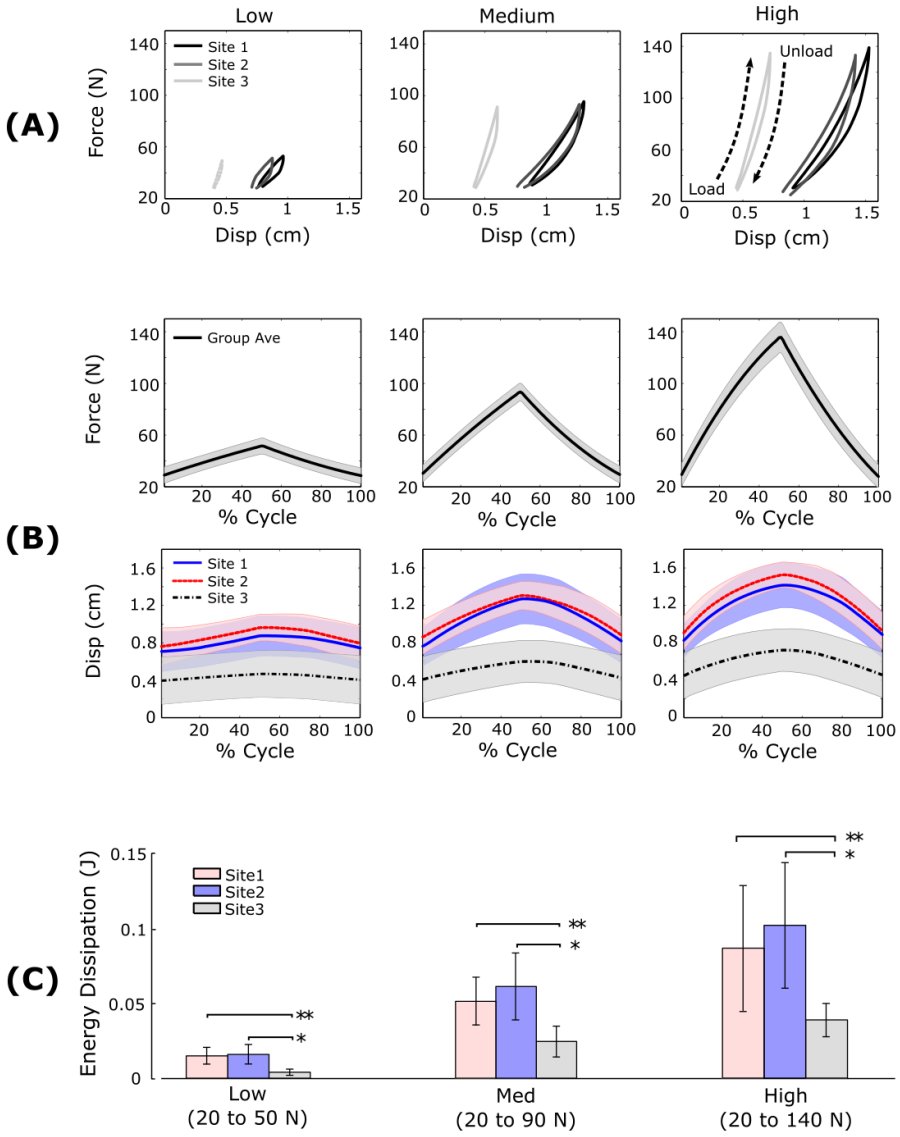

Figure 2.6: (A) Average force vs displacement curves for the three sites during low, medium, and high cyclic loading. (B) Mean and standard deviation of the force and the displacement are shown for the loading at the three sites. (C) Mean and standard deviation of the energy dissipation at the three sites.

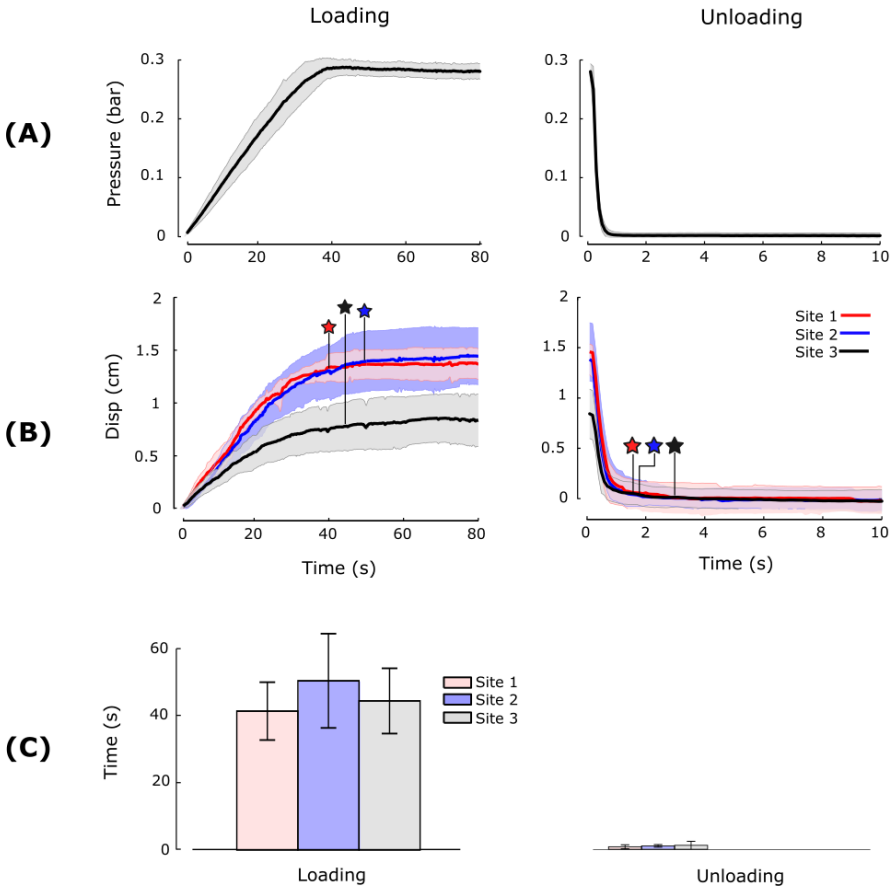

Figure 2.7: (A) Mean and SD are shown for creep and relaxation loading at the three sites. (B) Mean and SD of the resulting deformation at the three sites. The stars identify the average settling time to reach within 5% of steady state for each site during the loading and unloading phases. (C) Settling time is indicated by the stars during loading and relaxation, with the corresponding SD bars.

Table 2.2: SSCup In-vivo Measurement Result: The equivalent compliance (C_{eq}) represents the displacement (cm) of the substrate per unit loading (N), a larger C_{eq} means the integument at the site deforms more under the same under loading. Energy loss ($E_{cycle}(J)$) indicates the magnitude of energy dissipated by the integument during the cyclic loading. A larger E_{cycle} results from a larger hysteresis loop (energy difference) between the loading and unloading curve. Settling time for creep ($t_c(s)$) and relaxation ($t_r(s)$) indicates the rate that the integument at 3 sites reaches steady-state during loading and unloading.

	Static Step Loading	Repetitive Loading			Creep-Relaxation Loading	
Test Site	C_{eq} (cm/N)	E_{cycle} (J)			t_c (s)	t_r (s)
		Low	Medium	High		
Site 1	0.012	0.015 ± 0.006	0.051 ± 0.016	0.087 ± 0.042	41.4 ± 8.6	1.7 ± 1.1
Site 2	0.011	0.016 ± 0.007	0.061 ± 0.022	0.102 ± 0.042	50.4 ± 14.0	1.8 ± 0.7
Site 3	0.006	0.004 ± 0.002	0.024 ± 0.010	0.039 ± 0.011	44.4 ± 9.7	3.0 ± 2.2

(B) surfaces. Cup geometry was divided into two parts (Figure 2.8, the 3^{rd} subplot in (A)): 1) The Bell: from the lip at the substrate to the concave notch of the profile; and 2) The Neck: from the concave notch to the top of the suction cup which is enclosed inside the connection with the testing machine. Measurements of peak substrate displacement (D_p, the 5^{th} subplot in (B)) and the applied load (F_P) were used to calculate the stiffness of the substrates, Figure 2.9 (B). The stiffness of the compliant substrate compares well to the measured integument compliance at Sites 1 and 2 from the dolphins.

On the rigid substrate, the cup exhibited a two-stage deformation, with initial deformation at the neck followed by an elongation and expansion of the bell. Initially, cups on the rigid substrate had a flatter setup profile compared to cups on the compliant substrate (1^{st} column of Figure 2.8). This was characterized by a smaller contact angle (θ_c) and a lower suction cup height (H_{SC}). During initial loading on the compliant substrate there was little visible deformation of the neck. As loading increased the bell and substrate deformed together until failure. Deformation of the compliant substrate resulted in a smaller cup diameter with a more pronounced concave shape when first attached. During loading the cup and substrate deformation were coupled. The substrate deformed into the cup and reduced the internal volume throughout the loading, leading to a lower internal pressure (p_v) and smaller pressure differential (ΔP). Just before failure, cups on both substrates had similar vacuum areas ($A_v \cong \frac{\pi(D_{lip})^2}{4}$), Figure 2.8 ($5^{th}$ column) and Figure 2.9 (A). But the cup on the rigid substrate had a larger contact angle (θ_c) and a higher suction cup height (H_{SC}), leading to a larger internal volume compared to cups on the compliant substrate. These changes in geometry result in a larger internal volume (V_{int}), a lower internal pressure (p_v), and therefore larger vacuum force (F_V) for cups on a rigid substrate.

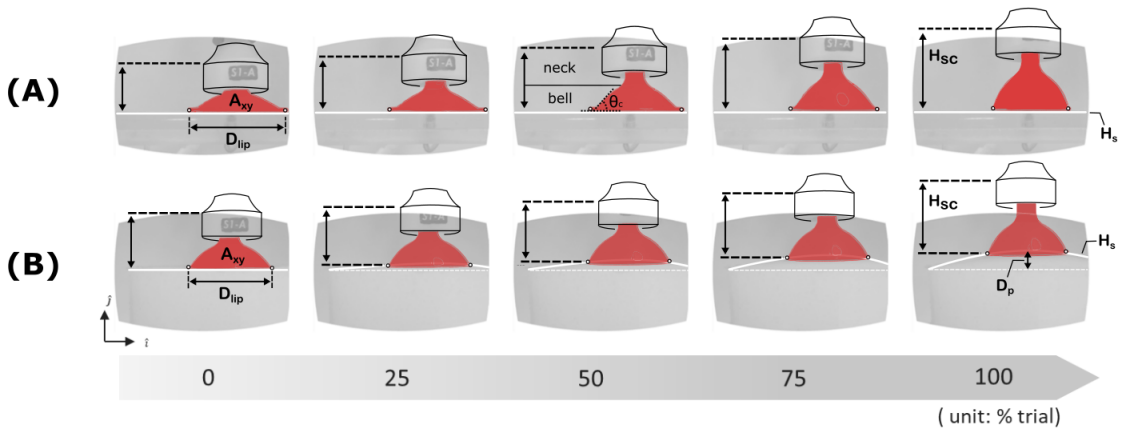

Figure 2.8: Suction cup deformation from representative trials on a rigid substrate (A) and a compliant substrate (B). There are noticeable differences in both the cavity expansion and the overall cup deformation between the two cases. Both of which influence cups performances.

2.3.2.2 Suction Cup Kinetics

When first attached, the magnitude of the vacuum force (F_V) generated by the cup (material and shape) and the normal force (N) are equal and opposite, Eq 2.9. At this point the cup is in compression and the normal force created by material and shape is acting to restore the cup to its initial shape. The average initial vacuum force was slightly larger for cups attached to the rigid substrate ($\sim$ 25 N vs 23 N), Figure 2.10. As the applied load (F_P) increases the magnitude of the vacuum force also increases, and the normal force decreases as the shape of the cup approaches its undeformed state. Figure 2.10 (sub figures on the top) presents the silhouettes that capture the deformation of the cups at 0, 25, 50, 75 and 100 % of the trial, along with a vector estimating the magnitude and direction of the estimated normal force.

The cups on both substrates were loaded with a constant displacement of 60 mm/min, but the applied force at failure was twice as large for cups tested on the rigid substrate (50 N vs 25 N). On the rigid substrate, the cups had two distinct regions of roughly linear stiffness: a lower stiffness from 0 – 20 % of the trial, and then a higher stiffness up to failure (Figure 2.10 (A)). The stiffness response of the cups tested on the compliant substrate was closer to linear throughout the trial (Figure 2.10 (B)). On the rigid substrate, the cup deformed more than that on the compliant substrate, transitioning from compression to tension at $\sim$86 % of the trial. On the compliant substrate, the suction cup and the substrate both deform during loading, but fail before the transition from compression to tension. In both cases cup deformation created by the applied force increases the cup volume, decreases the pressure differential, and increases the vacuum force.

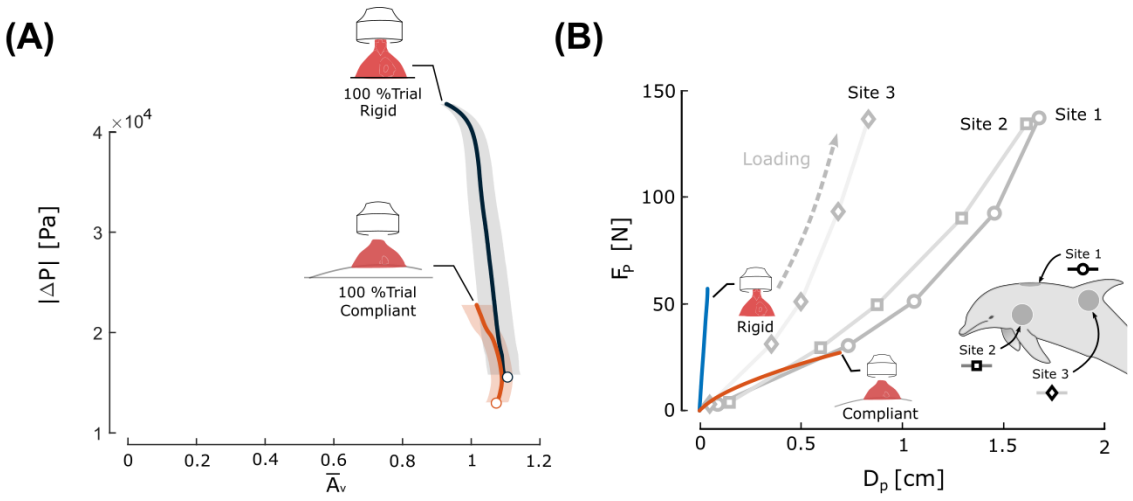

Figure 2.9: (A) Correlation between the pressure differential ($|\Delta P$—) and normalized vacuum area ($\overline{A}_v = A_v/A_{v,neutral}$). (B) Force ($F_P$) vs peak displacement ($D_p$) during the static-step loading is compared to data collected from the substrates during the cup testing. The stiffness of compliant substrate compares well to the values measured at Sites 1 and 2.

This continues until a leakage pathway is created at the lip of the cup results in attachment failure. Cups tested on the rigid substrate deformed more and failed at larger applied forces.

2.4 Discussion

Despite the widespread use of suction cups to attach bio-logging tags to cetaceans, little is known about the factors that control the tenacity of this attachment method. A major factor is the compliance of the surface to which the cups attach: cetacean integument is viscoelastic unlike the rigid substrates on which suction cups are typically used. This raises questions of how integument compliance affects cup mechanics and whether cups can be designed to improve their performance on a compliant substrate. This study makes a first step to address these questions. Specifically, we used an experimental approach to 1) characterize dolphin tissue mechanics at tag attachment sites, and 2) compare cup performance on compliant and rigid substrates. Measurements of integument deformation under vacuum loading were made at three sites on bottlenose dolphins using a novel *in-vivo* measurement system, SSCup. Integument deformation at all three sites demonstrated a viscoelastic response, but the fibrous tissue around the dorsal fin (Site 3) differed greatly from the other two sites on the trunk. Site 3 had half the equivalent compliance (C_{eq}), less than half the energy loss (E_{cycle}) and half the peak displacement (D_p) compared to Sites 1 or 2 (Table 2.2, Figures 2.5 and 2.6). These differences in the viscoelastic response demonstrate the inhomogeneity

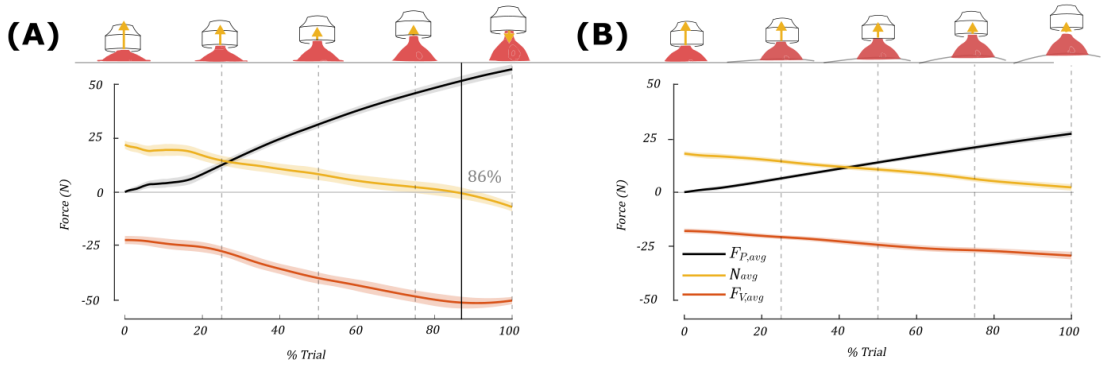

Figure 2.10: A comparison of the average cup performance during normal loading on rigid (A) and compliant (B) substrates. The pulling force (F_P), normal force (N), and vacuum force (F_V) for both conditions. The estimated direction of the direction and magnitude of the normal force (N) is illustrated with the arrows in the silhouettes of the cup at the top of each plot.

of cetacean integument created by distinct anatomical substructures, including varying amounts of sub-dermal fat, bone and muscle underneath each test site. The CT scans in Figure 2.2 (A) show that integument is deformed by the cups to varying degree at all three sites. This deformation reduces the internal volume of the cup, leading to lower pressure differentials when compared to measurements made with the same cups on a rigid substrate.

To investigate the impact of substrate compliance on cup performance, silicone suction cups were attached to both rigid (acrylic) and compliant (00-10 silicone rubber) surfaces and loaded to failure. The load-deformation response of these two engineered materials bracket the measured compliance at the three test sites on the dolphins, Figure 2.9 (B). As such, suction cup performance on a dolphin might be expected to fall between the results measured on these two surfaces. Because material response is dependent on strain rate [96], a low displacement rate (60 mm/min) was selected for the tests to be comparable to relatively slow hydrodynamic force changes likely experienced by a suction cup attached to a marine animal traveling at a steady speed. Animals swim at a range of speeds creating hydrodynamic loads on the tag in both normal (lift force) and shear (drag force) directions. The magnitude of the loading will depend on the speed of the animal. For example, steady state dolphin swimming speeds ranging from 1 to 5 m/s have been measured with tags [97]. These speeds can create drag forces ranging from 1 to 15 N and lift forces ranging from 1 to 60 N on bio-logging tags [98]. Forces generated by cups to resist hydrodynamic loading are related to the pressure differential between the cup and environment, and the projected area of the internal volume (A_v). Experimental results demonstrate that cup performance was significantly

impacted when attached to a compliant substrate. Cup geometry was more bell-shaped when first attached to the compliant surface, resulting in different mechanics at the lip-substrate interface, Figure 2.10.

During loading on the compliant substrate, both the cup and substrate deformed until a leakage path was created at the lip, resulting in failure. Peak applied force at failure on the compliant substrate ($\sim$25 N) was half that on the rigid substrate ($\sim$50 N). Failure under normal loading is impacted by the magnitude of the deformation that occurs before a leakage pathway is created at the lip-substrate interface. Cups on the rigid substrate deformed more before failure, resulting in the larger internal volumes and pressure differentials, improving performance. Figure 2.9 (A) shows that suction cups attached to the rigid substrate can generate pressure differentials that are more than twice as large as cups attached to the compliant one, but the projected cup area at failure was comparable between the two. Integument stiffness depends on the anatomy of the underlying tissues at the site. Areas of the body such as the dorsal insertion, where there is more fibrous tissue and less blubber or muscle, will tend to have lower compliance. The results from the failure testing on the compliant substrate suggest that suction cups might perform best at the stiffest site tested on the animals (Site 3) which most closely approximates a rigid surface.

The material properties of the suction cup influence cup performance. For example, cup stiffness is directly related to the deformation of a compliant substrate during attachment and loading: a softer cup will deform the substrate less, while a stiffer cup will result in more deformation. Compliance of a suction cup depends on both the shape and material selected for the design. Compliance can be increased be selecting a softer material for a given cup geometry, or by reducing the thickness of cup walls (changing the cup geometry). However, modifications that result in a softer cup may have an increased risk of failure by other mechanisms, e.g., by buckling of the cup or folding of the lip during normal loading or if the cup slides on the body. Further, the cups secure kinematic sensors to the animals to measure movement, and compliant cups will deform more under cyclic hydrodynamic loading increasing noise in the kinematic measurements from the animal. Fabricating hybrid cups that are more compliant than the integument at the interface would reduce the deformation created by the cups and lessen the coupling of the applied hydrodynamic loading to the integument during swimming. Lower pressure differentials would also decrease integument deformation at the attachment site. These lower differentials could be achieved without a reduction in attachment force by increasing the projected area of the cup.

2.5 Summary

To conclude, these results are a step forward, but there are important considerations for future research. Substrate compliance affects cup performance, and bulk integument properties varied

based on the anatomical substructure. Because bio-logging tags are placed on a number of animals of varying size and body composition, how applicable integument measurements from dolphins are for other species is unclear. Bio-logging tags are attached with suction cups on an ever-increasing range of species. Our results suggest that animals with thicker, less fibrous blubber will tend to have more integument compliance. Integument properties are likely to vary with ontogeny, body condition and habitat even within a species. Measurements from more animals and from multiple locations will be important to build on these results and inform the design and selection of cups for different species. However, *in vivo* measurements of animals in good condition are seldom possible for many species, especially larger whales. In these situations, using *ex vivo* measurements and simplified measurements of integument mechanics (e.g. indentation hardness tests or tensile tests [99]) could provide initial context and perspective about the attachment surface. Cadaver studies from a broader range of species could also provide an initial set of properties to inform cup designs and the selection of surrogate materials for engineered substrates that would better mimic integument.

Additionally, in this study, we only investigated cup performance during normal loading, but the hydrodynamic forces acting on a bio-logging tag will generate normal (lift) and shear (drag) forces. Characterizing performance during shear loading with additional testing will be critical for understanding failure modes and improving tag/cup designs. The main force resisting shear loading can be approximated using friction models like Coulomb's law. For this model, the resistive force (f^r) is dependent on both the normal force (N) and the friction coefficient on the contact surface. For our case, the normal force (N) is positively related to the vacuum force (F_V) per Eq 2.9. A compliant integument reduces the vacuum force (F_V) but tends to increase the contact surface area as the substrate deforms into the cup, Figure 2.1 (B). The net impact of integument compliance on shear force resistance is therefore complex and will require improved integument surrogates for lab testing. Additionally, an improved understanding of the hydrodynamic and hydrostatic forces that tags experience when deployed on animals would provide important context for the design of future experiments.

CHAPTER 3

In-vivo Cetacean Integument Investigation

3.1 Problem Statement

Characterizing and modeling cetacean integument is necessary to facilitating suction cup design for bio-logging tags because suction cup performance depends highly on the substrate. In-vivo measurement of skin parameters are difficult to collect from live cetaceans due to they are highly mobile and live in a marine environment. Building on the pioneer work introduced in Chapter 2, my first task aims to generate new knowledge about in-vivo cetacean integument by accomplishing the following:

Task 1: Development of a portable, splash-proof, full-field in-vivo measurement system to investigate cetacean skin response to vacuum loading.

Task 2: Establishment of the cetacean skin characterization paradigm.

Task 3: Selection of a suitable viscoelastic model for cetacean skin and experimental identification of model parameters.

3.2 Background

Cetacean integument is composed of skin, blubber and pelage, and functions to protect the animal from the environment, to thermoregulate the body, contributes to the net buoyancy of the animal, and can reduce drag forces as the animal moves through the water [77]. This system is made up of layers (stratum corneum, vessels, nerves, connective tissue, blubber, fat) that possess both viscous and elastic (viscoelastic) properties and exhibit a nonlinear stress-strain relationship during loading [57]. Further, the highly integrated layers that make up the integument are not distributed uniformly, resulting in an anisotropic nonhomogeneous viscoelastic composite. Characterization

of the viscoelastic properties of cetacean integument is critical for both gaining a better understanding of animal anatomy and facilitating the design of bio-logging tags that are placed in direct contact with the skin [58, 59, 60].

The contact between bio-logging tags and cetacean integument is a type of bio-mechanical interfaces, where a biological system and a mechanical apparatus with mismatch impedance interact with one another and oftentimes results in discomfort on the biological side of the system. Bio-mechanical interface examples are abundant in the daily life. Human examples including: the interface between our feet and the shoes we wear, the plaster cast around a broken arm, and dental implants surrounded by the gingival tissue, to name just a few. As for animals, such as horseshoe and horse hoof, ear tags on livestock, or the fish hook on fish jaw...etc. An impedance mismatch between a hard device (ex. bio-logging tags) and soft biological system (ex. cetacean integument), relative movement or poor fit at the interface creates discomfort or even tissue damage.

As the technology continually improves, sensors and embedded systems are getting smaller, more power efficient, and more present in our everyday lives. These systems can be fixed directly to the body, making fit particularly important. One class of these systems, bio-logging tags, are widely used to track and study animal movement and behavior in their natural habitat. Bio-logging tags are especially valuable for behavioral observation of cetaceans, animals that spend the majority of their lives under water and range widely in the open ocean. Various types of bio-logging tags have been developed to collect and store high-resolution sound, image and motion data for intervals of hours to days [49, 50, 51]. Figure 3.1(a) shows a bottlenose dolphin (*Tursiops truncatus*) wearing a representative bio-logging tag (Mtag) which was designed and manufactured by our research group, ESTAR (Embedded System for Tracking and Robotics) at the University of Michigan, to monitor the dolphin kinematics, and is secured to the animal using four suction cups. This suction-based attachment approach have been used widely for the last 20 years to attach short-term bio-logging tags to marine animals including many species of whales, dolphins, and turtles [52, 53]. Suction attachments are especially beneficial in cases where the recording longevity of the tag, the size or state-of-health of the study animal, or the need to recover the tag, make long-term invasive tagging inappropriate. These suction cup tags can be applied to free-swimming animals using poles or ballistic delivery, and the uniformly smooth surface of many marine mammals make suction cup attachments ideal for these animals. Additionally, the capability to deliver tags to many species without the need for capturing individuals, make suction cup tags a critical tool for research on species or on populations for which there is strong public sensitivity.

Besides all the advantages, using suction cups to secure bio-logging tags onto compliant cetacean integument has drawbacks as well. When a suction cup attaches to a compliant substrate, it generates a vacuum force (F_V) to load the substrate which in turns deforms the viscoelastic composite to reach a force equilibrium of the system. If the F_V created by the cup is too large it

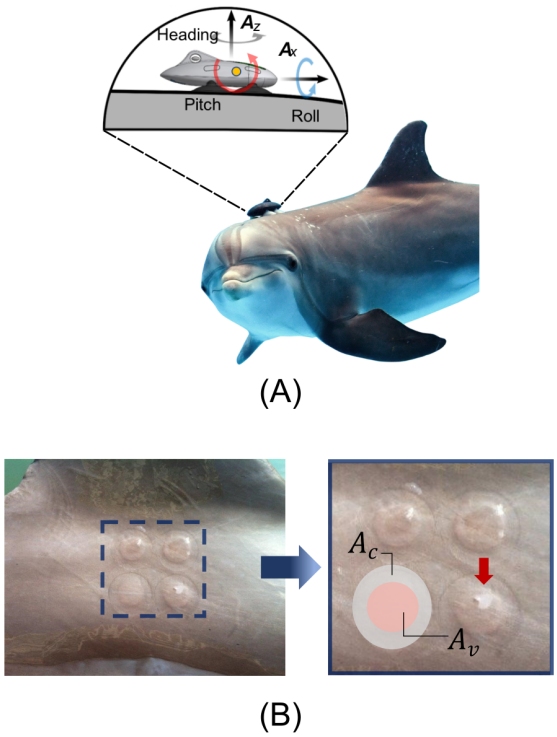

Figure 3.1: (A) A bottlenose dolphin (*Tursiops truncatus*) wearing a bio-logging tag (Mtag). The figure detail shows a closer look at the Mtag, which integrated multiple sensors (accelerometers, gyroscopes, magnetometers, pressure sensor, speed sensor, and temperature sensor). (B) Skin deformation after removing bio-logging tag. A_v and A_c refers to the vacuum area in the middle and the surrounding contact area, respectively. The red arrow points to the sloughed skin.

may cause discomfort and result in modified animal behavior. This includes the animals actively working to remove the bio-logging tags by breaching or rubbing the tag off on other animals or the ocean floor. On the other hand, if the F_V is too small, hydrodynamic forces acting on the tag become large enough to push the tag down the length of the body and off the animal. Both cases are undesirable since they result in a premature detachment of the tag from the animal. Additionally, the continued loading and skin deformation cause not only discomfort to the animals but even lead to capillary rupture and bruising. As shown in Figure 3.1(b), there is a visible skin irritation mark due to continued loading and deformation at each cup site after an 8-hour tag deployment. These cup 'foot-prints' are composed of two areas, the center circular area (A_v) where the vacuum loading occurs and the surrounding area (A_c) where the skin is in contact with the cup lip. Discoloration at the cup sites has been observed for more than 48 hours after day scale tag deployments. The previous studies conducted by our research group verified that suction cup performance is greatly affected by the properties of the attachment site (Chapter 2), and the same suction cup can

sustain as much as twice of the normal loading when attached on a rigid substrate versus on a compliant one (Section 2.3.2.2). Therefore, to improve the attachment duration of suction-based bio-logging tags and the liability of the collected data, it is necessary to be able to characterize cetacean integument properties to either distinguish the more suitable spot to place suction-based bio-logging tags or to choose suction cups whose impedance are more compatible with the targeted cetacean integument.

To characterize integument properties, both ex-vivo and in-vivo methods have been developed. Ex-vivo testing allows for the precise characterization of tissue samples separated from cadavers in a controlled laboratory environment. In-vivo measurements, on the other hand, can be used to collect data from live animals without compromising the structural integrity of the composite tissue. While there is a lack of information in the literature about cetaceans, previous in-vivo human skin studies can be categorized based on measurement methodologies and loading conditions. Researchers have used meters (such as indenter [78] and twistometer [79, 80]), ultrasound [81, 82, 83, 84], and optical instruments (for examples: light intensity [85, 86, 87], optical coherence topography (OCT) [88], and digital image correlation (DIC) [89, 90]) to capture skin responses under various loading conditions. Loading has included but not limited to indentation [78, 89, 90], torsion [79, 80], acoustic inputs [81, 82, 83] and suction [84, 85, 86, 87, 88]. Using data from these in-vivo experiments, different models have been used [91, 78] to estimate bulk material properties for the skin, like skin extensibility and Young's modulus [79, 80].

However, due to inherent challenges associated with collecting data from free-swimming animals, previous studies of cetacean integument mechanics have focused on the experimental measurement of material properties of ex-vivo samples of the composite tissues collected from cadavers [60]. These ex-vivo measurements may fall short in capturing the material properties of the composite and fail to represent the behavior of the living tissue as a whole. In-vivo skin characterization methodologies have not been directly applied to cetaceans until a previous study conducted by our research group [100]. Build upon our previous work, in this study we established a paradigm for cetacean integument characterization and modeling with an innovative optical in-vivo cetacean integument measurement system, and conduct an pilot study on cadaver to verify the feasibility of the paradigm.

3.3 Methods

3.3.1 Equipment: Portable Digital Image Correlation System

To capture how cetacean integument responds to vacuum loading inside the area enclosed by suction cups, the portable digital image correlation (PDIC) system (Figure 3.2(a)) is developed by

our research group (ESTAR: Embedded Systems for Tracking and Robotics) at the University of Michigan. PDIC is a pioneer instrument which can make full-field in-vivo cetacean integument measurements. digital image correlation (DIC) is an optical surface displacement measurement technique that can capture the shape, motion, and deformation of an object by tracking a pattern in a sequence of images [101]. Compared to the SSCup (Static Suction Cup) system used in the pilot study which features a LVDT for single-point measurement (Session 2.2), PDIC equipped two cameras to realize stereo vision which enables us to see the 3D deformation of integument under vacuum loading without introducing disturbances. With the full-field information of the enclosed area, the collected data provides the possibilities to extract the comprehensive material properties of the integument, including anisotropy, nonhomogeneity and viscoelasticity. Vacuum loading is selected to not only simulating the loading exerted by suction cup to cetacean integument but also because it is the most used technique in clinical dermatology for its' simple implementation, and a broad range of regions which can be tested on [102, 103, 104, 105, 106].

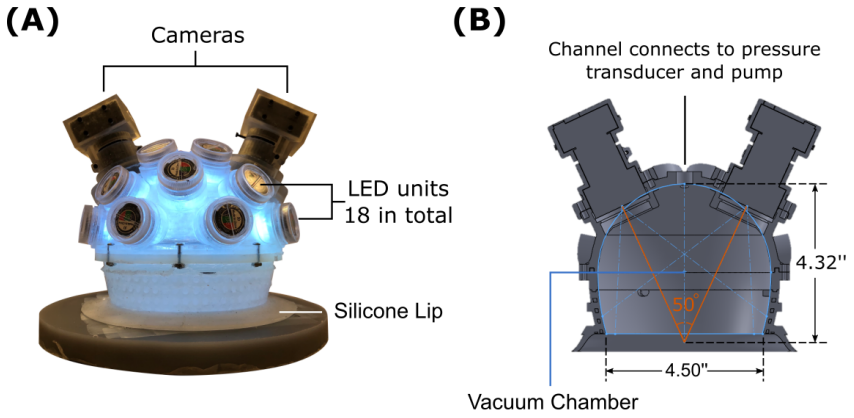

Figure 3.2: (A) Portable Digital Image Correlation (PDIC) system and (B) a cross-sectional view the assembly. PDIC combines traditional stereo DIC, with a 50-degree angle between cameras, and a vacuum chamber (Height: 4.32", diameter: 4.50") which also serves as the camera mount. A pump and pressure sensor are used to create and sense the vacuum in the chamber. A silicone lip provides a compliant seal at the surface interface. Eighteen LED units were mounted on the outside of the vacuum chamber for illumination.

PDIC is fully developed, fabricated, assembled, and tested in our lab, and the designs went trough multiple iterations. The one shown in Figure 3.2(a) is the latest model which were used in our pilot study on the dolphin cadaver. The main structure of PDIC were 3D printed using Form 2 (Formlabs, Somerville, MA, USA) with Clear Resin (Formlabs, Somerville, MA, USA) as material in two separated pieces. The dome-shape top piece serves as both the camera rig as well as

the LED mounts. The two cameras were angled 50-degree in between, and there were 18 battery-powered LED units mounted on the outside of the dome for illumination. In the center of the top piece is a channel connects to the pressure sensor and the pump for the purpose of measuring and regulating the pressure differential (ΔP) between the PDIC chamber and the surrounding environment. The bottom cylindrical piece works as the base configuration of the silicone lip, which features a netted structure that enables silicone to flow through, mold on and anchor the lip in place once the silicone is set. The compliant silicone lip can follow the profile of the integument to generate a sealed environment inside PDIC chamber. The two pieces were then assembled together using bolts and screws, with the joint grove in between covered with silicone to ensure a complete seal. Figure 3.2 (a) showcases the PDIC system and (b) the cross-sectional view the assembly. The completed vacuum chamber is 4.32 inch in height and 4.50 inch in diameter, the size is chosen as a combination result of the printing volume limitation of Form 2 printer as well as to enclose the footprint of the bio-logging tags design by our research group.

To achieve a precise measurement result with DIC, an important factor is the trackability of the pattern on the subject in the series of images taken throughout the loading procedure. For the best practice, the pattern should feature unique non-repetitive arrangement with nice contrast along with pixel size tailored to the camera shutter speed and the strain rate of the measured object [107]. For our application, the pattern on integument should also be splash-proof and easily applicable and repeatable on live cetacean. After experimenting multiple methods of creating patterns, we settled on the stamp and ink pad approach and build a revolutionary custom stamp specifically designed for cetacean integument with the assistance from 1900 Engineering company (Clemson, SC, USA). The finished stamp can successfully a 500-micron randomized speckle pattern onto compliant substrate, which is the dolphin cadaver integument in our pilot study. The process contains two steps, a powdered white pigment ink (HERO ARTS, Richmond, CA) was applied first as a base coat to increase contrast, followed by the stamped speckle pattern in waterproof black pigment ink (Rangerink, Tinton Falls, NJ)(Figure 3.3).

3.3.2 Experimental Facility and Experimental Setup

The pilot study was conducted on a common dolphin (*Delphinus delphis*) cadaver at Woods Hole Oceanographic Institution (WHOI, Woods Hole, MA, USA) autopsy lab in June 2019. The source of the cadaver originates from the stranded animal discovered on a beach in Cape Cod earlier the same year. The cadaver had been preserved in freeze condition and was thawed 72 hours prior to the experiment. Figure 3.4 showcases the photos taken during the experiment. To ensure proper placement, the PDIC was positioned near the upper rim of the left pectoral fin of the animal. This location was chosen for two reasons. Firstly, the size of the animal restricted the available area

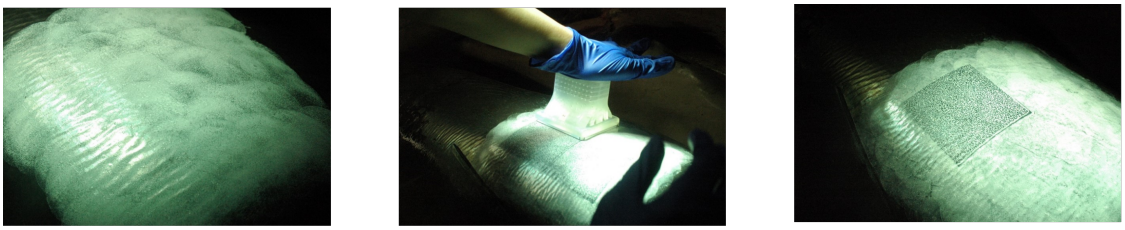

Figure 3.3: Application of the splash-proof random 500-micron speckle pattern onto the skin of the dolphin cadaver. A custom silicone stamp was designed for cetacean skin in collaboration with 1900 Engineering company (Clemson, SC, USA). A powdered white pigment ink was applied first as a base coat to increase contrast, followed by the black stamped speckle pattern.

where the lip of the PDIC could be fully secured and sealed. Secondly, this particular area is one of the larger smooth areas where bio-logging tags are commonly placed on. Therefore, taking integument measurement at this spot can address the constraint and obtain insights on the skin where it's particularly important for bio-logging tag practice.

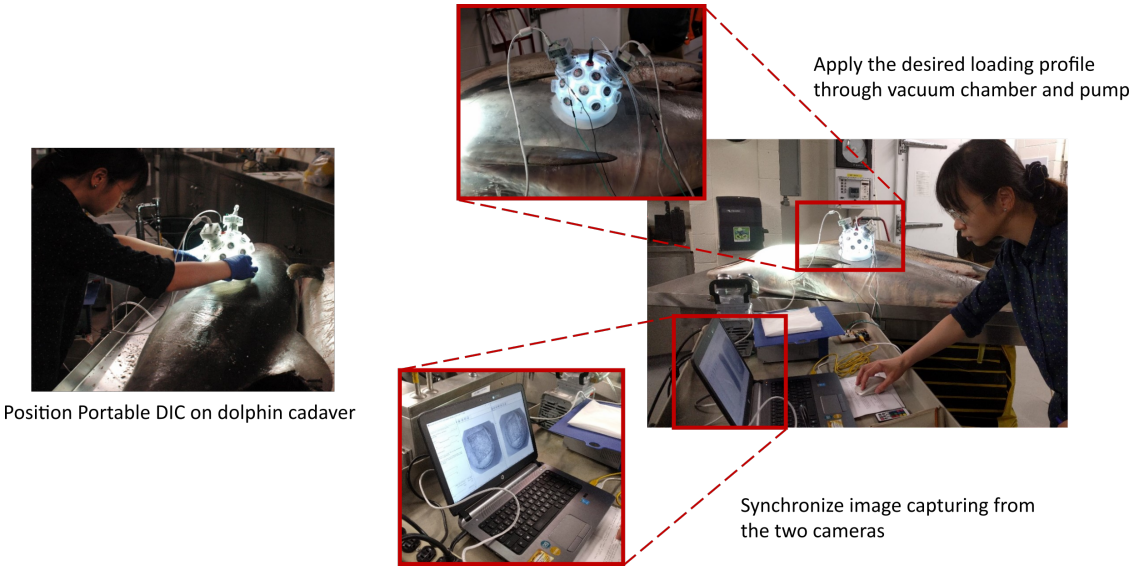

Figure 3.4: Experimental setup of the PDIC pilot study at WHOI.

3.3.3 Integument Constitutive Modeling, System Identification and Dynamic Mechanical Analysis

In this study, we established a paradigm to realize in-vivo cetacean integument characterization, shown in Figure 3.5, which contains three steps. First is integument measurement using PDIC (Figure 3.5 (a)), with the more detailed illustration of data collection process being covered in the following session. Second is selecting an appropriate viscoelastic model which can properly capture the cetacean integument response under vacuum loading (Figure 3.5 (c)). Last but not least is system identification (Figure 3.5 (b)), by importing the measured skin responses to the selected viscoelastic model, we can then determine the viscoelastic properties of the skin.

Various constitutive models were developed and used to represent the nonlinear elasticity, the viscoelasticity, and the dissipative behavior of skin (integument). These models can be classified into three different categories based on structural representation and complexity, which are phenomenological models, semi-structural models and semi-structural models with distributed fiber [108].

Tissue response in phenomenological models is typically represented by rubber-like materials or polymers, which are primarily based on empirical observations. Several examples of such models include the Ogden model, the Mooney-Rivlin model, and the Fung model [109, 110, 111, 112, 113, 114]. While these models are relatively easy to implement, they have limitations when it comes to capturing the anisotropic behavior of the tissue. As a result, the models may produce inconsistent results depending on factors like sample orientation, location on the body, or testing conditions. The parameters obtained from these models therefore can often lead to ambiguous interpretations, and they may lack clear physical meaning.

To address these limitations, from the beginning of semi-structural models, the constituents of the material, their corresponding mechanical behaviors, and the potential relative interactions in between were taken into account. The generalized Maxwell model [115] and the Bergström-Boyce model [116] are two of the iconic examples of semi-structural models. The major improvement of semi-structural models is that some characteristics of the material behavior can be attributed to corresponding specific constituents, or their structure [108]. Such as illustrating tissues' behaviors in restoration and energy dissipation as arrays of springs and dashpots. Skin (integument) can therefore be analyzed by distinguishing the contributions of constitutive fibers and the surrounding ground matrix. Anisotropy can therefore be incorporated by introducing fiber families aligned in preferred directions, while viscoelasticity can be attributed solely to the surrounding matrix [108]. Due to their increased level of complexity, semi-structural models often introduce considerably more parameters, which can be associated with specific components or physical processes within the tissue.

The last category, semi-structural models with distributed fiber shares similar features with semi-structural models with the major difference being the additional fiber families featured distributed orientations which allows a more generalized description of tissue response.

In this study, the standard linear solid (SLS) model was chosen to model the skin response. Also refereed as the Zener model, SLS model is a semi-structured constitutive model composed of a Kelvin-Voight solid unit in series with an elastic spring (Figure 3.5 (c)). With its' linear combination of springs and dashpots, SLS model is the simplest yet effective method in capturing both the creep and stress relaxation behaviors of a viscoelastic material, and therefore adopted. The governing equation of the SLS model is as below [117]:

$$(E_1 + E_2)\sigma + \eta\dot{\sigma} = E_1 E_2 \epsilon + E_1 \eta \dot{\epsilon} \tag{3.1}$$

with E_1 , E_2 , and η corresponding to the stiffness of the elastic spring, the stiffness of the Kelvin-Voight solid, and the damping coefficient of the Kelvin-Voight solid, respectively.

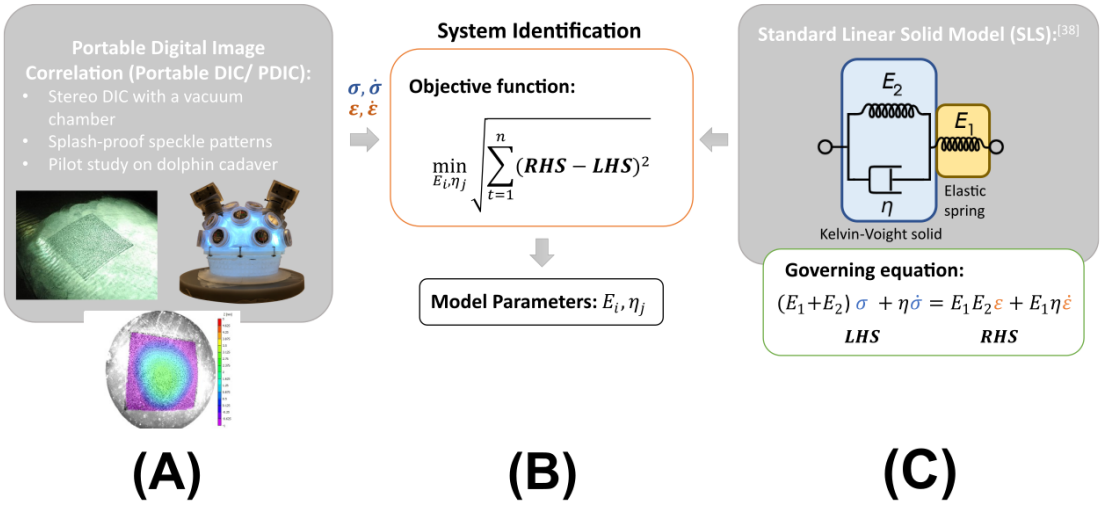

Figure 3.5: Paradigm for in-vivo cetacean skin characterization which consists three blocks: (A) data acquisition, (B) viscoelastic modeling, and (C) system identification.

After selecting the model, the data collected from the cadaver pilot study with PDIC were imported to identify the model parameters (Figure 3.5 (b)) by minimizing the objective function defined as the root sum square of the difference between the right hand side and the left hand side of the governing equation as follow:

$$\min_{E_1,E_2,\eta} \sqrt{\sum_{t=1}^{n}(\mathbf{RHS}-\mathbf{LHS})^2} \tag{3.2}$$

where $\mathbf{RHS} = E_1E_2\epsilon + E_1\eta\dot{\epsilon}$ and $\mathbf{LHS} = (E_1+E_2)\sigma + \eta\dot{\sigma}$.

On top of the system identification based on SLS model, we further conducted the dynamic mechanical (DMA) analysis with the cadaver data collected in PDIC pilot study. DMA is another approach widely used to characterize viscoelastic behavior of polymers. It is a straightforward way to gain an insight of the elastic and the viscous components of the integument by calculating the phase difference between an sinusoidal loading and the corresponding response. There are two types of dynamic moduli, storage modulus (E_S) and loss modulus (E_L), defined as follows [118]:

$$E_S = \frac{\sigma_{(t)}}{\epsilon_{(t)}} cos\delta \tag{3.3}$$

$$E_L = \frac{\sigma_{(t)}}{\epsilon_{(t)}} sin\delta \tag{3.4}$$

where stress ($\sigma_{(t)}$) and strain ($\epsilon_{(t)}$) are the sinusoidal input (loading) and output (response) of the measured system (cadaver integument), and δ represents the phase lag between $\sigma_{(t)}$ and $\epsilon_{(t)}$.

For a purely elastic material, $\sigma_{(t)}$ is proportional to $\epsilon_{(t)}$, without any phase difference ($\delta = 0$). In contrast, for a purely viscous material, $\sigma_{(t)}$ is proportional to strain rate ($\dot{\sigma}_{(t)}$) instead, and the lag is 90 degrees ($\delta = \frac{\pi}{2}$) [118]. For any material contains both elastic and viscous features, the the phase lag therefore falls between 0 and 90 degrees ($0 < \delta < \frac{\pi}{2}$), with the value of δ showcases whether the elastic or the viscous component is more dominant in the measured system. By conduction DMA, it provide us a way to validate the system identification results.

3.3.4 Data Collection

The schematics of PDIC data collection and processing procedure is presented as the block diagram shown in Figure 3.6. The input to the system (cetacean integument) is the designed sinusoidal pressure differential ($\Delta P_r(t)$) loading. The microcontroller (ARDUINO UNO REV3, Arduino, Italy) is used to execute clock control on both the cameras and the pressure transducer embedded in PDIC to take a sequence of patterned images and record the measured pressure differential ($\Delta P_m(t)$) simultaneously. $\Delta P_m(t)$ is then fed back into the system, based on the error between $\Delta P_r(t)$ and $\Delta P_m(t)$, the microcontroller executes bang-bang control to switch the state (on/off) of the solenoid valve connected to the pump accordingly to regulate $\Delta P(t)$ inside the PDIC chamber.

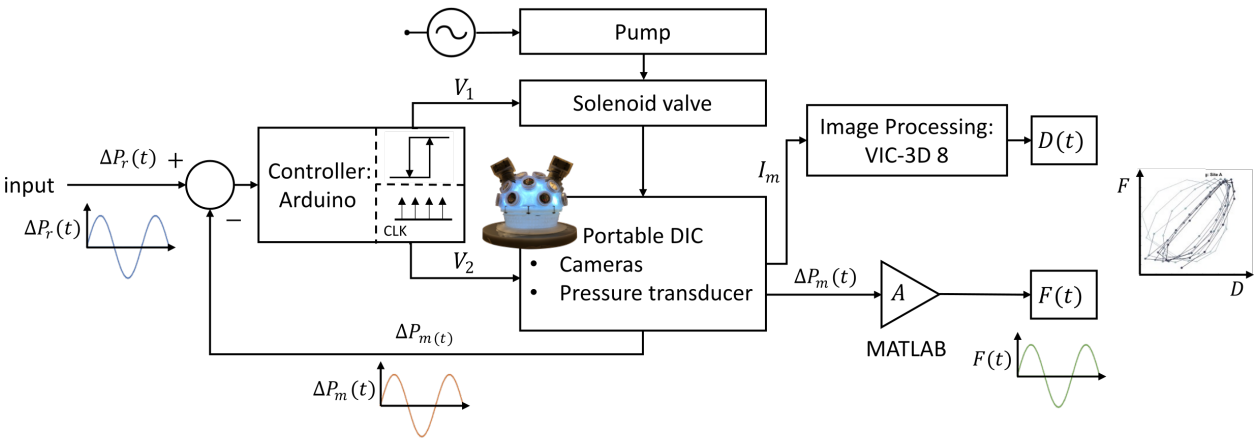

Figure 3.6: The block diagram showcasing the data collecting and processing procedure of PDIC (Portable Digital Image Correlation) system. A microcontroller (ARDUINO UNO REV3, Arduino, Italy) and a pump are incorporated to regulate $\Delta P(t)$ inside the PDIC chamber to trace the designed loading profile ($\Delta P_r(t)$).

The sequence of the patterned images from the stereo cameras were then processed using a DIC software, VIC-3D 8 (Correlated Solutions, Irmo, SC, USA), to obtain integument displacement over time. The $\Delta P_m(t)$, on the other hand, were processed using Matlab (MathWorks, Natick, MA, USA) to estimate the corresponding force applied to the system. With these information, the force ($F(t)$) - displacement ($D(t)$) relationship of the integument response can be established and used to calculate the corresponding stress (σ) and strain (ϵ) as follow:

$$\sigma = F(t)/A_{PDIC}\ (kPa) \tag{3.5}$$

$$\epsilon = \frac{D(t) - D_{min}}{\Delta \bar{D}}\ (\%) \tag{3.6}$$

where A_{PDIC} is the cross sectional area of PDIC, $D(t)$ is the peak integument displacement over time, D_{min} and $\Delta \bar{D}$ represent the minimum peak displacement and the average peak-to-valley difference of $D(t)$ within the steady state. Once the stress (σ)-strain (ϵ) correlation is established, the system identification and DMA can be executed.

3.4 Results

The stress (σ) and strain (ϵ) of the skin (integument) were calculated and presented in Figure 3.7(a). We then identified and examined the steady-state response of the skin (the last 5 cycles enclosed

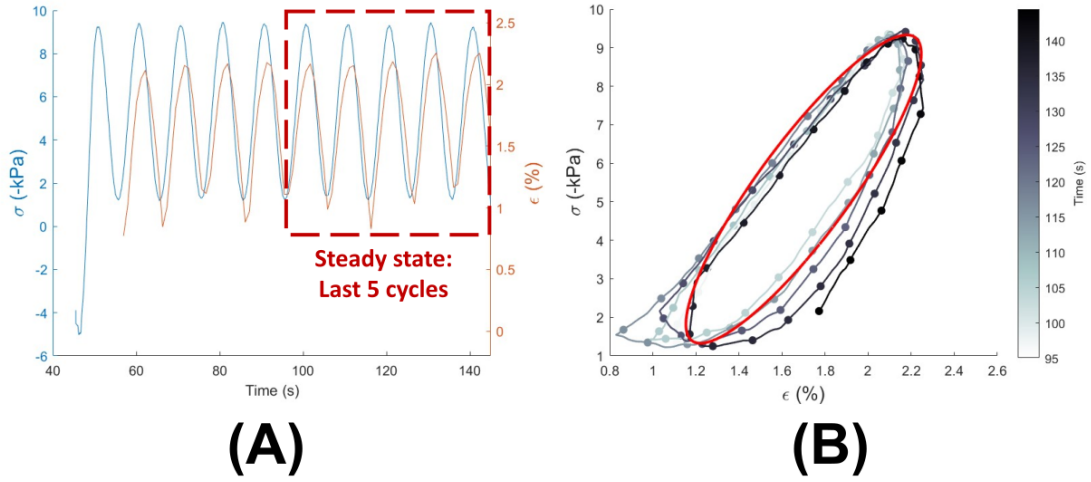

Figure 3.7: Cadaver skin (integument) analysis results: (A) Stress (σ) and strain (ϵ) correlation during the trial, with the last five cycles (100 - 145 seconds) identified as steady-state response; (B) Comparison between the simulated skin (integument) response based on the SLS (Standard Linear Solid) model parameters (red curve) and the calculated stress (σ) - strain (ϵ) from experimental measurements (gradient dotted line, with color indicating the corresponding timestamp).

by the red dashed box) so as to focus on the behaviors of constitutive fibers while decoupling the contributions from the surrounding ground matrix. In the next step, to find out the dominant amplitude and frequency for further analysis, both the input (σ) and the response (ϵ) were processed with fast Fourier transform (FFT) to filter out the noises, and later reconstructed using inverse fast Fourier transform (IFFT). The results of the filtered and reconstructed signals are as follow:

$$\sigma = 4.00\ sin(0.6290t + 0.5018) + 5.3288\ (kPa) \tag{3.7}$$

$$\epsilon = 0.55\ sin(0.6290t) + 1.7000\ (\%) \tag{3.8}$$

where frequency and amplitude are $\omega_\sigma = 0.6290\ rad/s$, $A_\sigma = 4.00\ kPa$ for the input signal (σ); $\omega_\epsilon = 0.6290\ rad/s$, $A_\epsilon = 0.55\ kPa$ for the output signal (ϵ), and the phase angle (δ) difference is $0.5018\ rad$.

With the above information, stress rate ($\dot{\sigma}$) and strain rate ($\dot{\epsilon}$) can be calculated by taking the 1st-order derivative with respect to (wrt) time:

$$\dot{\sigma} = 2.52\ cos(0.6290t + 0.5018)\ (kPat^{-1}) \tag{3.9}$$

$$\dot{\epsilon} = 0.35\ cos(0.6290t)\ (\%t^{-1}) \tag{3.10}$$

The frequencies (ω_σ, ω_ϵ, $\omega_{\dot{\sigma}}$, $\omega_{\dot{\epsilon}}$), amplitudes (A_σ, A_ϵ, $A_{\dot{\sigma}}$, $A_{\dot{\epsilon}}$) and phase angles (δ) of the input (σ), input rate ($\dot{\sigma}$), response (ϵ), and response rate ($\dot{\epsilon}$) were used to conduct system identification using Eq 3.2, and the three skin (integument) properties for SLS model are derived as follow:

$$E_1 = 1.02\ (MPa) \tag{3.11}$$

$$E_2 = 0.45\ (MPa) \tag{3.12}$$

$$\eta = 2.18\ (MPa - s) \tag{3.13}$$

To verify the feasibility of the system identification result, the same sinusoidal pressure loading (σ) were inputted into the SLS model to simulate the response (ϵ_{model}). The comparison between the modeled and the measured skin response is presented in Figure 3.7(b), with the red contour being the modeled skin response (ϵ_{model}) and the gradient line in the background showing the measured data set chronologically. The result showcases that the modeled response compares well with the experimental measurements with $R^2 = 0.9210$, and serve as an initial verification for the feasibility of the cetacean skin (integument) characterization paradigm.

For dynamic mechanical analysis (DMA), the ratio ($tan\delta$) between the storage modulus (E_S) and loss modulus (E_L) characterize energy storage and dissipation. The phase lag (δ) between $\sigma_{(t)}$ and $\epsilon_{(t)}$ is 0.5018 rad, and the ratio is 0.55. This value indicates the loss modulus (E_L) that is about half of the storage modulus (E_S), indicating that the dolphin cadaver skin is more prone to restore energy (elastic) than dissipate (viscous).

3.5 Discussion

In this chapter, a novel device called the PDIC system is introduced for the characterization of in vivo cetacean integument. The device combines DIC with vacuum loading to simulate the loading conditions under the case of suction-based bio-logging tags on compliant tissue (integument). To generate the desired speckle pattern, a customized stamping equipment and method specifically designed for compliant tissue are developed. A pilot study is conducted on a dolphin cadaver using the proposed data collection and analysis framework. System identification is performed using SLS models, and the measured skin characteristics are consistently demonstrated through

DMA.

In addition to the promising results obtained, our team encountered several challenges with the current experimental setup which need to be further addressed. First is the dripping issue with the powdered white base coat applied before stamping the custom speckle pattern. Due to the temperature difference between the environment and the cadaver, the current base coat product cannot adhere well on skin with moisture. To overcome this, we plan to explore waterproof and long-lasting cosmetic products that can attach to skin and enhance the contrast and sharpness of the speckled pattern. Secondly, we experienced insufficient and unsustainable lighting during our experiments. The current model of the PDIC system utilizes 18 battery-powered LED units, which drain quickly and gradually dim. This necessitated the use of additional lighting during the experiments. In the next generation of the PDIC system, our team will seek and incorporate lighting options which are more power-efficient, durable and stable. Lastly, the diameter of the PDIC system posed a challenge. Since the pilot study conducted on a small animal cadaver, there were limitations in terms of available testing spots. The PDIC system needs to conform entirely to the body profile to create an enclosed chamber for vacuum. For future model, our team will consider the body shape and size of different cetaceans and revise the PDIC diameter accordingly.

3.6 Summary

Measuring cetacean integument in vivo presents several inherent challenges, and this study represents an initial proof of concept for the feasibility of the PDIC system. In the next stage, a comprehensive review will be conducted to assess the practicality of the system, with a focus on preparing the device for live animal experiments. This review will explore various perspectives, including but not limited to waterproof packaging, transitioning to wireless operation, and reducing the overall weight and size of the system.

Regarding the experimental protocol, factors such as the size, body profile, and specific measuring spots (ex. the preferable spots to attach suction cup bio-logging tag) of the animal will be taken into account. Various parameters will be considered, including different initial setup pressure differentials (ΔP_i), frequency (ω) and amplitude (A) sweeps, as well as other loading profiles like creep and stress relaxation. These experiments aim to provide a more in-depth characterization of the cetacean integument.

In future integument modeling endeavors, our plan is to utilize the extensive data gathered from full-field measurements to advance tissue characterization in two dimensions. This will involve exploring parameters such as anisotropy and comparing nonhomogeneity and viscoelasticity across different preferred bio-logging tag attachment sites. By obtaining a deeper understanding of cetacean integument through these analyses, our objective is to design and create a cetacean skin

phantom. The cetacean skin phantom will serve as a representation of the real integument, either as a single material that closely resembles its bulk material properties or as a multi-layered structure with various components. This will allow us to closely mimic the features of real cetacean skin. The purpose of the phantom will be to assist in in-lab suction cup examinations and aid in the design process. By utilizing the data-driven insights and improved understanding of cetacean integument, the development of a cetacean skin phantom will provide a valuable tool for further research and experimentation in a controlled laboratory environment.

CHAPTER 4

Suction Cup: Characterization and Modeling

4.1 Problem Statement

Suction cups play a critical role in securing bio-logging tag onto compliant cetacean integument (skin), which greatly influences the reliability of collected data. However, with the current practice and suction cup design, phenomenon of early detachment as well as drifting from the original attachment spot are commonly observed during field studies. Based on biologists' experiences and the specific species they work with, each has own preferences of the suction cup that works better for their case. However, the objective methods to quantify and compare performance of different suction cup designs under various loading conditions are lacking. Further, the relationship between key design features and cup performance on a compliant substrate is still an open question. As introduced in Chapter 2, my preliminary work demonstrated how differently the same (Nitrile rubber) suction cup can perform under normal loading when attached to two substrates with distinct (rigid vs. compliant) impedance. In this chapter, I will extend this investigation to better understand why suction cups fail and what's the corresponding loading limits before failures. Specifically, I will:

Task 1: Establish a generalized suction cup kinetic model to illustrate the dynamics between the suction cup - integument interaction, and as criteria for suction cup performance quantification.

Task 2: Based on Task 1, identify suction cup characteristics related to its' performance, then design and conduct experiments to evaluate these features quantitatively.

Task 3: Decoupled and build corresponding experiments to examine the loading limit of suction cups under each specific failure mode.

4.2 Methods

4.2.1 Suction Cup - Kinetic Modeling

Animal locomotion induces hydrodynamic force (F_H) which loads the suction cups on bio-logging tag in both normal ($\hat{\jmath}$) and shear ($\hat{\imath}$) direction. To model the kinetics of a suction cup attaching to compliant integument, the following assumptions were made to simplify the system:

1. The suction cup - substrate system is quasi-static during constant rate loading in lab and while the animal is traveling at a steady-state speed.
2. Neutral height ($H_{SC,o}$) of a suction cup is used as the reference datum of the cup state.
3. Buoyancy force (F_b) and gravity force (F_{mg}) are negligible since both are relatively small when compared to other applied forces.
4. Externally applied forces pass through the center of mass (COM) of the cup.
5. The radial resistance force ($\overrightarrow{f}^{\,r}_{\theta}$) preventing a suction cup from entirely restoring its' shape is symmetrical. Therefore the net radial resistance force is zero ($\sum_0^{2\pi} \overrightarrow{f}^{\,r}_{\theta} = 0$).

Based on the aforementioned assumptions, our suction cup kinetic model focuses primarily on elucidating the steady-state behaviors and performances of the cup under conditions where the host animal, such as a cetacean, maintains a relatively consistent speed and depth during travel. While it is acknowledged that real-world suction cup failures are more prone to occur during dynamic occurrences like breaching and rubbing—instances marked by significantly distinct loadings compared to steady-state situations—our established suction cup kinetic model holds substantial value as a fundamental reference point for quantifying and comparing suction cup performances.

To better illustrate how a suction cup responds to external loading, the hydrodynamic force (F_H) is decoupled into pulling force (F_P) in normal direction and drag force (F_D) in shear direction, and the two cases were analyzed individually. After setting up a suction cup on cetacean skin (Figure 1.6), We firstly start by applying pulling force (F_P) to the system. From the perspective of the suction cup, the force equilibrium is achieved as below in normal direction:

$$\hat{\jmath}\ direction : F_V + F_{env} + F^r_{\perp} = N + F_P \tag{4.1}$$

where $F_V (= \Delta P A_v)$ is vacuum force , $F_{env} (= p_o A_c)$ is environmental force , $F^r_{\perp} (= \Sigma f^r_{\perp})$ is the sum of friction force in $\hat{\jmath}$ axis, and N $(= \Sigma f^n_{\perp})$ is normal force on A_c.

The state of a suction cup can be further segmented into three stages based on its' height with respect to the reference datum (the neutral height: H_{SC}). At the beginning, with a small pulling force (F_P), the suction cup is still in compression (Figure 4.1 (A)). As the pulling force (F_P) increases, the suction cup will then return to its' original height ((Figure 4.1 (B)), follow by stretching into extension state (Figure 4.1 (C)). Looking only at the force equilibrium on vacuum area (A_v), the state can be express as:

$$\hat{\jmath}\ direction : F_V = F_P + F_{SC} \tag{4.2}$$

here, F_{SC} is the spring force coming from suction cup deformation. Analogize the suction cup as a spring, on the vacuum area (A_v), F_V and F_P load the spring in opposite direction. Therefore, based on the suction cup's state, F_{SC} could be either direction or equal to zero.

Next, for the case of applying drag force (F_D) only. Similarly, we start with a small drag force (F_D) where the suction cup is static (Figure 4.1 (D)), then gradually increase to the magnitude of the maximum static friction force ($f_{s,max}$) (Figure 4.1 (E)) when the sliding is about to initiate, and finally the suction cup start to slide on the substrate (Figure 4.1 (E)). The force equilibrium stated is:

$$\hat{\imath}\ direction : F_D = F_{||}^r \begin{cases} \leq \mu_s N = f_{s,max}, & \text{static or about to slide} \\ \geq \mu_k N = f_k, & \text{sliding} \end{cases} \tag{4.3}$$

Both normal force (N) and friction force (f) act merely on contact area (A_c) where the suction cup lip is in contact with the substrate, and the values of the static (μ_s) and dynamic (μ_k) friction coefficients are unique to each suction cup - skin combination. Now, taking a closer look at the $\hat{\jmath}$ direction of A_c, the force equilibrium can be express as:

$$\hat{\jmath}\ direction : F_{env} + F_{\perp}^r + F_{SC} = N \tag{4.4}$$

here, we again analogize the suction cup as a spring, on the contact area (A_c), F_{env} and N load the spring in opposite direction. One key point is that F_{SC} on A_c being the same amount but in the opposite direction as the one on A_v based on both continuum mechanics and the spring's nature to restore its' neutral position. $F_{\perp}^r$ is the summation of friction force projected on $\hat{\jmath}$ axis. Since the major component of friction force ($F_{||}^r$) is to resist movement in $\hat{\imath}$ direction, we opt to neglect $F_{\perp}^r$ to simplify the above equation into:

$$\hat{\jmath}\ direction : F_{env} + F_{SC} = N \tag{4.5}$$

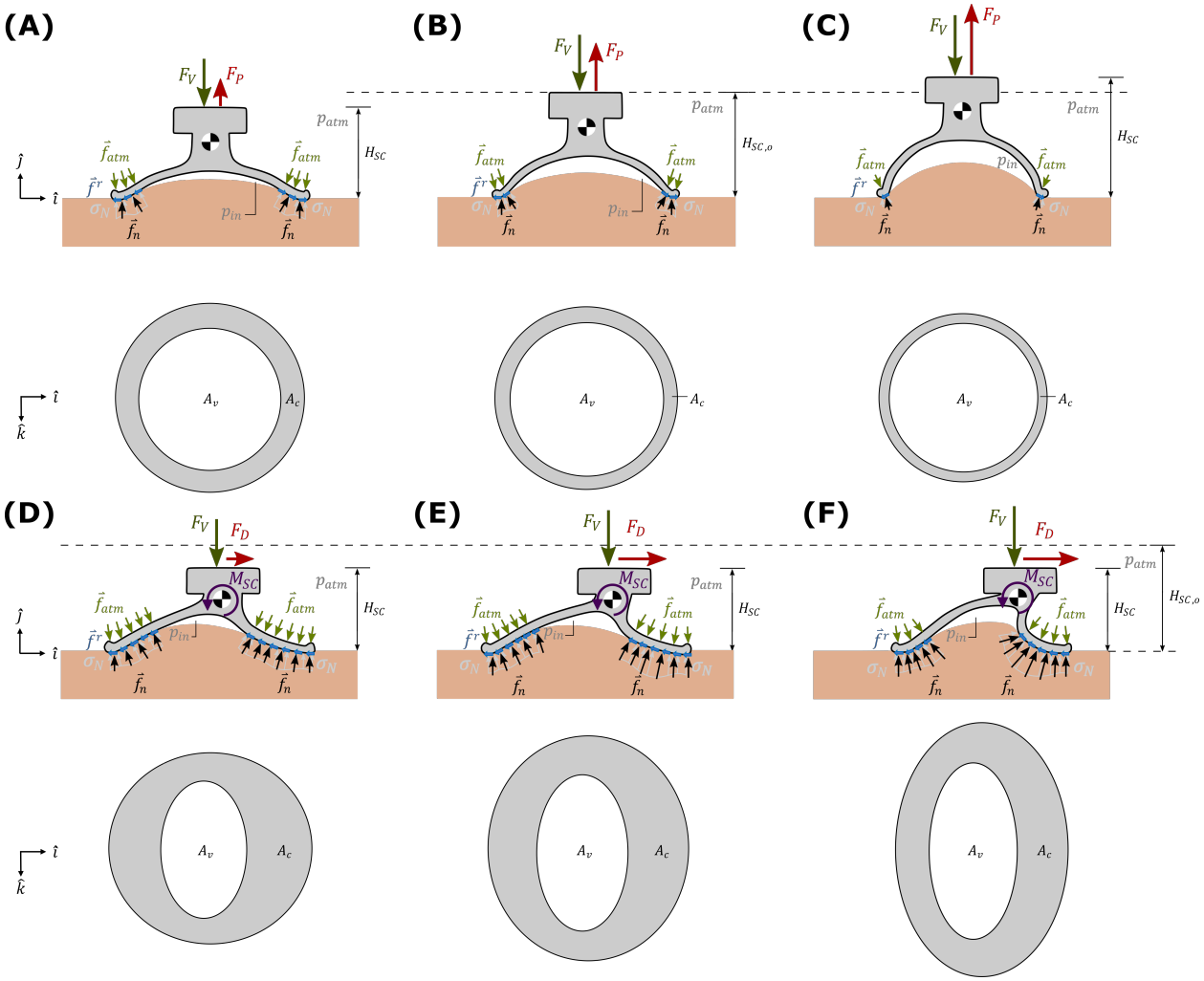

Figure 4.1: Suction cup under normal and shear loading conditions. When loaded in normal direction, suction cup kinetics can be categorized into three states: (A) start to apply pulling force (F_P), suction cup in compression; (B) gradually increase pulling force (F_P), suction cup returns to its' natural height; and (C) continue to increase pulling force (F_P), suction cup turn into tension, and it will detach once vacuum force (F_V) reaches limit. Suction cup states can also be divided into three types when shear loading is applied: (D) start to apply drag force ($F_D \leq F_{s,max}$), suction cup is static; (E) gradually increase drag force ($F_D = F_{s,max} = \mu_S N$), suction cup is about to slide; and (F) continue to increase drag force ($F_D \geq F_d = \mu_d N$), suction cup become dynamic.

Finally, on $\hat{k}$ axis, the drag force (F_D) and the friction force ($F_{||}^r$) create a moment that is balanced by the moment ($\mathbf{M_{SC}}$) generated via cup deformation:

$$\hat{k}\ direction: \sum \mathbf{M_{com}} = \overrightarrow{F_D} \times -\overrightarrow{r} + (-\overrightarrow{F_{||}^r}) \times \overrightarrow{r} + \mathbf{M_{SC}} = 0 \tag{4.6}$$

where $\overrightarrow{r}$ is the vertical distance from the applied force to COM, approximately the half of suction cup height (H_{SC}). Since $\overrightarrow{F_D}$ and $\overrightarrow{F_{||}^r}$ are same in magnitude and opposite in direction, the above relation can be rewrite as:

$$\hat{k}\ direction: \overrightarrow{F_D} \times \overrightarrow{H_{SC}} = \mathbf{M_{SC}} \tag{4.7}$$

With these equations, We now have a generalized kinetic model to help investigate suction cup overall response as a single unit as well as studying how it behaves internally by individual sections (A_v and A_c).

4.2.2 Suction Cup - Characterization

From the process of developing the generalized suction cup model, it is found that there are two critical components which are unique to each suction cup design and would need further research. These two features are highly correlated to suction cup material, geometry and its' deformation as a whole.

4.2.2.1 Suction Cup Stiffness

The first component is the spring restoration force (F_{SC}). By analogizing a suction cup as a linear spring on $\hat{j}$ axis, we are able to parameterize the mapping from deformation (ΔH_{SC}) to force (F_{SC}), and use the equivalent linear stiffness (k_{SC}^L) of the suction cup to estimate the spring force (F_{SC}) at each state accordingly.

Due to the shape and material distribution, a suction cup doesn't behave as a perfect linear spring, meaning the $\Delta H_{SC} - F_{SC}$ correlation cannot be fully captured with a 1^{st} order regression. However, as the pioneer study for suction cup characterizing, we reckon this simplified bulk property (k_{sc}^L) is well enough to used as criteria to distinguish different suction cup designs.

The experimental setup specifically designed for suction cup stiffness (k_{SC}^L) characterization is shown in Figure 4.2 (A). To decouple the vacuum force (F_V) from the measurement, the tested suction cup has a channel connecting the inside of the bell to the surrounding environment. A set of three 3D-printed stages were fastened on ball bearing carriages sitting on guide rails which are

120^o apart from each other. The entire fixture allows suction cup to expand freely in radial direction without being constrained by friction force (f). The suction cup is placed on the stages and mounted to the load cell. The test is conducted on a uniaxial extension testing machine (Instron, USA), starting from the suction cup's neutral height ($H_{SC,o}$) then gradually pushing it against the platform until the suction cup is fully flattened. The suction cup height difference (ΔH_{SC}) and the applied force during the process were recorded.

4.2.2.2 Area Analysis

The second feature unique to each suction cup design is the area ($A_v - A_c$) distribution profiles during the loading process. The sizes of vacuum (A_v) and contact (A_c) areas have direct influence on the magnitude of vacuum force ($F_V = \Delta P A_v$) and the environmental force ($F_{env} = p_o A_c$), which will further affect the estimation of other force terms in the kinetic model. The area distribution of a suction cup at each state is resulted from the integral effect of suction cup material and geometry. Therefore, it is important to build the correlation between the area profile distribution ($A_v - A_c$) wrt the corresponding pressure differential (ΔP).

Figure 4.2 (B) showcases the experimental setup designed for the area study. This time, a tubing is connected between the suction cup bell and a pressure transducer (ABPDANT600MDAA5, Honeywell, Charlotte, NC, USA) with the measurement of pressure differential (ΔP) processed and logged by a microcontroller (ARDUINO UNO REV3, Arduino, Italy). The suction cup is mounted on a load cell of a uniaxial extension testing machine (Instron, USA), started with the initial setup on an elevated transparent platform, the load is applied and gradually increased until the suction cup is detached from the platform. Meanwhile, a camera is recording the area profiles from beneath. With these information, the video footage can be processed to estimate the size of vacuum (A_v) and contact (A_c) area and synchronize with the corresponding pressure differential (ΔP), which can be used to assist kinetic analysis.

4.2.3 Suction Cup - Failure Modes and Experimental Setup

Suction cup failure is defined as undesirable detachment or sliding from it's original attachment spot. Quantifying the loading limits of a suction cup before failure setup an objective criteria to compare the performances between different suction cup design. In my research, I will study the three types of suction cups currently used for bio-logging tags. The first type is a hybrid cup with Neoprene body and silicone lip, the second type is Nitrile Rubber cup, and the last one is silicone cup (shown in Figure 4.4 as legend). These three designs share the same geometry with the materials being the only difference.

In order to comprehensively compare the performance of the cups from various perspectives, I

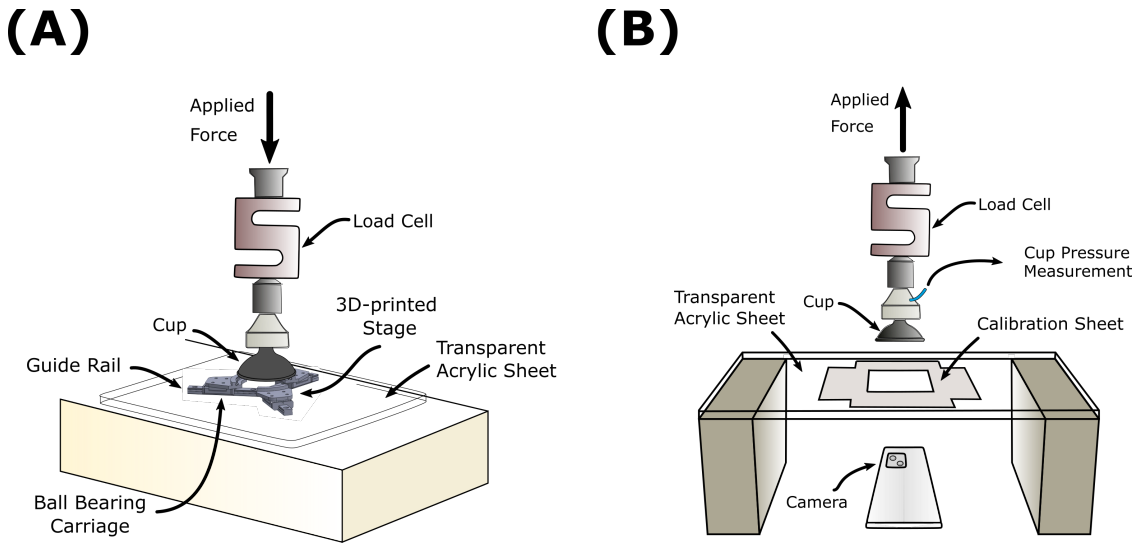

Figure 4.2: Experimental setups for suction cup characterization: (A) Linear stiffness (k_{SC}^{L}) is the mapping between suction cup height difference ($\Delta H_{SC} = H_{SC} - H_{SC,o}$) and spring restoration force (F_{SC}); (B) Area ($A_v - A_c$) analysis can be used to calculate vacuum force ($F_V = \Delta P A_v$) and environmental force ($F_{env} = p_o A_c$), which can be further used to estimate other force terms in the suction cup kinetic model.

define three suction cup failure modes to decouple the time - effect as well as isolating the loading on different axes. The specific experimental setup for each failure mode is presented in Figure 4.3.

The first failure mode is leakage over time. The purpose of this test is to investigate how pressure differential (ΔP) drop without applying load to the system. The three suction cups were setup on the compliant substrate phantom made of A10 hardness silicone rubber (Dragon Skin™ 10 SLOW, Smooth-On, Inc., Macungie, PA, USA) selected based on Table 2.2. The pressure transducer (ABPDANT600MDAA5, Honeywell, Charlotte, NC, USA) connects to the interior of the suction cup bell through a tubing, and a microcontroller (ARDUINO UNO REV3, Arduino, Italy) logs the pressure differential (ΔP) over the 24 hrs (Figure 4.3 (A)). The experiments were conducted both in air and water to see how medium affect the leakage rate.

To quantify the leakage behavior, the decrease of pressure differential (ΔP) over time was modeled as an exponential decay and a leakage time constant (τ_{leak}) can be derived as:

$$\Delta P(t) = \Delta P_{int}(e^{-24/\tau_{leak}}) \tag{4.8}$$

$$\tau_{leak} = -24/ln(\Delta P_{24}/\Delta P_{int}) \tag{4.9}$$

where ΔP_{int} and ΔP_{24} represent the initial setup pressure differential and the pressure differential after 24 hours, respectively.

The second failure mode is the detachment under normal loading. The same experimental setup

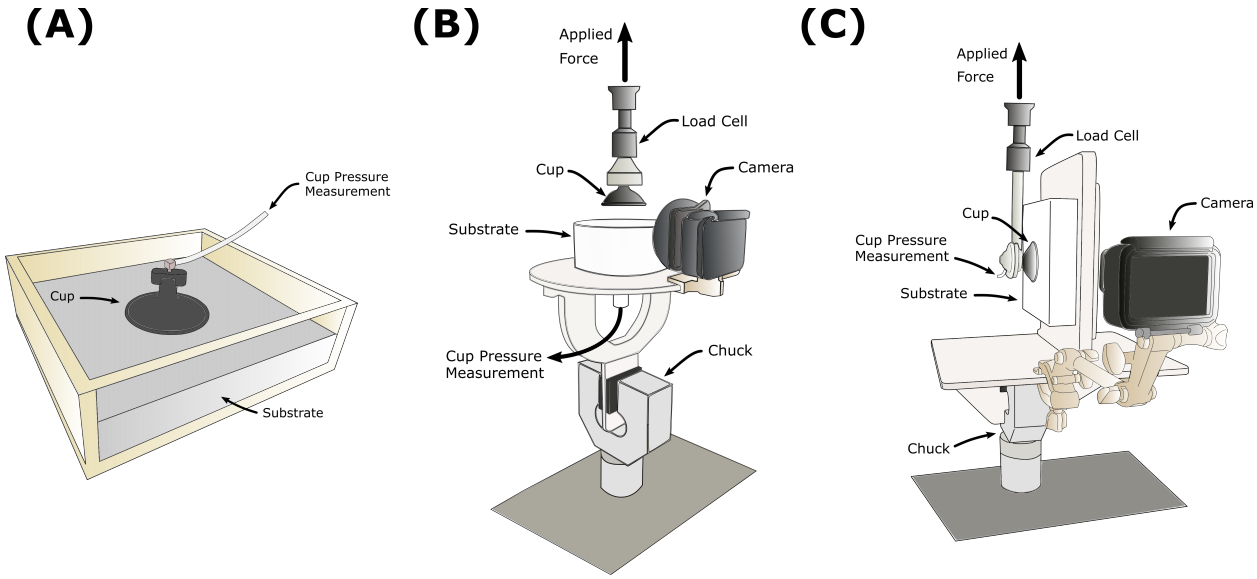

Figure 4.3: Experimental setups to examine suction cup performances under (A) leakage, (B) normal loading, and (C) shear loading. Pressure differential (ΔP) fluctuation during trials is measured. On top of that, the magnitude of the applied load, suction cup displacement and deformation are also recorded for the (B) normal and (C) shear loading tests.

presented in Session 2.2.2 was used to compare the normal loading limits of the three suction cups. With the pulling force (F_P) and the system displacement (D_{sys}) measured from the uniaxial extension testing machine (4301, Instron, USA), and the monitored pressure differential (ΔP) along with the camera footage, we are able to decompose the forces acting vacuum area (A_v) and obtain a more profound insight regarding the suction cup deformation with respect to its' material stiffness and the ability to sustain loading in normal direction.

Lastly, the third failure mode is sliding under shear loading. This is suspected to be a significant cause of bio-logging tag detachment. This hypothesis is informed by observations of animal locomotion (speed and acceleration) as well as data from the retrieved bio-logging tags.

To evaluate suction cup performances under shear loading, I design the experimental setup shown in Figure 4.3 (C). Similar to the normal test (Figure 4.3 (B)), a universal tester (4301, Instron, USA) was used to load the suction cup at a constant rate ($60\ mm/min$) in shear direction until failure. The drag force (F_D) and the sliding distance were measured by the universal tester as well. The corresponding pressure differential (ΔP) between the cup (p_v) and the environment (p_o) was monitored via a pressure transducer (ABPDANT600MDAA5, Honeywell, Charlotte, NC, USA) from the initial setup state till the moment the suction cup detached from the substrate phantom. A fixed camera (HERO 5, GoPro, USA) recorded suction cup deformation during the experiment at 25 frames per second (FPS). The video data were used to estimate the vacuum area (A_v) and the suction cup height (H_{SC}). The three suction cup designs were tested ten times each.

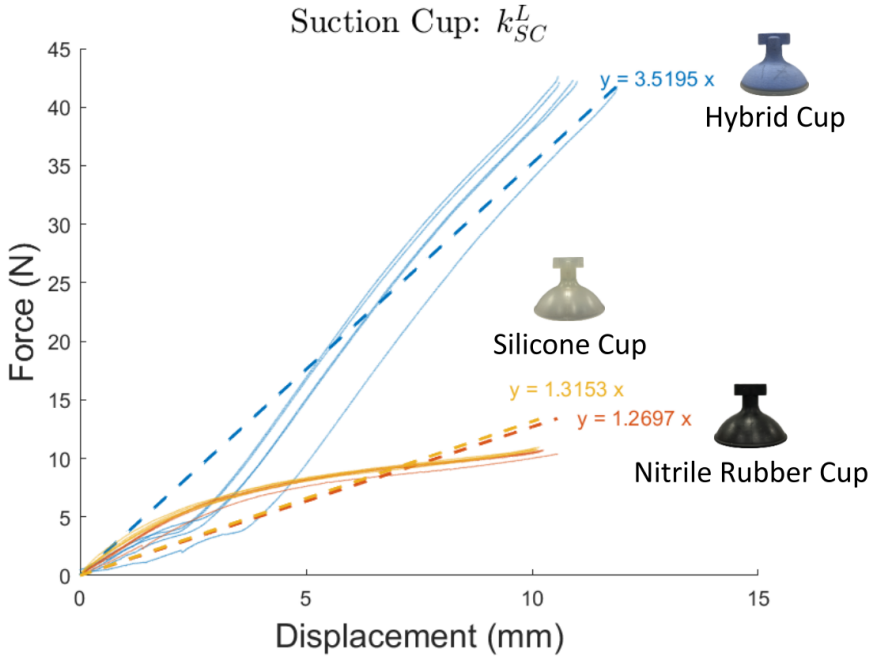

Figure 4.4: Suction cup linear stiffness (k_{SC}^L). The linear stiffness k_{SC}^L along $\hat{\jmath}$ axis of the three suction cups all demonstrate nonlinear behaviors during tests. To simplified the modeling, the 1^{st} order linear regression model is adopted to extract k_{SC}^L. Among the three cups, Hybrid cup has the significant higher k_{SC}^L, while the values for the Nitrile Rubber cup and Silicone cup are similar.

Suction cups were secured to the substrate phantom (Dragon Skin™ 10 SLOW, Smooth-On, Inc., Macungie, PA, USA) by hand and water was applied to the surface before the cup was attached to mimic the cetacean skin condition.

4.3 Results

During this session, we will present the outcomes derived from the suction cup characterization and failure mode tests, highlighting significant discoveries and key findings.

4.3.1 Suction Cup Linear Stiffness vs. Material Force

The relationship between the applied force (F) versus suction cup height difference (ΔH_{SC}) is presented in Figure 4.4. This mapping showcases the amount of force in need to compress suction cup in $\hat{\jmath}$ direction. It was observed that each of the three types of suction cups exhibits a two-stage deformation pattern. The Silicon and Nitrile Rubber cups display a comparable convex curve, characterized by an initial steeper slope followed by a gentler one, while the Hybrid cup shows

the reverse behavior. This dual-stage relationship between force and deformation predominantly arises from the unique shape and material composition of the suction cup. A steeper slope indicates a more substantial deformation per unit of applied force, whereas a gradual incline signifies the opposite. This phenomenon underscores the non-uniform deformation of a suction cup, which initiates from a relatively compliant region of the structure.

As stated in Session 4.2.2.1, to capture the bulk behavior of a suction cup, the 1^{st}-order linear regression is adopted to fit the curves (shown as dashed lines, Figure 4.4) to find out the corresponding linear stiffness (k_{SC}^{L}). Among the three, the Hybrid cup has a significant larger k_{SC}^{L}, 3.5195 (N/mm). While the other two have pretty close values, 1.3153 (N/mm) and 1.2697 (N/mm) for Silicone and Nitrile rubber cup, respectively.

4.3.2 Area Composition

The area study results are presented in Figure 4.5, which are Hybrid ((A)), Nitrile Rubber ((B)), and Silicone ((C)) cup, respectively. On the top of the area composition sub figures are the initial setup state of each cup, with the corresponding initial setup pressure differential (ΔP_i) and the snapshot of the area composition at the moment. Hybrid cup ((A)) starts at $\Delta P_i = 0.25\,bar$, with $A_v - A_c$ ratio being about $6:4$. The other two cups share similar behaviors, with $\Delta P_i = 0.12\,bar$ and $A_v - A_c$ ratio being about $5.5:4.5$.

The area analysis covers the time span from the initial setup to the last video frame before suction cup detachment. The change of area composition is normalized to % Trial for better comparison, with the states of 0, 25, 50, 75, 100% Trial shown as examples on the top of the area composition sub figures.

It is found that the three cups go through an alike trend, where A_v stays relatively constant during the entire loading process, while the major area drop happens on A_c. This phenomena provides the insight that vacuum force F_V ($= \Delta P A_v$) is largely depending on the pressure differential (ΔP) a suction cup can generate during the loading process. It also matches the physical fact that the normal force ($N = p_o A_c$) is gradually decreasing with contact area (A_c) and the trial will fail in an abrupt matter, where A_c and N suddenly return to zero at the moment of detachment.

4.3.3 Leakage

In the leakage test, we measured the change of the pressure differential (ΔP) of the three suction cups over the 24-hour period in two mediums. The pressure differential ($\Delta P(t)$) decay curves are shown in Figure 4.6 for air ((A)) and water ((B)). With the exponential decay model introduced previously, the corresponding average leakage time constant ($\tau_{leak,avg}$) can be evaluated, along with

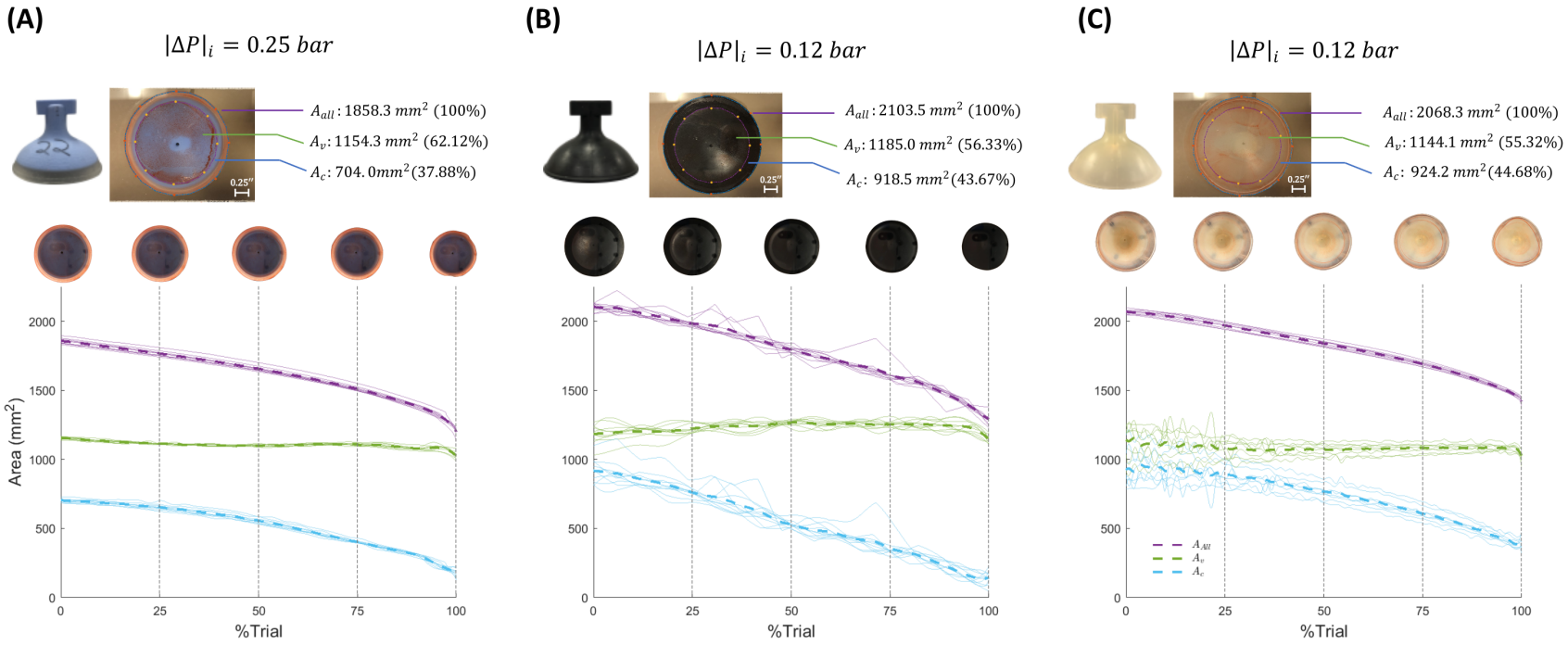

Figure 4.5: Suction cup area analysis results: (A) Hybrid cup (B) Nitrile Rubber cup and (C) Silicone cup. The top sub figures are the initial setup state of each cup, with the corresponding initial setup pressure differential (ΔP_i) and the snapshot of the area composition at the moment. The area composition states of $0,\ 25,\ 50,\ 75,\ 100\%$ Trial are presented as well.

Table 4.1: Leakage Test Result: the three suction cups (Hybrid, Nitrile Rubber, and Silicone) were tested in air and water for 24 hours. The Nitrile Rubber cup has the largest average leakage time constant ($\tau_{leak,avg}$), while Hybrid cup has the largest average initial setup pressure differential ($\Delta P_{int,avg}$), and the average pressure differential change rate ($\dot{\Delta P}_{avg}$).

Medium	Air		
	$\tau_{leak,avg}\ (hrs)$	$\Delta P_{int,avg}\ (bar)$	$\dot{\Delta P}_{avg}\ (bar/hr)$
Hybrid	23.58	0.312	0.0084
Nitrile rubber	68.00	0.149	0.0020
Silicone	27.69	0.147	0.0036
Medium	Water		
	$\tau_{leak,avg}\ (hrs)$	$\Delta P_{int,avg}\ (bar)$	$\dot{\Delta P}_{avg}\ (bar/hr)$
Hybrid	42.27	0.298	0.0056
Nitrile rubber	95.29	0.169	0.0018
Silicone	60.25	0.148	0.0022

the average initial setup pressure differential ($\Delta P_{int,avg}$), and average pressure differential change rate ($\dot{\Delta P}_{avg}$) are reported in Table 4.1.

Based on these findings, it becomes evident that the suction cup's leakage behavior is comparatively slower in water compared to its performance in air. Our initial hypothesis attributes this variance to the molecular size of the medium. Specifically, the larger molecules in water require an extended duration to traverse the gaps present within the bio-mechanical interface. As a consequence, this leads to an increase in the leakage time constant ($\tau_{leak,avg}$), a characteristic that remarkably aligns with the requirements of our application.

Among the three suction cup designs, Nitrile rubber cup has the largest average leakage time constant ($\tau_{leak,avg} = 95.29\ (hrs)$ in water) and the smallest average pressure differential change rate ($\dot{\Delta P}_{avg} = 0.0018\ (bar/hr)$ in water). Hybrid cup, on the other hand, although has the highest average initial setup pressure differential ($\Delta P_{int,avg} = 0.298\ (bar)$ in water), but it also has the smallest average leakage time constant ($\tau_{leak,avg} = 42.27\ (hrs)$ in water). However, despite the high leakage rate, this cup still maintains the highest average pressure differential after 24 hours ($\Delta P_{24,avg} \approx 0.165\ (bar)$ in water).

4.3.4 Normal Loading

The pull force (F_P) and the corresponding overall system displacement (D_{sys}, which is the combination of suction cup and substrate displacement along $\hat{\jmath}$ axis) measured in the normal test is presented in Figure 4.7 (A). Among the three, Hybrid cup has the smallest D_{sys} ($\approx$ 12.5 mm), which is about half the case of Nitrile Rubber and Silicone cup ($\approx$ 25.0 mm). As for the ultimate pull force before failure, Nitrile Rubber cup has the largest value ($\approx$ 50 N), followed by Hybrid

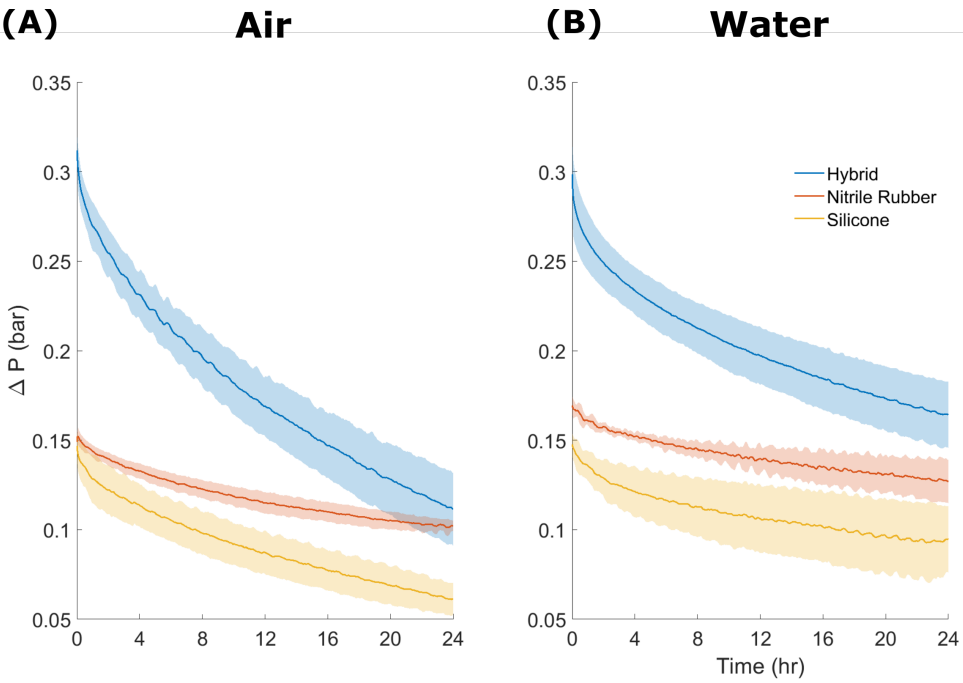

Figure 4.6: Pressure differential ($|\Delta P|$) drop over the 24-hour Leakage test, 3 suction cups (Hybrid, Nitrile Rubber and Silicone) were setup on compliant substrate and test in two mediums: (A) Air and (B) Water.

(≈ 42.5 N) and Silicone cup (≈ 37 N).

The pressure differential (ΔP) fluctuation of the three cups were normalized to $\%$ Trial and showcased in Figure 4.7 (B). While Hybrid cup has the highest initial setup pressure differential ($\Delta P_i = 0.16$ bar) among the three, Nitrile Rubber cup has the largest increment in ΔP and reaches the maximum ultimate pressure differential (0.50 bar) before detachment.

Using the kinetic equation (Eq. 4.2) on vacuum area (A_v) along with the suction cup stiffness (k_{SC}^L), the force composition correlation of $F_P - F_{SC} - F_V$ can be established. The results are presented in Figure 4.7 (C), where F_P is directly measured from the experiment, the F_{SC} is calculated using $k_{SC}^L \Delta H_{SC,o}$, and F_V is the difference between the two. The force composition of the three cups went through a similar pattern. Starting with $F_V = F_{SC}$ at the initial setup state, when suction cup is being compressed by F_V and the spring force F_{SC} counterbalances with it. As F_P being applied to the system and gradually increased, suction cup is slowly returning to its neutral position then switch into elongation, which explains why F_{SC} is at first in the same direction as F_P, gradually decreases to zero, then switch to the opposite direction and increases the magnitude again. The deformation of the cups at 0, 25, 50, 75, 100% Trial are displayed on the top of the force composition sub figures. Comparing the three cups, it is found that Nitrile Rubber cup is the one who generates the largest amount of F_V while the other two are relying more on F_{SC} to reach

force equilibrium with F_P.

4.3.5 Shear Loading

Shear test was conducted to study how well can the three suction cup designs resist drag force (F_D) before sliding. Figure 4.8 (A) and (B) showcase the results of drag force (F_D) and pressure differential (ΔP) normalized to % Trial. The diamond legends in Figure 4.8 (A) indicate the initial sliding of the cups, which were identified by finding the curve slope change from the drag force (F_D) and sliding distance (Figure 4.8 (C)) correlation. The curve segment before sliding is steeper than the one after, which coincides with the physical fact that the static friction coefficient (μ_s) is larger than the kinetic one (μ_k).

Among the three, Nitrile Rubber cup can resists the largest F_D ($\approx 29\ N$) before sliding, follow by Hybrid cup ($\approx 25\ N$), and Silicone one comes last ($\approx 21\ N$). Meanwhile, Nitrile Rubber cup also has the largest increment in ΔP ($\approx 0.3\ bar$) while Hybrid cup has the minimum change in ΔP ($\approx 0.05\ bar$).

To compare the deformation of the suction cup, the states of the initial setup, sliding initiation and the moment of detachment were extracted and displayed in Figure 4.8. There are two noticeable findings. Firstly, Hybrid cup has its' anterior lip edge gradually folding in during the sliding process, while the other two cups have flattened front edge. Second, the level of bell deformation is much subtle on Hybrid cup than the cases of Nitrile Rubber and Silicone cup, which matches the corresponding amount of pressure differential increment.

Lastly, M_{SC} is estimated using Eq 4.7 as a method to quantify suction cup deformation on $\hat{k}$ axis. Since there's no significant change in suction cup height (H_{SC}), the magnitude of M_{SC} is pretty much decided by F_D. Therefore, the $M_{SC} - \%$ Trial curves follows the same trends as $F_D - \%$ Trial curves, where Nitrile Rubber and Silicone cup share the similar patterns and surpass the value of Hybrid cup.

4.4 Discussion

In this chapter, we at first study how a suction cup responds under pure normal ($\hat{\jmath}$ direction) and pure shear ($\hat{\imath}$ direction) loading conditions, with each can be further divided into three stages. Under pure normal loading (F_P only), depends on the current height (H_{SC}) of suction cup with respect to its' neutral height ($H_{SC,o}$) in $\hat{\jmath}$ direction, a suction cup could be either in compression, neutral and elongation state (Figure 4.1 (A) - (C)), which decides the direction of the suction cup restoration force (F_{SC}). As for pure shear loading (F_D only), based on whether the drag force (F_D) overcomes the maximum static friction force ($f_{s,max}$), the suction cup might be static, about

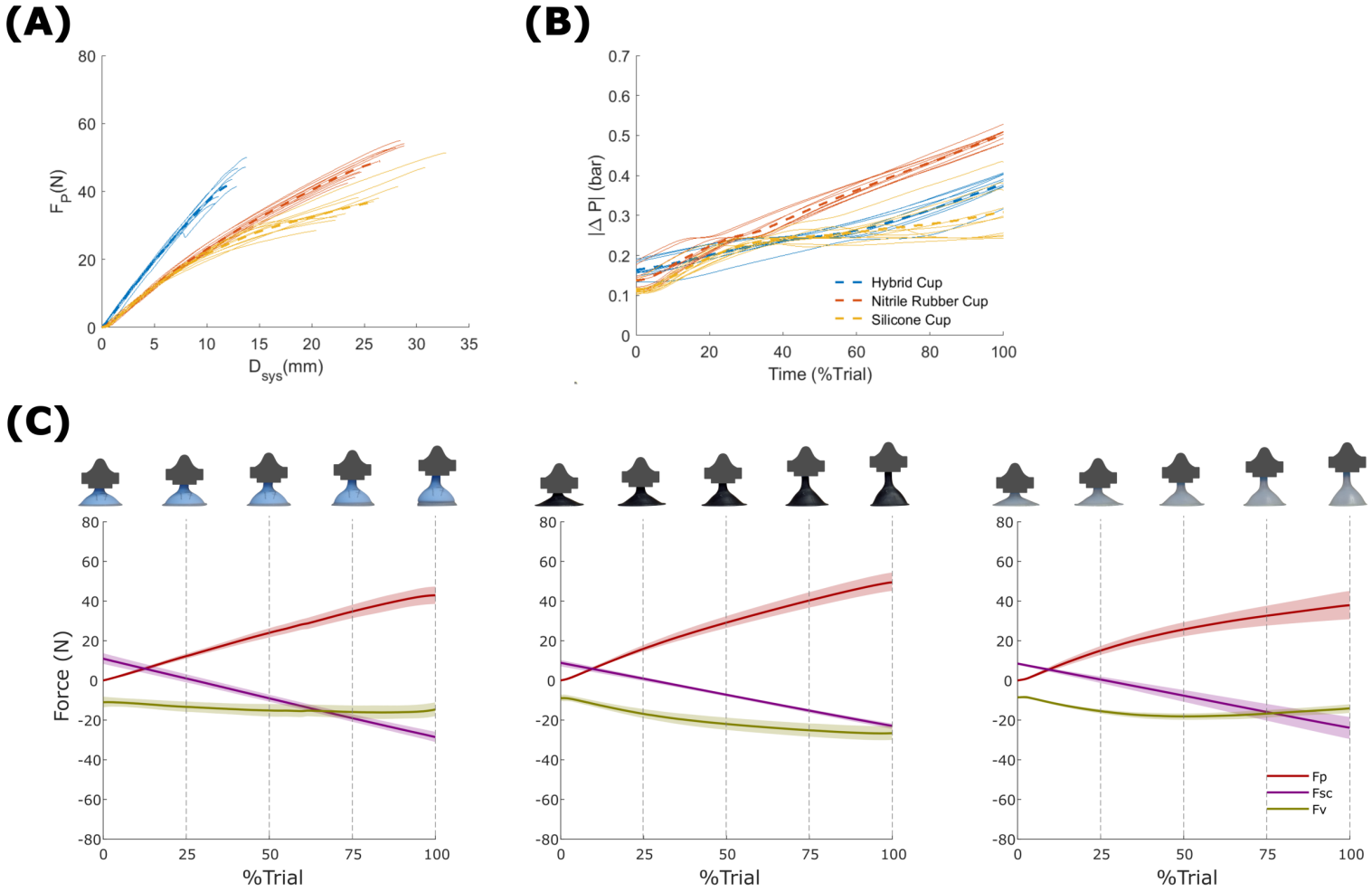

Figure 4.7: Normal test results on compliant (A10) substrates. (A) $D_{sys} - F_P$ correlation; (B)$|\Delta P| - \%$ Trial correlation; (C) Suction cup kinetics of Hybrid (left), Nitrile Rubber (middle), and Silicone cup (right).

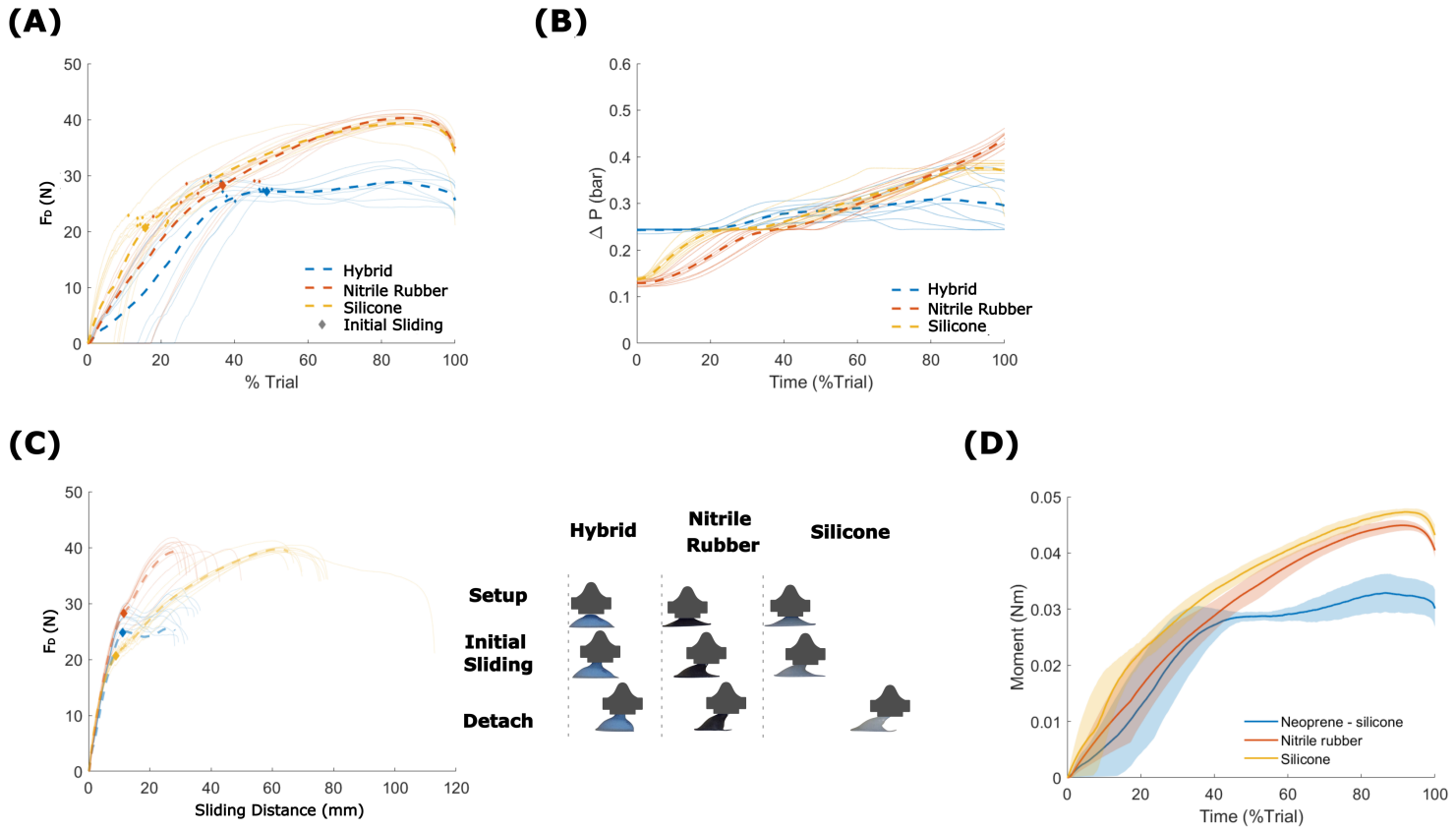

Figure 4.8: Shear test results on compliant (A10) substrates. (A)$F_D - \%$ Trial correlation; (B)$|\Delta P| - \%$ Trial correlation; (C) $D_{slide} - F_D$ correlation with suction cup profiles at setup, initial sliding and detachment (Hybrid (left), Nitrile Rubber (middle), and Silicone cup (right));(D) $M_{SC} - \%$ Trial correlation.

to slide, and sliding (Figure 4.1 (D) - (F)). With the above analysis, we proposed a kinetic model to parameterize the response of a suction cup under a general loading condition for all the three axes as well as from both the systematic (the entire suction cup) and the sectional (A_v and A_c) perspectives (Eq. 4.2 - 4.7).

From the generalized suction cup kinetic model (Eq. 4.2 - 4.7), two key characteristics are found to be specific to each suction cup design. The first is suction cup linear stiffness (k_{SC}^L) which correlates to suction cup spring restoration force ($F_{SC} = k_{SC}^L \Delta H_{SC}$). The second is the area composition ($A_{all} - A_v - A_c$) change during the loading process, which is critical in estimating vacuum force ($F_V = \Delta P A_v$) and environmental force ($F_{env} = p_o A_c$). The insights derived from the suction cup characterization experiments empower us to conduct a more precise analysis of the impact of each individual force component in the suction cup failure tests.

Three sets of experiments were designed to quantify and compare the performances of the three suction cup designs (Hybrid, Nitrile rubber and Silicone) in resisting leakage as well as finding out their normal and shear loading limits before detachment. Upon a comprehensive review of all test results, it becomes evident that suction cup material and geometry exert interconnected influences on parameters that are not entirely separable from one another.

Take Hybrid cup for example, with the highest stiffness (3.5195 N/mm), it can generates the highest initial setup pressure differential (ΔP_i) among the three. However, this feature also makes it difficult to deform the bell when being loaded which prevents the increment of pressure differential (ΔP) to resist larger external loading. Further, the stiffer material also has a larger tendency to restore its' neutral state, which explains the higher pressure differential change rate ($\dot{\Delta P}_{avg}$) measured from the leakage test. On the flip side, Nitrile Rubber cup is the least stiff (1.2697 N/mm) one. It not only has the largest leakage time constant ($\tau_{leakage,avg}$) and the smallest pressure differential change rate ($\dot{\Delta P}_{avg}$) in the leakage test, but also goes through the largest pressure differential (ΔP) increment and reaches the highest loading limits in both normal and shear test.

At this moment, however, it is still difficult to judge which suction cup will be the most suitable choice to use on cetacean bio-logging tags. The reason is that the correlation between these critical suction cup performance criteria (ex. ΔP_i, $\dot{\Delta P}$...) and the level of disturbance they introduce to the animals remains unclear. Further, different cetacean has various integument characteristics which will in turns influence suction cup performances as well.

All in all, this study is groundbreaking in establishing a generalized suction cup kinetic model to depict its' responds to external loading as well as building the connections between suction cup characteristics to the corresponding force components. It also creates the new knowledge on the coupling relationship between suction cup features and certain performance parameters. This is an irreplaceable foundation in setting up the design framework for improving suction cup designed for cetacean bio-logging tag.

For our forthcoming steps, we have outlined a more refined approach. We intend to conduct an intricate analysis and modeling of suction cup stiffness, aiming to disentangle the influences arising from cup material and geometry. In place of a simple 1^{st} order linear regression, we are opting for a polynomial fit that can aptly encapsulate the two-stage deformation pattern exhibited by the suction cup. Moreover, drawing from observations made during field studies, where shear and torque loading stood out as pivotal failure modes, we are devising a novel test setup. This setup will amalgamate shear and torque loading while simultaneously monitoring area distribution ($A_{all} - A_v - A_c$), pressure differential (ΔP), and suction cup morphology. This concerted approach will enable us to pinpoint the critical matrices responsible for triggering suction cup failures.

4.5 Summary

Expanding upon the foundations of the generalized suction cup model and the experimental assessment of cup characteristics and failure modes, the subsequent chapter of my research will delve into harnessing these empirical insights to gain a more profound understanding of cup performance within real-world contexts.

Our current research findings have highlighted disparities between the quantified suction cup performance obtained through laboratory tests and the parameters reconstructed using bio-logging tag data from field studies. Illustrated in Figure 4.9 (A), a schematic depicts a bio-logging tag affixed to cetacean integument. Employing animal acceleration data (a_x) from the bio-logging tag alongside CFD modeling, our research team estimated the drag force (F_D) exerted on the tag at varying animal traveling speeds (u). This drag force (F_D) signifies the resistance that the cups need to withstand during animal deployments.

Upon juxtaposing the outcomes of failure mode tests with preliminary CFD results, it becomes evident that all three types of suction cups should comfortably encompass the performance envelope (Figure 4.9 (B)). This envelope, defined as the loading range encompassing a 95 % probability distribution of animal traveling speeds, fails to align with observations derived from field studies. Intriguingly, tag data reveals instances of tag sliding, rotation, and early detachment, presenting a perplexing contradiction.

The divergence between in-lab testing and field study results can be attributed to multiple factors. Divergent methods for attaching suction cups/tags are a prime example. In the field, on a bumping boat, researchers encounter challenges in deploying tags and have limited control over adjusting suction cups for optimal attachment. Execution issues manifest as lower initial setup pressure differentials (ΔP_i) and potential acceleration of leakage due to seal breaks. Moreover, our in-lab experiments do not consider cetacean body curvature, integument deformation arising from muscle elongation/contraction during locomotion, and the shedding of skin.

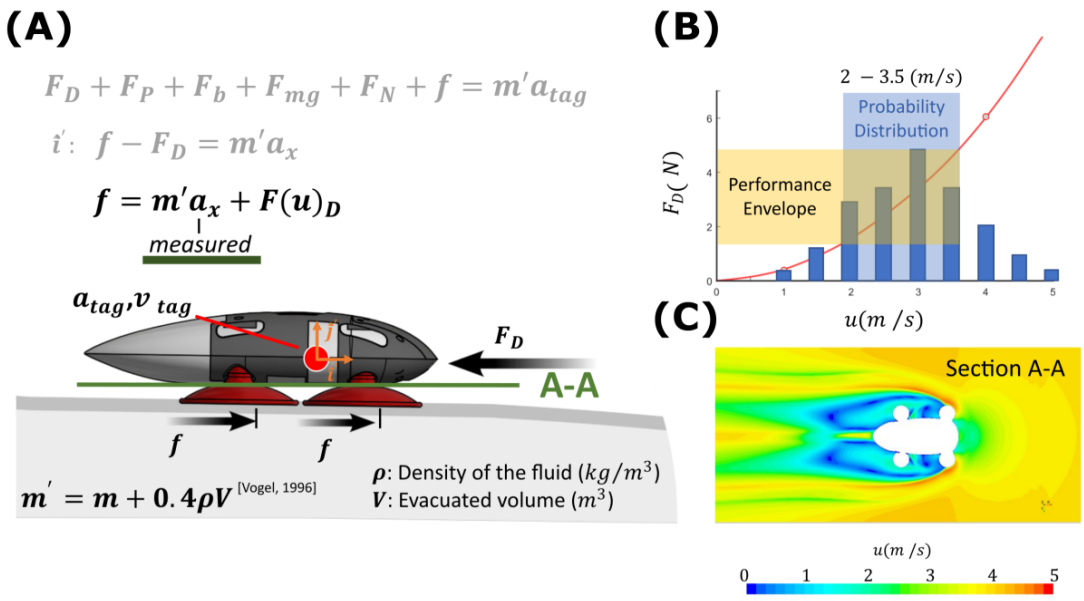

Figure 4.9: Suction cup modeling and performance evaluation. (A) The schematic of a bio-logging tag on cetacean integument; (B) The drag force (F_D) - animal velocity (u) correlation from CFD simulation. (C) The CFD simulation of the A-A plane.

In my forthcoming work, I aim to address these challenges through a two-pronged approach. Firstly, I intend to expand the test protocol to encompass a range of initial setup pressure conditions (ΔP_i) and scrutinize their impact on suction cup performance. Secondly, enhancements to the design and fabrication of the substrate phantom used for testing are paramount. Incorporating multi-layer or distinct material components, and adding surface texture will enable a more faithful emulation of actual cetacean integument. Moreover, improvements to suction cup stiffness (k_{SC}) estimation and area composition ($A_{all} - A_v - A_c$) will be pursued. Through these measures, I aim to closely replicate the scenarios encountered by suction cups in real-world environments, offering a more accurate assessment of their performance.

CHAPTER 5

Suction Cup in Real World

5.1 Problem Statement

Expanding upon the laboratory investigations into the characteristics of suction cups and their load-bearing capacities across three distinct failure modes (Chapter 4), the subsequent phase of our research aims to delve deeper into the interplay of a four-suction cup arrangement when integrated onto a bio-logging tag's body within a real-world context. When affixed to cetacean integument, the tag becomes subject to loading from the surrounding water flow. Consequently, the magnitude and orientation of the resulting hydrodynamic force (F_H) are closely intertwined with the animal's travel speed and the relative alignment between the tag and the animal's heading direction.

With the objective of enhancing tag attachment to yield more reliable animal behavior data, the four-suction cup configuration must extend its capacity to withstand the hydrodynamic force (F_H) under diverse scenarios. To successfully achieve this goal and enhance resilience against heightened hydrodynamic forces (F_H), the initial step necessitates a meticulous quantification of its magnitude across a spectrum of animal locomotion conditions.

However, the direct measurement of hydrodynamic force (F_H) has historically presented a formidable challenge. Furthermore, prior investigations have largely revolved around animal-centric perspectives. Some studies have emphasized the estimation of animals' overall propulsive force, leveraging acceleration information [119, 40]. Others have utilized rudimentary modeling and kinematic measurements from animal subjects [120, 121, 40, 122], or harnessed CFD simulations to gauge drag force [123, 124, 125, 98, 126, 127, 122]. The central focus of these prior endeavors has been to explore how the placement of a tag upon the sleek form of a cetacean body possesses the potential to impact swimming mechanics.

To summarize, a tool that establishes a connection between suction cup performance and its capacity to withstand the hydrodynamic force limit (F_H) is currently absent. Drawing from the suction cup kinetic model introduced in Chapter 4, my intention is to devise a methodology for estimating the hydrodynamic force (F_H) by leveraging the measured parameters of the suction

cup. Specifically, my approach entails:

Task 1:Establish a mapping framework which correlates suction cup kinetics with the hydrodynamic force (F_H).

Task 2: Develop a pressure-logging device to monitor suction cup kinetics and kinematics in real world scenarios.

Task 3: Design and conduct experiments with the pressure-logging device to test different suction cup design under various traveling speed (v).

5.2 Methods

5.2.1 Mapping: From Suction Cup Kinetics to Hydrodynamic Force

The hydrodynamic force (F_H) encompasses force components in both the perpendicular ($\hat{\jmath}$ direction) and parallel ($\hat{\imath}$ direction) with respect to the animal's travel path (Figure 5.1 (A)). For the ensuing analysis, we will focus on the simplified scenario where the animal achieves a steady state, maintaining a constant speed while traveling consistently in a single direction at a uniform depth. While actual suction cup tag failures are prone to occur during transient states, often when animals abruptly alter their travel speed and direction, the examination of steady-state conditions provides a reference point for the average hydrodynamic force (F_H) that suction cup tags must endure. Additionally, this assumption enables us to utilize the generalized suction cup kinetic model introduced in Chapter 4 to formulate the hydrodynamic force expression as follows:

$$\mathbf{F_H} = F_D\,\hat{\imath} + F_P\,\hat{\jmath} \Rightarrow\ F_H = \sqrt{F_D^2 + F_P^2} \tag{5.1}$$

where F_D is as introduced previously:

$$\hat{\imath}\ direction: F_D = F_{||}^r \begin{cases} \leq \mu_s N = f_{s,max}, & \text{static or about to slide} \\ \geq \mu_k N = f_k, & \text{sliding} \end{cases} \tag{5.2}$$

From the kinetic analysis on A_c, N can be expressed as:

$$\hat{\jmath}\ direction: N = F_{env} + F_{SC} + F_{\perp}^r \tag{5.3}$$

with $F_{\perp}^r (= \Sigma f_{\perp}^r)$ being the sum of friction force on $\hat{\jmath}$ axis. Friction force (F^r) acts along the contact surface. Hence, for the case of rigid substrate, $F_{\perp}^r = 0$, because the friction force act

merely horizontally, such that there's no component in $\hat{\jmath}$ axis. Therefore, N can be simplified as:

$$\hat{\jmath}\ direction : N = F_{env} + F_{SC} \tag{5.4}$$

Next, we look at the kinetic analysis on A_v, where F_P can be expressed as:

$$\hat{\jmath}\ direction : F_P = F_V - F_{SC} \tag{5.5}$$

here, F_{SC} is the spring restoration force coming from suction cup deformation.

Using the aforementioned equations, we can now establish a correlation that connects measurable suction cup parameters to the force components required for estimating hydrodynamic forces (F_H). Among the various suction cup parameters, the pressure differential (ΔP) proves to be the most practical and straightforward to monitor. Unlike forces such as F_P and F_D, which necessitate load cells for measurement, or deformations like ΔH_{SC} and area compositions (A_v and A_c), which rely on camera footage data, pressure transducers offer a compact form factor that can be seamlessly integrated into the current electrical module of bio-logging tags. With pressure differential (ΔP) identified as the targeted suction cup parameter for measurement, the subsequent step entails establishing the correlation between ΔP and the corresponding F_D and F_P.

Commencing with F_D, its estimation necessitates a sequential progression. Initially, the determination of N (Eq. 5.2) is required, which, in turn, hinges upon the availability of data for F_{env} and F_{SC} (Eq. 5.4). Subsequently, since $F_{env} = p_o A_c$, establishing the relationship between ΔP and A_c becomes imperative. Turning to F_{SC} ($= k_{SC}^L \Delta H_{SC}$), its computation mandates knowledge of the suction cup $\hat{\jmath}$-axis deformation (ΔH_{SC}), thereby ruling out a direct mapping from ΔP. Instead, F_{SC} can be expounded as $F_v - F_P$ predicated on the force equilibrium relation pertaining to A_v (Eq. 5.5). Here, $F_V = \Delta P A_v$, amenable to calculation through the established mapping between ΔP and A_v. Concerning F_P, informed by our generalized suction cup kinetic model and preceding standard tests, it is revealed to be a variable that fluctuates in tandem with alterations in pressure differential ($|\Delta P|_{rel} = \Delta P_t - \Delta P_{int}$) concerning the initial setup pressure differential (ΔP_{int}). This affirms that F_P can be correlated with the value of $|\Delta P| rel$. Armed with the approaches to derive F_V and F_P through mapping, the computation of F_{SC} ensues accordingly (Eq. 5.5), thereby supplying the requisite data for estimating N (Eq. 5.4).

In a nutshell, the following three mappings are required in order to estimate F_H:

1: $|\Delta P|_{rel}$ - F_P

2: $|\Delta P|$ - A_v

3: $|\Delta P|$ - A_c

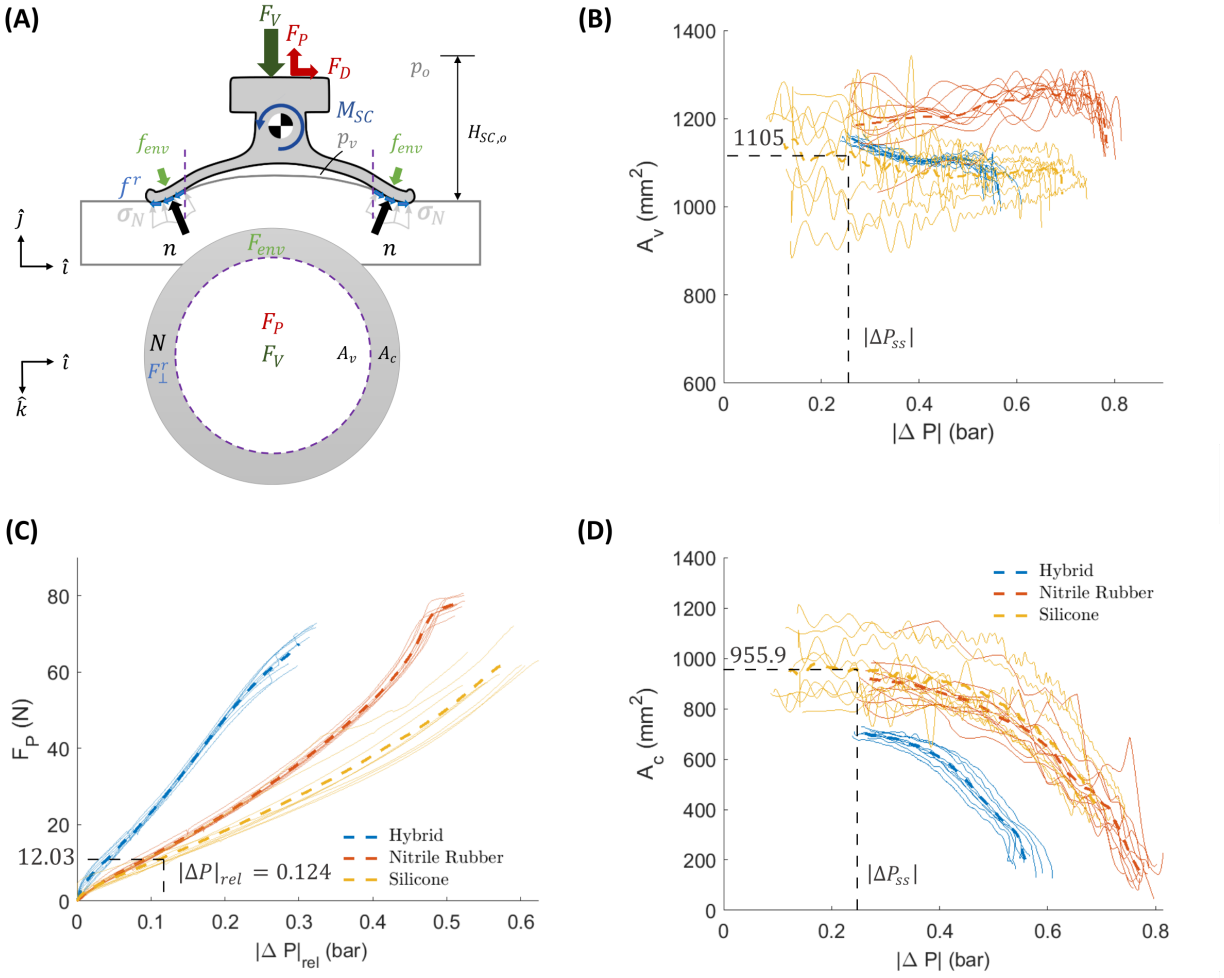

Figure 5.1: (A) Suction cup kinetics under general loading condition; (B) Correlation between pressure differential ($|\Delta P|$) and vacuum area (A_v), which can be used to estimate vacuum force as $F_V = |\Delta P| A_v$; (C) Mapping from relative pressure differential ($|\Delta P|_{rel}$) to pulling force (F_P), $|\Delta P|_{rel}$ is the increment of pressure differential ($|\Delta P|$) with respect to the initial setup value ($|\Delta P|_i$); (D) Correlation between pressure differential ($|\Delta P|$) and contact area (A_v), which can be used to estimate environmental force as $F_{env} = p_o A_c$

Firstly, utilizing the parameters collect from the suction cup characterization experiment (Figure 4.2 (B)), the area composition data ($A_{all} - A_v - A_c$) can be synchronized with the corresponding pressure differential ($|\Delta P|$) measurement via % Trial, and the $|\Delta P|$ - A_v (Figure 5.1 (B)) and $|\Delta P|$ - A_c (Figure 5.1 (D)) mapping can be obtained. Take Silicone cup for example, when it reaches the steady state pressure differential ($|\Delta P_{ss}|$) as 0.216 (bar), the corresponding A_v and A_c are 1105.0 mm^2 and 955.9 mm^2, respectively. With these information, the F_V ($= |\Delta P_{ss}| A_v$) and F_{env} ($= p_o A_c$) at the moment can be calculated accordingly.

Second, in order to build the mapping from $|\Delta P|_{rel}$ to F_P, we leverage the data collected from the normal test experiment (Figure 4.3 (B)). $|\Delta P|_{rel}$ is calculated by subtracting the initial setup pressure differential ($|\Delta P|_{int}$) of each trial from the $|\Delta P|$ measurement, than normalized to % Trial in order to synchronized with F_P. The resultant relationship is presented in Figure 5.1 (C). Take Silicone cup as example again, when it reaches the steady state pressure differential ($|\Delta P_{ss}|$) as 0.216 (bar), the corresponding $|\Delta P|_{rel}$ is 0.124 bar, which allows us to know the value of F_P at the moment is 12.03 (N).

5.2.2 Pressure-logging Tag

With the mapping approach ready, we now need a device which enables pressure differential ($|\Delta P|$) measurement while the suction cups are on board of a bio-logging tag. So as to evaluate the magnitude and direction of the hydrodynamic force (F_H) that the suction cups are experiencing. To achieve the goal, we make use of the existing M-tag architecture as foundation to develop the pressure-logging tag, a device shares the same body profile as a M-tag and with embedded pressure sensors to monitor ΔP of each of the four suction cups.

For the electronic module of the pressure tag, we maintained the same footprint as the one used on M-tag to eliminate the need for great modification on the tag body structure. Figure 5.2 showcases the schematic of the electrical module. The module units include the charging circuit for switching power source selection between battery and USB port; the voltage regulator which pumps up the voltage input from the charging circuit to power 5V-logic microcontroller; the micorocontroller and I2C communicator which regulate the data sensing and recording among multiple I2C sensors; data storage module and finally the sensor module.

We then designed a 34 mm x 60 mm printed circuit board (PCB) embedding essential components based on the schematic. On the back of the PCB (Figure 5.3 (A)(right)), four pressure transducers (MS5837-30BA, TE Connectivity, Schaffhausen, Switzerland) sit at the four corners to match the location of suction cups to reduce the length of the connecting tubing in between. The measurements of absolute pressure (P_{abs}) from 4 cups were converted into I2C signals (Inter-Integrated Circuit) and sent to the main processor board (Arduino Nano Every, Adafruit Industries,

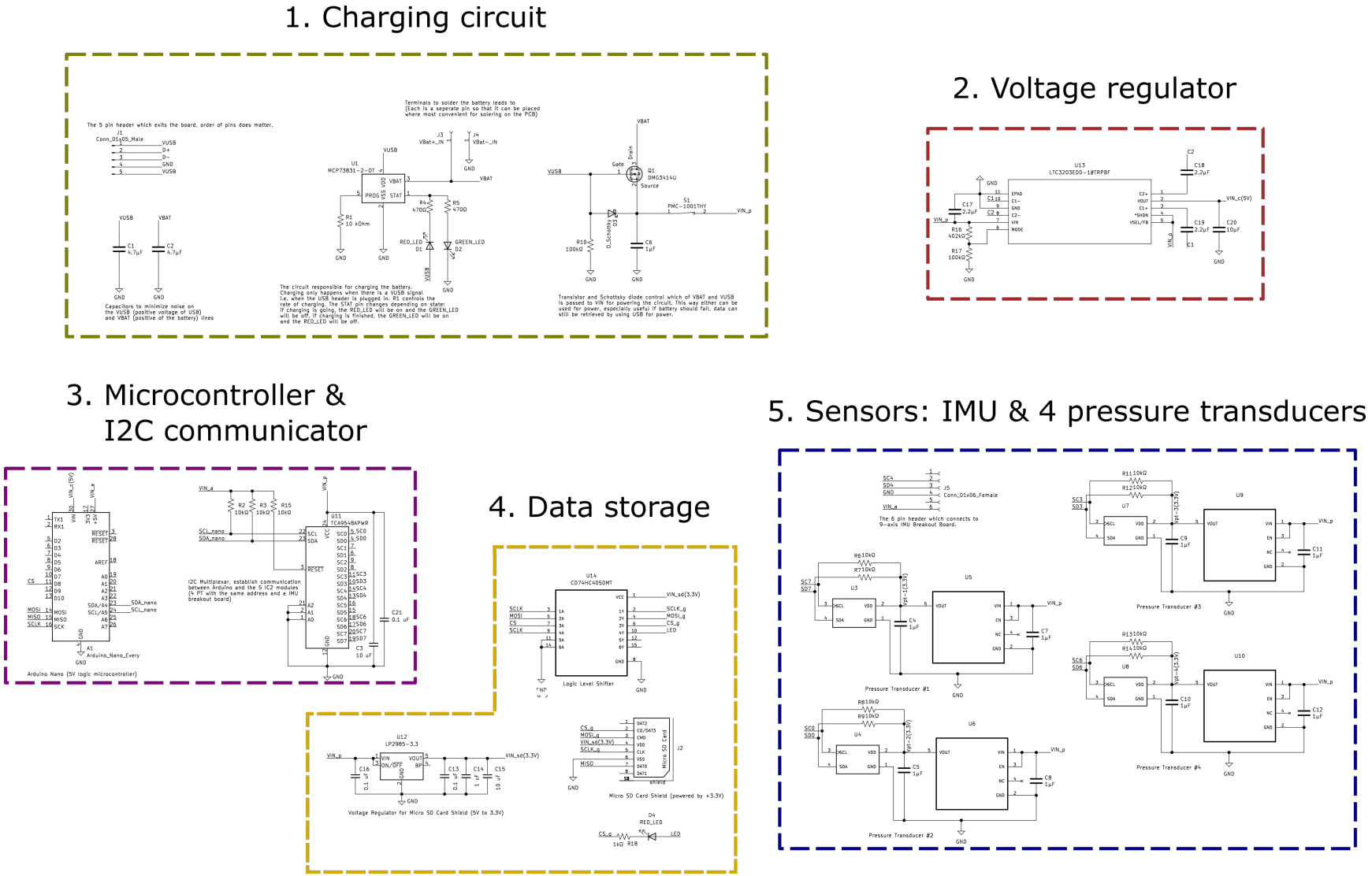

Figure 5.2: Pressure tag schematic, the printed circuit board (PCB) contains the following modules:(1) charging circuit, (2) voltage regulator, (3) microcontroller and I2C communicator, (4) data storage and (5) sensors.

Italy) on the front of the PCB (Figure 5.3 (A)(left)) through a I2C multiplexer (TCA9548A, Texas Instruments, USA), which helps regulate signals from different sensors. In addition to the pressure transducers, an inertial measurement unit (IMU. BNO055, Adafruit Industries, New York, USA) was also incorporated on the PCB to measure the orientation, acceleration and rotation of the tag. Once the microcontroller received the measurements, the data will be logged onto a micro SD card. The entire circuit was powered by a rechargeable 3.7-V lithium battery (Li-Polymer 803860, PKCELLK, Shenzhen, China).

After soldering and assembling the chips, the PCB was then stacked with the battery and encased in the container previous developed for M-tag and sealed with Epoxy to create a waterproof electronic module, as shown in Figure 5.3 (B) (left). The electronic module has 4 tubing sticking out from the 4 pressure transducers. A set of 4 suction cups can be anchored on the tag body like the one presented in Figure 5.3 (B) (right). There are 4 groves on the tag body to position the tubing which connects each pressure transducer to the corresponding suction cup. The top view and the side view of the fully assembled pressure tag is showcased in Figure 5.3 (C).

5.2.3 Tow Tank Experimental Setup

To investigate the magnitude and direction of the hydrodynamic force (F_H) the suction cups experience under various animal locomotion, we tested the pressure-logging tag in Aaron Friedman Marine Hydrodynamics Laboratory at University of Michigan. The lab is equipped with a physical model basin (tow tank) of 109.7 m long, 6.7 m wide, and 3.2 m deep. The tow tank has a carriage sitting on top of the track which can travel at the speed ranged from 0.08 to 6.1 m/s.

For our experimental setup, an aluminum plate is machined into foil profile and attached to the fixture at the bottom of the carriage (Figure 5.4 (A)). The aluminum plate serves as the substrate for the pressure tags to stick on and carry them to travel along with the carriage. Hybrid and Silicone cup were tested with the orientation of 0, +45, 90, -45, 180 degrees at the speed of 1, 2, 3, and 4 m/s, these speed were chosen based on the field study tag data [98]. Figure 5.4 (A) displays the side view of the carriage and the orientations tested, with the tag sitting at 0.7 m below water during the trials. The carriage speed profiles are shown in Figure 5.4 (B).

The entire experiment contains 6 sessions, each one tests the same tag orientation for 8 trials with the carriage speed in the order of [1, 2, 3, 4, 4, 3, 2, 1] (m/s). Before the 1^{st} and the 4^{th} session, the tags were flipped upside-down and back five times with the intervals of 5 seconds and the time of actions was recorded to synchronize with the carriage system data (travel speed) in post-processing. Three cameras (HERO5, GoPro, California, USA) were mounted on the carriage to monitor the tags and suction cup conditions during the trials.

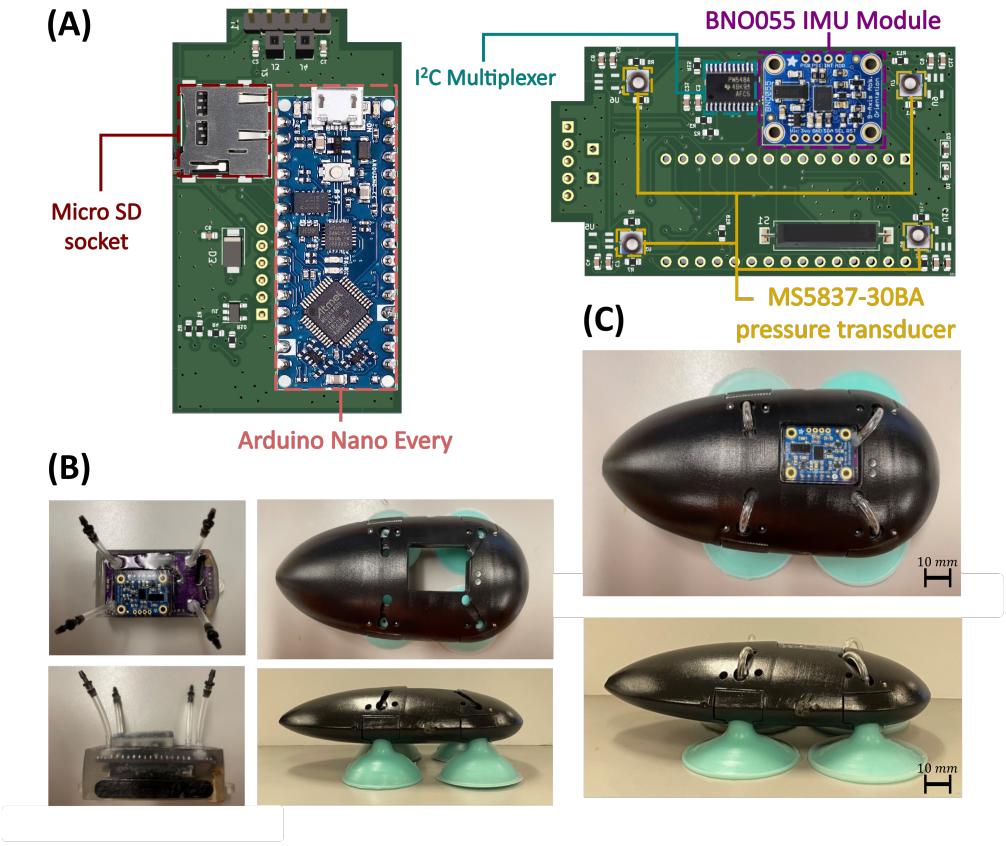

Figure 5.3: Pressure tag: (A) PCB and major components: microprocessor (Arduino Nano Every), 4 pressure transducers (MS5837-30BA), IMU (BNO055), processor-sensor communicator (I2C multiplexer) and data collection (micro-SD card); (B) Epoxied electronic module (left) and tag body (right) (C) Assembled pressure tag.

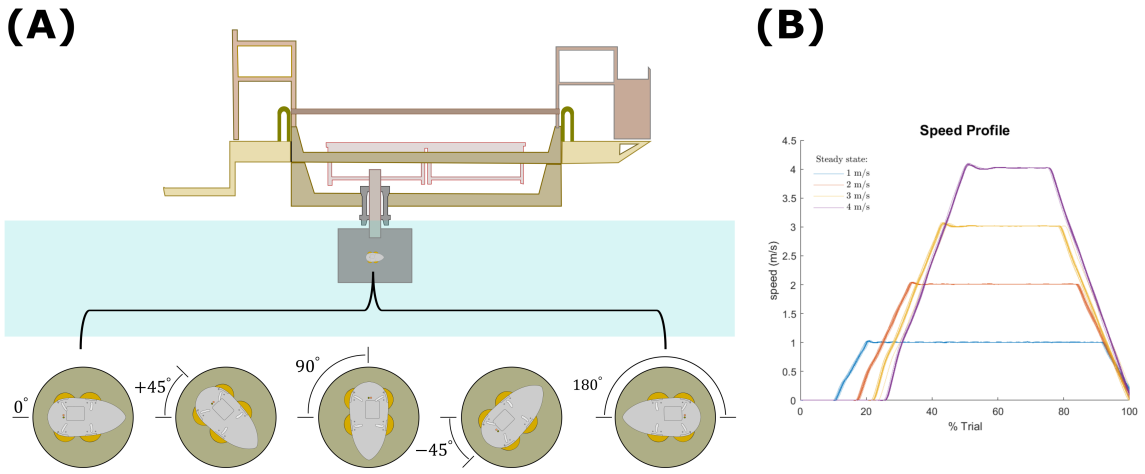

Figure 5.4: Pressure tag testing conditions: The tags were attached to the aluminum plate which connected to the bottom of the cart. Tests include: (A) 5 tag orientations (angle from the tag front center line to the direction of travel) and (B) 4 cart speeds.

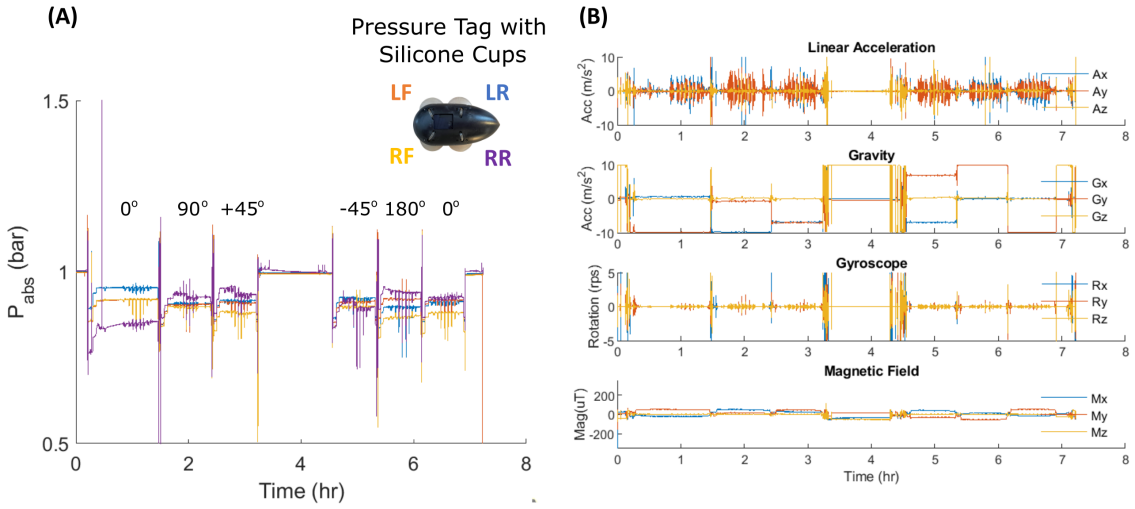

Figure 5.5: Pressure tag raw data from silicone cups: (A) Absolute pressure (P_{abs} (bar)) measurement from 4 pressure transducers onboard (LF, RF, LR, RR represent the cup positions with respect to the tag, which are left front, right front, left rear, right rear). The test consists of 6 sessions, with the corresponding tag orientation noted in the figure. There are 8 trials in each session in the order of 1, 2, 3, 4, 4, 3, 2,1 (m/s); (B) IMU measurements: linear acceleration, gravity, rotation, and magnetic field (From top to bottom). Before the experiment, the tag were flipped in z-direction with a specific pattern to create time stamps in gravity reading (G_Z), for the purpose of aligning data from tow tank system.

5.2.4 Data Analysis

To download the recorded data from the pressure tag, we used a Python script to communicate with micro SD card via serial port through microcontroller. Afterward, the data were imported into MATLAB (MathWorks,Natick, USA) for further processing. Figure 5.5 displays the raw data collected from pressure tag with Silicone cups. The $|P_{abs}|$ were collected by the 4 pressure transducers on board (Figure 5.5 (A)), the data lines are color-coded with each represents the corresponding suction cup on the pressure logging tag legend. Figure 5.5 (B) showcased the data collected by IMU, including linear acceleration, gravity, rotational speed, and magnetic field. Using the timestamps we created on z-axis acceleration (gravity), we can now synchronize pressure-logging tag data with the carriage traveling speed from the tow tank system.

The goal of data processing is to find the steady-state pressure differential ($|\Delta P_{ss}|$) and the corresponding relative pressure differential ($|\Delta P|_{rel} = \Delta P_t - \Delta P_{int}$) of each cup under each tag orientation and traveling speed. Then we can follow the mapping approach introduced in 5.2 to estimate F_P and F_D, and calculate F_H accordingly.

The data processing procedure is broken down into three steps and presented in Figure 5.6. The

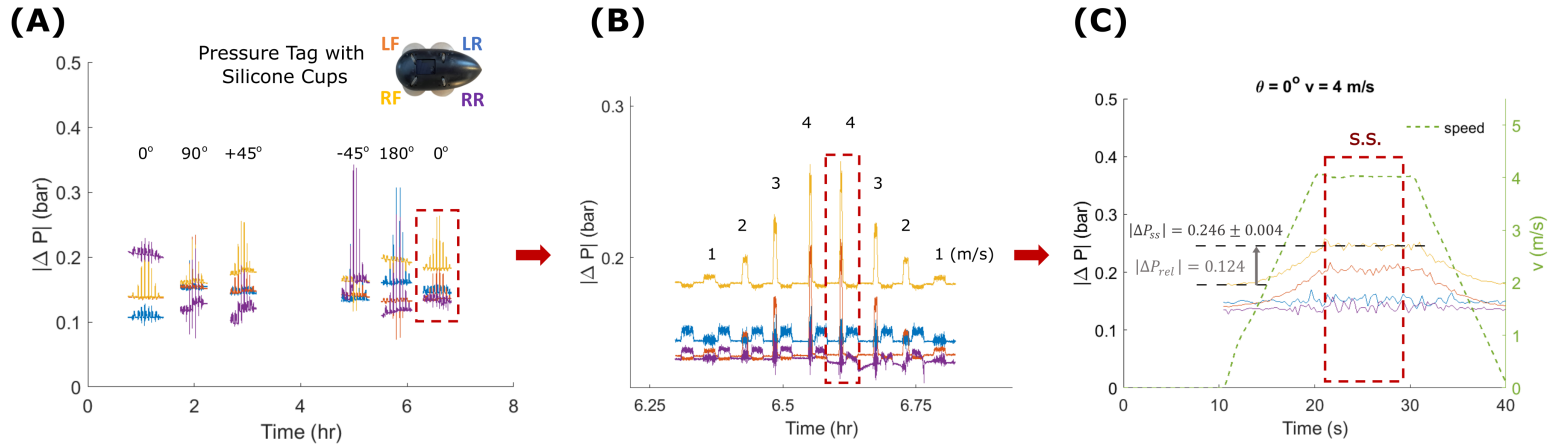

Figure 5.6: Data analysis procedure: (A) Pressure differential ($|\Delta P|$) of each suction cup with respect to the surrounding environment, with the redundant data in between sessions removed; (B) Zoom-in view of the 0^o session, the numbers denote the cart speed in each trial; (C) Data alignment between the tag measurement ($|\Delta P|$) and the tow tank system (cart speed), the dashed box enclosed the steady state section of the representative trial ($\theta = 0^o$, $v = 4\,m/s$), and, for the RF suction cup, the steady state pressure differential ($|\Delta P_{ss}|$) as well as the relative pressure differential ($|\Delta P_{rel}|$) of each cup can be calculated accordingly.

first step is to calculate pressure differential ($|\Delta P|$) from absolute pressure (P_{abs}). Based on the relationship between carriage travel speed with time, we were able to identify the pressure data prior to each test session. We then take the average of these data as the environment pressure (P_{env}). Figure 5.6 (A) showcases the resultant pressure differential ($|\Delta P|$) after subtracting P_{env} and removing redundant data between sessions. Second, we zoom in to one test session where it contains 8 trials and isolate the data from one trial for the next step. Here we use the 5^{th} trial ($v = 4\ m/s$) in $\theta = 0^o$ session as example (Figure 5.6 (B)). In the third step, we align the pressure differential data ($|\Delta P|$) with carriage travel speed. The steady state of each trial is identified as the carriage reaches the target travel speed, and the pressure differential data fall within the time span is used for calculating $|\Delta P_{ss}|$ and $|P_{rel}|$. In Figure 5.6 (C), the steady state is enclosed by a red dashed box, with $|\Delta P_{ss}|$ and $|P_{rel}|$ of the RF suction cup being 0.216 bar and 0.124 bar, respectively.

Once we have the values of $|\Delta P_{ss}|$ and $|\Delta P_{rel}|$, we can now leverage the mapping correlation introduced in 5.2 to calculate the corresponding forces. Continue with the same example, for Silicone cup, the A_v and A_c are found to be $1105\ mm^2$ and $955.9\ mm^2$ with $|\Delta P_{ss}| = 0.216$ bar and F_P is 12.03 N with $|\Delta P_{rel}|$ equals to 0.124 bar. Thereby, the vacuum force ($F_V = \Delta P A_v = 23.87$ N), and environment force ($F_{env} = p_o A_c = 103.24$ N) could be calculated accordingly.

Next, we rewrite normal force (N) as follow:

$$\hat{\jmath}\ direction : N = F_{env} + F_{SC} = F_{env} + (F_V - F_P) \tag{5.6}$$

which equals to 115.08 N for this specific case. Having the value of N, we can now estimate the upper bound of the drag force ($F_{D,max}$) this RF Silicone suction cup could resist under this condition before sliding starts. With Eq. 5.2 and the estimated static friction coefficient ($\mu \approx 0.25$ between rubber and metal), $F_{D,max} \approx 28.77$ N.

5.3 Results

Adopting the analysis procedure established in Session 5.2.4, we processed the data collected by pressure-logging tags with Silicone and Hybrid cups under each individual test condition.

5.3.1 Hydrodynamic Force Estimation with Pull Force and Drag Force

The average pull force (F_P) sustained by each suction cup along with the corresponding standard deviation is showcased in Figure 5.7. Take Hybrid cup as example, with orientation equals to 0^o, LF and RF cups contribute about resisting 79-83 % of the total pull force ($F_{P,total}$). As travel speed increases from 1 m/s to 4 m/s, the total pull force ($F_{P,total}$) increases from 3.88 N to 39.51 N.

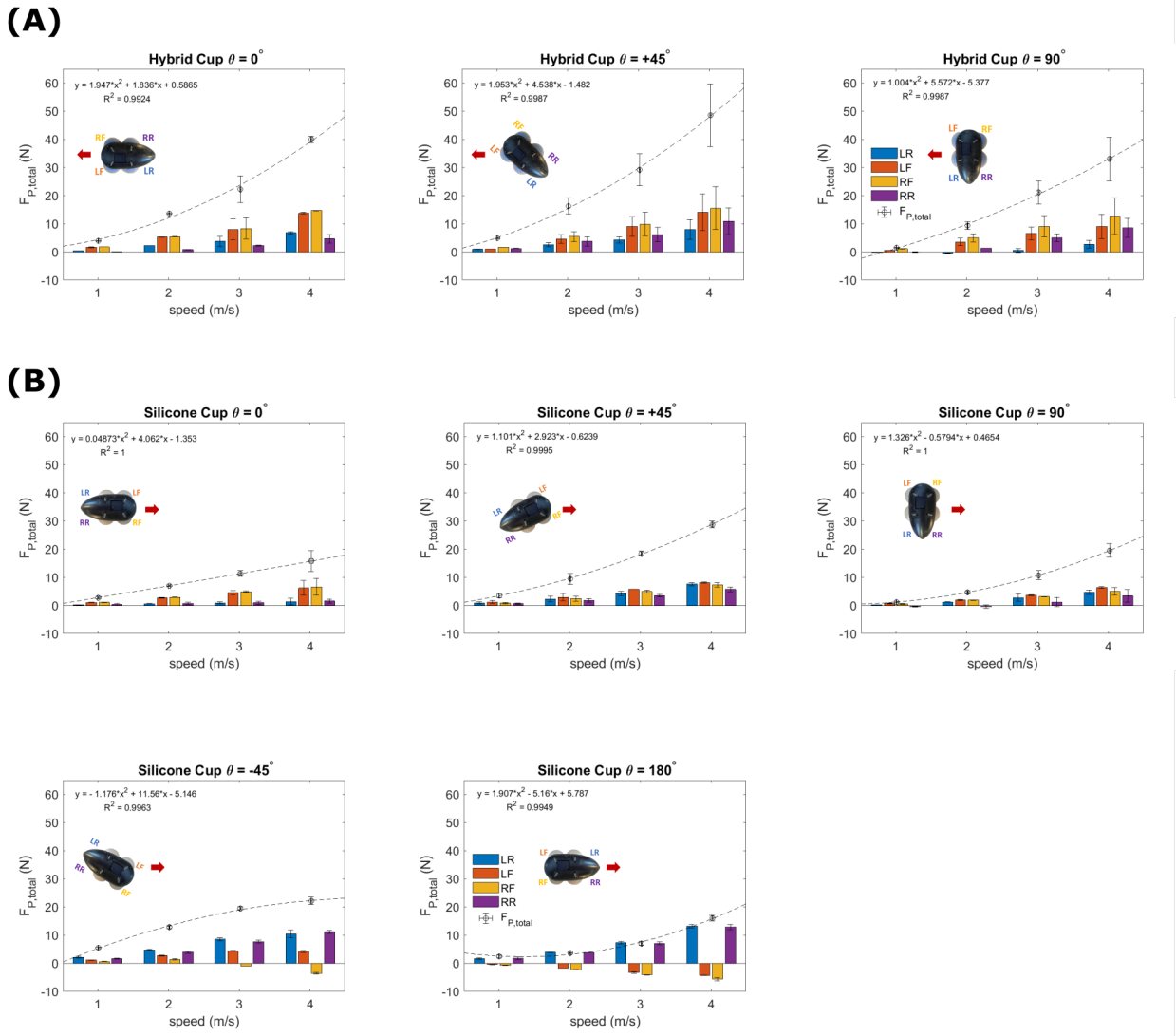

Figure 5.7: $F_{P,total}$ - θ - v correlation: Each subplot contains the average and standard deviation of F_P sustained by individual cup at [1, 2, 3, 4] (m/s) under each specific orientation. (A) Hybrid cups at [0^o, $+45^o$, 90^o]; (B) Silicone cups at [0^o, $+45^o$, 90^o, -45^o, 180^o]. The sum of the pull force from 4 cups ($F_{P,total}$) are also presented and fitted with 2^{nd}-order linear regression. The corresponding tag orientation is illustrated as legend, with arrow indicating the direction of travel.

Table 5.1: Upper Bound of Drag Force ($F_{D,max}$): Silicone and Hybrid cups with $\theta = 0^o$ orientation, where LR, LF, RF, RR represent suction cup positions as shown in Figure 5.7 legends.

Silicone cup	$\theta = 0^o$			
$v\ (m/s)$	1	2	3	4
LR	29.280 ± 0.024	29.17 ± 0.020	29.06 ± 0.105	28.905 ± 0.281
LF	28.993 ± 0.017	29.293 ± 0.042	29.952 ± 0.181	30.048 ± 0.647
RF	30.378 ± 0.025	30.377 ± 0.029	30.185 ± 0.068	30.219 ± 0.748
RR	31.025 ± 0.091	30.932 ± 0.085	30.892 ± 0.144	30.760 ± 0.186
Hybrid cup	$\theta = 0^o$			
$v\ (m/s)$	1	2	3	4
LR	26.737 ± 0.006	26.260 ± 0.010	25.853 ± 0.439	25.017 ± 0.103
LF	26.167 ± 0.025	25.348 ± 0.015	24.976 ± 0.934	23.891 ± 0.074
RF	26.259 ± 0.001	25.292 ± 0.022	24.572 ± 0.937	23.398 ± 0.017
RR	26.877 ± 0.015	26.712 ± 0.022	26.388 ± 0.046	25.864 ± 0.354

Similar trends are found in the case of Silicone cup as well, at 0^o, the two suction cups (LR and RF) which position at the anterior of the tag account for about 80 % of $F_{P,total}$, with the magnitude increases with travel speed, from 2.78 N at 1 m/s to 15.75 N at 4m/s. Among all the orientation conditions, both cups sustain the highest $F_{P,total}$ at $\theta = +45^o$, with 48.15 N and 28.82 N at 4 m/s for Hybrid and Silicone cup, respectively.

For Silicone cup, we did tests with two additional orientation, $\theta = [-45^o\ 180^o]$. For the case of -45^o, the $F_{P,total}$ increment with travel speed is smaller due to the fact that one of the cup (RF) contributes little to negative amount. As for the case of 180^o, both LF and RF contribute negative amounts to $F_{P,total}$ acroos all travel speeds.

The upper bound of the drag force ($F_{D,max}$) for each suction cup can be evaluated using the Coulomb friction model (Eq. 5.5). In Table 5.1, the cases of Hybrid and Silicone cup under 0^o orientation are presented. To find $F_{D,max}$ under other test conditions, please refer to Appendix A. Based on Table 5.1, the $F_{D,max}$ for Silicone cup falls within the range of 29-31 N, and 23.5-27 N for Hybrid cup. The values of $F_{D,max}$ are pretty constant across all the travel speeds and orientations.

With the information of pull force, F_P, and the upper bound of drag force, $F_{D,max}$, we can now pinpoint the range of both the magnitude and direction (Eq. 5.1) of the hydrodynamic force (F_H) that a set of 4 suction cups experience under specific tag orientation and travel speed.

5.4 Discussion

5.4.1 Traveling Speed and Tag Orientation

Comparing the values of pull force (F_P) among all test conditions from a comprehensively perspective, it is found that the magnitude increases along with travel speed under all tag orientations. On the other hand, when we look at the same travel speed under different tag orientation, $+45^o$ is the case has the highest F_P. As for the drag force (F_D), from the upper bound we estimated, there's no evident tendency regarding both the travel speed and tag orientation. Based on the findings above, we can assume that the value of the ultimate hydrodynamic force ($F_{H,u} = \sqrt{F_{D,max}^2 + F_P^2}$) increases as the corresponding pull force (F_P).

5.4.2 Hybrid Cup vs. Silicone Cup

Taking a closer look at the analysis result from the Hybrid and Silicone cup, it is noticed that the Hybrid one sustains higher F_P than the Silicone one. On the other hand, for the case of $F_{D,max}$, Silicone cup has a slightly higher value than Hybrid one consistently across all the test conditions.

To better understand the causes for the differences, we firstly checked the $|\Delta P_{rel}|$, and found the values between the two cups are about 30 % apart. Take $\theta = 0^o$ and $v = 4$ (m/s) for example, for Hybrid cups in RF and LF positions, $|\Delta P_{rel}| \approx 0.05$ bar, as for the case of Silicone cups, the number is about 0.07 bar. We reckoned that since Silicone cup is more compliant (1.3153 N/mm) than Hybrid one (3.5195 N/mm) (Figure 4.4), its' bell deformed more under the same flow which resulted in larger $|\Delta P_{rel}|$. Nevertheless, since the $|\Delta P_{rel}| - F_P$ mapping correlation is steeper for Hybrid cup (Figure 5.1 (C)), it still resulted in a higher F_P.

On the other hand, as $F_{D,max}$ estimation mainly depends on $N = p_o A_c$, it is pretty much decided by the size of A_c. Referring to the $|\Delta P| - A_c$ mapping on Figure 5.1 (D), we can find that there's roughly a constant 250 mm^2 difference between Silicone and Hybrid cup, which explained why the former has a higher $F_{D,max}$.

We don't really know for sure at this moment which suction cup suits better for what specific animals. There's a lot more factors that need to be taken into account. Ideally, we would prefer a design that can sustain higher F_H with minimal $|\Delta P_{rel|}$. Because a larger increment in $|\Delta P_{rel|}$ might have a higher chance of disturbing animals' behaviors, further, the elongation of suction cups will results in relative motions between the tag and the animals so as to influence the reliability of the collected data, either case is not desirable.

5.5 Summary

In this chapter, based on the generalized suction cup kinetic model and the data collected from the failure mode tests, we established the mapping from measurable suction cup parameters ($|\Delta P|$ and $|\Delta P_{rel}|$) to the critical force components (F_P and $F_{D,max}$) required to estimate the hydrodynamic force (F_H).

A new device, pressure-logging tag, was developed following the architecture of M-tag to realized suction cup $|\Delta P|$ monitoring under the same setup as the ones embedded in bio-logging tag. The pilot experiments conducted in a tow tank validate the feasibility of the pressure tag. $F_{H,max}$ under various test conditions, for both tag orientation (θ) and travel speed (v), were evaluated and compared between Hybrid and Silicone cups.

There are two major limitations in our approach. First is not able to estimate the exact F_D with the Coulomb friction model (Eq. 5.5). Moving forward, we will include CFD simulation to help narrow down the potential range of F_D so as to have a more precise idea of F_H under each loading conditions, and to have a clear vision regarding how F_D correlates to different tag orientations and travel speed as well. Figure 5.8 presents a preliminary CFD simulation model built by our cooperator. From the lift - speed curve on the bottom right, the F_P values CFD estimated match well with the ones we derived for the case of Silicone cup using the mapping approach. This is a promising news that implies the setup of the model coincides well with the real scenario, and therefore the simulation results of F_D (Figure 5.8, top right) is very likely to reflect the real condition and can serve as reference.

Second is to improve the phantom design. We tested pressure tag on aluminum plate in the tow tank experiment, which is nothing alike cetacean integument. As we already proved that substrate attributes (ex. compliance and skin shedding) have tremendous impacts on suction cup performances. This necesstes the need to ameliorate phantom designs to include features better mimicing ceteacean integument for the furtue tests before we are confident to deploy the pressure tag on live animals.

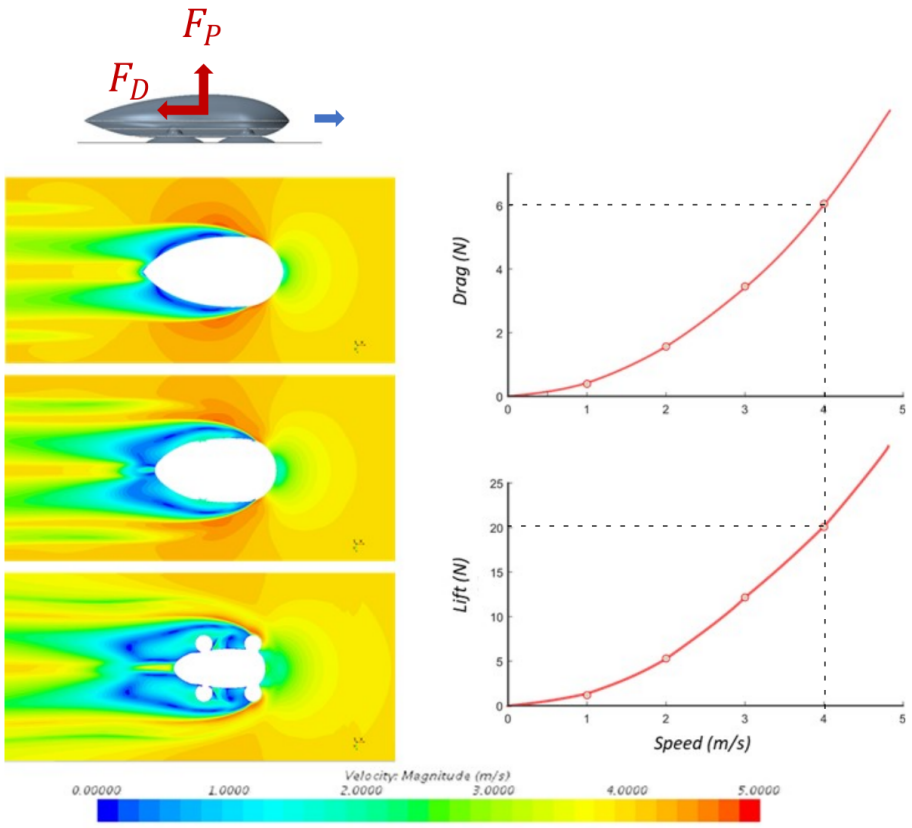

Figure 5.8: Preliminary CFD modeling of bio-logging tag: The illustration on top left showcases the physical setup of the sysem, with blue arrow indication the direction of travel. The simulation results for $Drag - speed$ and $Lift - speed$ are show on the right, with the lift force matches well with the F_P of Silicone cup derived using our mapping approach.

CHAPTER 6

Conclusion

6.1 Synthesis of Research Contributions and Broader Impacts

Bio-mechanical interface where a biological system being contact with a mechanical apparatus can be found everywhere in the daily life. The force interaction and impedance mismatch between the two parties are crucial factors that impact the comfort of the biological host and the effectiveness of the mechanical device. The focus of my research is on one specific example of the diverse bio-mechanical interfaces: the use of suction cups to secure bio-logging tags onto cetacean integument.

Spanning over thousands of years, researchers have faced significant challenges in understanding and improving device designs for biological-mechanical coupled systems. The most iconic example is the design of orthotics and prosthetics, which can be traced back to ancient Egypt [27] (Figure 6.1). Compared to modern medical practice, despite advancements in the orthotics and prosthetics fabrication process, the design principle and procedure stay pretty much unchanged, and the problem of fitting on the contact surface remains a persistent issue to this day, with the only solution being the regular clinical visits for adjustment.

The primary contribution of my work was to generate novel insights into a systematic and comprehensive approach for addressing bio-mechanical interface design problems. My research approach comprised five key components:

Step 1: Developing a new *in-vivo* characterization instrument for the biological system.

Step 2: Establishing a kinetic model of the suction cup - cetacean integument coupled system.

Step 3: Identifying key design parameters which correlate with suction cup performance.

Step 4: Creating a new tool to monitor suction cup performance under real-world conditions.

Step 5: Proposing a design framework to guide and improve suction cup performance in a systematic manner.

Figure 6.1: The 3000-year-old ancient Egyptian prosthesis recovered from a burial chamber in the Sheikh ´Abd el-Qurna necropolis (west of Luxor, Egypt) was crafted from leather and wood, which can be adjusted to precisely fit its wearer's foot [27].

These steps can be applied to study other bio-mechanical interfaces, particularly those related to suction-based interfaces, for example, the contact interaction between residual limb and prosthetic socket. My research findings can directly benefit such applications and facilitate the development of improved devices.

6.2 Future Directions

Aside from the accomplishments delineated in preceding sections, I possess a noteworthy blueprint for forthcoming endeavors: the establishment of a design framework tailored for suction cups, intertwined with the infusion of bio-inspired attributes to fulfill the stipulated performance benchmarks. This scheme entails harnessing my investigatory revelations and proficiencies to formulate a comprehensive and methodical approach to suction cup design, seamlessly integrating the principles of biomimicry. By gleaning insights from the adhesive traits and mechanisms that various species have evolved to attain a symbiotic relationship with other participants, there exist avenues to extract novel design concepts and envision a redefined morphological paradigm for suction cups. Through this approach, I aim to develop suction cups that are more effective, efficient, and comfortable for the biological host. Ultimately, this work could have important implications for a wide range of applications, from biomedical devices to robotics and beyond.

6.2.1 Existing Bio-inspired Adhesive Devices

Previous research has explored bio-inspired attachment features from various organisms, such as insects [128], spiders [129], snails [130], clingfishes [131], octopus [132, 133, 134, 135, 136, 137], and and remora fish [138, 139, 140, 141], to enhance attachment or translation between two interfaces or to improve artificial suction cup performances. However, these studies tend to focus on replicating biological features or building robots that mimic the locomotion of animals, and are often based solely on morphological observations. Therefore, with my background as a mechanical engineer, I would like to fill the gaps between the straightforward replica versus engineering interpretation of these biological features.

6.2.2 Design Framework for Suction Cup

Suction cup performance is highly correlated to the properties of the substrate. The integument - suction cup should be considered as a coupled system and investigated as an integrated unit.

To enhance cup performance for bio-logging tags and reduce animal discomfort, a design matrix can be employed to customize cup design features for the specific type of cetacean integument and loading conditions induced by animal locomotion. The following three tasks serve as the basis for the suction cup design matrix:

Task 1: Formulate a framework for the suction cup design problem based on the coupled suction-integument system. This involves creating a comprehensive and systematic approach to designing suction cups that takes into account the unique properties of cetacean integument, the forces experienced during animal locomotion, and the specific requirements for bio-logging tag attachment. This framework should provide a clear road map for optimizing suction cup design and evaluating performance.

Task 2: Investigate bio-inspired suction cup design features for improved performance. Drawing on the principles of biomimicry, this task involves researching natural mechanisms and structures that could be adapted to enhance suction cup performance, such as the suction cups on octopus tentacles or the adhesive pads on gecko feet. The goal is to identify promising design features that could be incorporated into the suction cup framework.

Task 3: Design and fabricate bio-inspired suction cup prototypes using the proposed framework, and conduct a quantitative comparison with the traditional engineering suction cups currently used with bio-logging tags. This task involves using the framework and bio-inspired design features to create working suction cup prototypes that can be tested in laboratory and field conditions. The performance of these prototypes should be compared with

existing suction cups to evaluate their effectiveness and identify areas for further improvement.

6.3 Proposal

To design bio-inspired suction cups for use with bio-logging tags, I propose to tackle the potential biological feature from an engineering perspective. Instead of replicating biological features in a straightforward matter, I suggest linking specific attributes from the animals to corresponding engineered components of the suction cups. This approach would allow us to better understand how these attributes contribute to the overall performance of the suction cups, and how they can be optimized for specific applications.

More importantly, I also propose that the suction cups remain passive devices, meaning that they do not require any active control or manipulation. This is because passive suction cups are more practical and cost-effective for use in field studies with live animals. By using a combination of bio-inspired attributes and engineering design principles, we can create suction cups that are optimized for use with bio-logging tags and are effective, reliable, and comfortable for the animals.

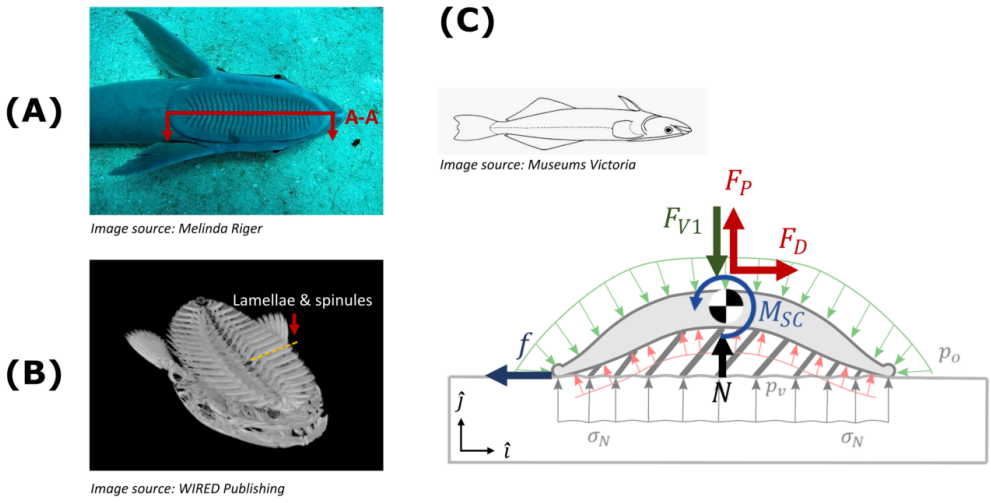

Figure 6.2: Remoras (Family: *Echeneidae*). (A) Top view of a remora's dorsal fin, which is evolved into a suction disc; (B) Skeleton of a remora, with the bony lamellae and spiky spinules inside the dorsal fin being highlighted; (C) The FBD of the suction disc with the remora heading to the right and being upside-down.

6.3.1 Bio-inspired Features Identification

Among the many animals that use suction for attachment, the remoras (Family: *Echeneidae*) were chosen by our research team as the inspirations of the bio-inspired suction cup designs. Remoras (Family: *Echeneidae*) maintain attachment to fast-swimming hosts, for example: sharks, whales and dolphins [142, 143, 144, 145, 146, 147], which is exactly what the bio-logging tags are doing. Remoras do so by using an adhesive suction disc. The adhesive disc has a soft tissue lip to control vacuum, and the bony lamellae with spinules to regulate friction force [139] (Figure 6.2 (B)).

Figure 6.2 (C) showcases the schematic of remora suction disc of section A-A (Figure 6.2 (A)). In this FBD, a remora fish secures itself upside-down to the integument of the host, with its' head pointing to the right. The remora suction disc and suction cups on bio-logging tag function in a comparable manner, as such, the modeling and testing approaches illustrated in Chapter 4 can be applied to this biological system. There are two major differences between the two systems. First, remora can actively regulate friction coefficients ($\mu_{s,d}$) and normal force (N) via rotating the lamellae - spinules structures. Second, remora can adjust the amount of water expelling from the suction disc to control the pressure inside the disc. These two features enable a remora fish to use a lower pressure differential (ΔP) to resist external loading. On the contrary, the artificial suction cup we used is a passive system, and therefore requires a higher initial setup pressure differential ($\Delta P_{int}\uparrow$) to address leakage in the system which comes with the higher risk of inducing discomfort and disturbing animal behaviors.

6.3.2 Remora - inspired Suction cup

Based on the features observed on remoras's disc (Family: *Echeneidae*), my first bio-inspired suction cup prototypes will be focusing on three decision variables. First, lip microstructure, finding out how to improve the contact condition between suction cup and cetacean integument so as to increase contact coefficients ($\mu_{s,d}$) as well as the normal force (N). Second is area, comparing the area ratio ($\frac{A_v}{A_c}$) between remora disc and artificial suction cup, and determining the range that will benefit the system in resisting external loading. Third is suction cup material, figuring out the correlation of material properties between suction cup and cetacean skin, in order for the system to generates a moderate initial setup pressure differential (ΔP_{int}) which won't disturb the animals and also maintains a relatively stable pressure differential (ΔP) under the general loading condition for the desired length of time.

It is promising that the bio-inspired suction cup design, guided by a proper design framework, can address the critical challenges in device design for bio-mechanical interfaces. However, it is important to conduct comprehensive testing and evaluation of the proposed design before drawing any firm conclusions. Further research and development may be required to fully optimize the

design and ensure its practicality and effectiveness.

6.3.3 Formulate the Suction Cup Design Framework and Design Matrix

The interaction between cetacean integument and suction cup is a complex system that involves both biological and mechanical components. Therefore, a comprehensive design process for suction cups should take into account the interactions between these components, as well as their properties and behaviors. The design process should also consider the specific requirements of the application, such as the species of animal, the attributes of surface to which the suction cup will be attached, and the expected loading conditions. By taking a holistic approach to the design process, it is likely to optimize the performance of suction cups for bio-logging tags and minimize any negative impact on the animals.

The suction design framework I proposed is presented in Figure 6.3, and consists of three blocks connected by the design matrix:

- Outputs X_j: contain measurable values from the failure mode tests, including initial setup pressure differential (ΔP_{int}), pressure differential change rate ($\dot{\Delta P}$), time constant of leakage (τ_{leak}), and the force (F_P, F_D) and moment (M_{SC}) that a suction cup can resist. Outputs are criteria used to quantify suction cup performances based on the generalized suction cup model introduced in Session 4.2.1, and are functions of decision variables and parameters ($X_j(Y, \Theta)$).

- Decision variables (Y): refer to the design factors of a suction cup which can be adjusted to have an impact on the output. Examples are material properties (k_{SC}^L, k_{SC}^R), areas (A_c, A_v), overall geometry, and lip microstructure... to name just a few. The decision variables of a suction cup should be adjusted based on its' working environment and the targeted animals, therefore decision variables are functions of parameters ($Y(\Theta)$).

- Parameters (Θ): these are the inputs to the system, and depend on features associated with the animal, such as skin properties, epidermis features, performance envelope defined by the hydrodynamic forces acting on the tag as it moves through the water on an animal and the overall environment.

Using these blocks, I proposed a suction cup design matrix ($L(Y, \Theta)$) in the form of a loss function which is the weighted sum of the outputs (Eq. 6.1). The decision variables will be

selected to minimize the loss function (Eq. 6.2).

$$L(Y, \Theta) = \sum_j w_j X_j(Y, \Theta) \tag{6.1}$$

$$Y(\Theta) = arg \min_{Y(\Theta)} \; L(Y, \Theta) \tag{6.2}$$

with w_j being the weighting of the corresponding output, X_j.

In essence, subjecting suction cup designs to comprehensive failure testing emerges as a pivotal stride within the design process. This strategic approach serves to unravel the utmost significance of each decision variable and culminate in a refined design matrix. Through the systematic assessment of failure modes in suction cups, the paramount design attributes governing their performance - encompassing cup dimensions, configuration, suction count, and material traits - become unequivocally evident.

Such discernment is invaluable, equipping designers to judiciously allocate weights to individual design variables within the matrix. This judicious allocation ensures that critical variables garner the meticulous attention they warrant throughout the design trajectory. A virtuous cycle of iterative testing and meticulous refinement thus ensues, heralding the emergence of meticulously tailored suction cup designs. This precision craftsmanship finds its zenith in applications as intricate as bio-logging tags for marine giants, exemplifying the potential for optimization and innovation that this comprehensive approach can yield.

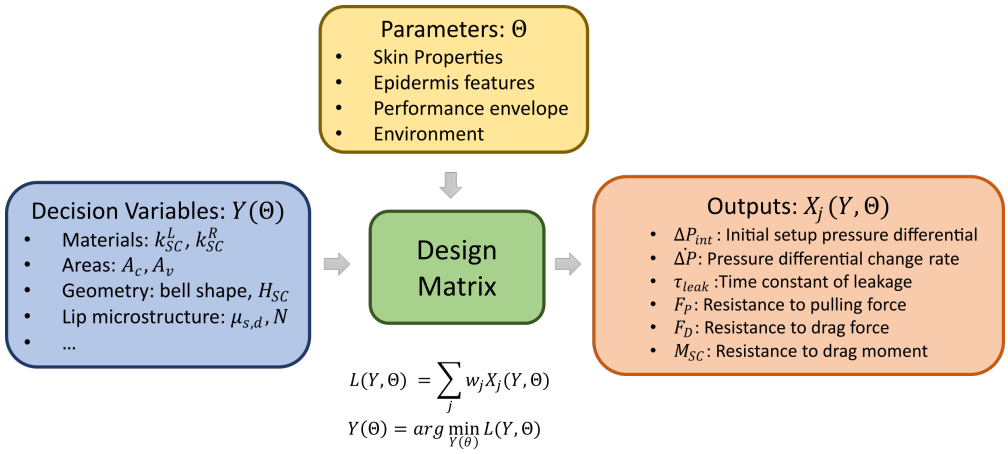

Figure 6.3: The proposed suction cup design framework consists of three blocks, which are - decision variables ($Y\Theta$), parameters (Θ) and outputs ($X_j(Y, \Theta)$), connected by the design matrix ($L(Y, \Theta)$).

APPENDIX A

PDIC Execution Code

```
int val_pin = 9;
int cam_pin = 6;
int buttonPin = 12;
unsigned long t = 0;
unsigned long stept = 35000;
unsigned long rampt = 10000;
unsigned long freq = 500;
unsigned long PressureTimer = 0;
unsigned long CameraTimer = 0;
float RefPressure = 0;
//float PressureArray[9]={0,-0.05, -0.1, -0.2, -0.3, -0.2, -0.1,
   -0.05, 0};
//float PressureArray[9]={0,-0.035, -0.07, -0.105, -0.14, -0.105,
    -0.07, -0.035, 0};
float PressureArray[9]={0, -0.025, -0.05, -0.075, -0.1, -0.075,
   -0.05, -0.025, 0};


float pressure_bar;
float volt;
float bits;
int PressureIndex = 0;
//float thres = 0.001;
bool start;
int count = 0;

```

```
24
25
26 void setup() {
27
28   //Pressure sensor
29   Serial.begin(9600);
30   //Air valve
31   pinMode (val_pin, OUTPUT);
32   digitalWrite (val_pin, LOW); //release, connect to air
33   //Cameras
34   pinMode(cam_pin, OUTPUT);
35   //digitalWrite (cam_pin, LOW); //off, not triggered
36   //Button
37   pinMode(buttonPin, INPUT);
38   start = false;
39   //Clock
40   t = millis();
41   PressureTimer = t;
42   PressureIndex = 0;
43   CameraTimer = t;
44   freq = 500;
45   count = 0;
46
47 }
48
49 float measure(){
50
51
52   float sensorVal = analogRead(A0);
53   //Serial.print("Sensor Value: ");
54   //Serial.print(sensorVal);
55   //Serial.print("\t");
56   float voltage = (sensorVal*5.0)/1023.0;
57   //Serial.print(" Volts: ");
58   //Serial.print(voltage);
59   //Serial.print("\t");
```

```
  float p = (voltage-0.5)*1.2/4-0.6; //New PT
  //float p = (0.3*((float)voltage-0.495))*1e1;//Old PT
  return p;

  }

void loop() {

  t = millis();//loop start time
  if (digitalRead(buttonPin) == HIGH && !start){
    start = true;
    PressureTimer = t;//set to loop start time
    CameraTimer = t;//set to loop start time
  }


  if (start){

    t = millis();//update clock

    //Pressure

    Serial.print(t); // ms
    Serial.print("\t");
    Serial.print(PressureTimer);
    Serial.print("\t");
    pressure_bar = measure();
    Serial.print(pressure_bar,5);//check point 1
    Serial.print("\t");
    Serial.print(RefPressure,5);//check point 2
    Serial.print("\t");
    Serial.print(PressureArray[PressureIndex]);//check point 3
    Serial.print("\t");
    //Air valve control
    if (pressure_bar < RefPressure){
```

```
95        digitalWrite (val_pin, LOW); //release, connects to
              atmosphere
96      }
97      else{
98        digitalWrite (val_pin, HIGH); //close, connects to pump
99      }
100
101     //Camera control (Trigger at H)
102     if (t - CameraTimer >= freq){
103       CameraTimer = t;//reset camera timer
104       count = count + 1;
105       //Serial.println(count);
106       if (count%2 == 1) {
107         digitalWrite (cam_pin, LOW);
108         //Serial.println("L");
109       }
110       else {
111         digitalWrite (cam_pin, HIGH);
112         //Serial.println("H");
113       }
114     }
115
116     //Pressure profile
117
118     if(t - PressureTimer <= stept ){
119       RefPressure = PressureArray[PressureIndex];
120       Serial.println("holding");
121     }
122
123     if(stept <(t - PressureTimer) && (t - PressureTimer)<= (stept
          +rampt)){
124       if (PressureIndex < 7){
125         RefPressure = PressureArray[PressureIndex]+(PressureArray
              [PressureIndex+1]-PressureArray[PressureIndex])*(t-(
              PressureTimer+stept))/rampt;
126       }
```

```
127       else{
128         RefPressure = PressureArray[PressureIndex];
129       }
130       Serial.println("ramping");
131     }
132 
133     if (t - PressureTimer > (stept+rampt)){
134       Serial.println("switch");
135       if (PressureIndex < 8){
136         PressureTimer = t;//reset pressure timer
137         PressureIndex = PressureIndex + 1;
138         RefPressure = PressureArray[PressureIndex];
139       }
140       else {
141         digitalWrite (val_pin, LOW);//release, connect to air
142         digitalWrite (cam_pin, LOW);//turn off camera
143         exit(0);
144       }
145     }
146 
147   }
148 
149 }
```

APPENDIX B

Pressure Differential Logging Code

```
#include <Honeywell_ABP.h>

// create Honeywell_ABP instance
Honeywell_ABP abp(
    0x28,    // I2C address
    -1,       // minimum pressure
    1,       // maximum pressure
    "bar"    // pressure unit
);

int buttonPin = 7;
int countnumber = 0;
float avg_init_p_bar;
float pressure_bar;
bool hold;
bool readSensor;
unsigned long t_zero = 0;
unsigned long t = 0;

void setup() {

  pinMode(buttonPin, INPUT);
  t = millis();
  hold = false;
  readSensor = false;
  countnumber = 0;
```

```
27
28    // open serial communication
29    Serial.begin(9600);
30    // open I2C communication
31    Wire.begin();
32  }
33
34  void loop(){
35
36    if (digitalRead(buttonPin) == HIGH && !hold){
37      readSensor = !readSensor;
38      hold = true;
39      countnumber = countnumber + 1;
40      //Serial.println(countnumber);
41
42      if (countnumber <= 9){
43        float j = countnumber/2;
44        int k = (int)j + 1;
45        String text1 = "Initial␣Average␣Pressure␣(bar)␣␣Check";
46        String text2 = text1 + k + ":␣";
47        Serial.println(text2);
48        avg_init_p_bar = measure_initial();
49        Serial.println(avg_init_p_bar,5);
50        countnumber = countnumber + 1;
51        readSensor = !readSensor;
52      }
53      if (countnumber == 11){
54        Serial.println("Start␣Measuring␣(bar):");
55        t_zero = millis();
56      }
57    }
58
59    if (digitalRead(buttonPin) == LOW && hold) {
60      hold = false;
61    }
62
```

```
63    if (readSensor && countnumber >= 11) {
64      t = millis() - t_zero;
65      pressure_bar = measure();
66      Serial.print(t);
67      Serial.print("␣");
68      Serial.print(pressure_bar,5);
69      Serial.println();
70    }
71
72  }
73
74  float measure() {
75      // update sensor reading
76      abp.update();
77      float p = abp.pressure();
78      return p;
79    }
80
81  float measure_initial() {
82      float p_sum = 0;
83
84      for(int i=0; i < 5; i++){
85      float p = measure();
86      //Serial.println (p);
87      p_sum = p_sum + p;
88      }
89      float p_avg = p_sum/5;
90      return p_avg;
91    }
```

APPENDIX C

Pressure Tag Execution Code

```
#include <Wire.h>
#include "MS5837.h"
MS5837 sensor_0;
MS5837 sensor_1;
MS5837 sensor_2;
MS5837 sensor_3;

#include <Adafruit_Sensor.h>
#include <Adafruit_BNO055.h>
#include <utility/imumaths.h>
Adafruit_BNO055 bno = Adafruit_BNO055(55, 0x28);

#include <SPI.h>
#include <SD.h>
File myFile;
float myTime;
unsigned long triallength = 86500; //11000; //21600;// 86500(s)

//int pinLED = 4;
//bool stateLED = false;
///* LED */
//void blinkLED() {
//  stateLED = !stateLED;
//  if (stateLED) digitalWrite(pinLED, HIGH);
//  else digitalWrite(pinLED, LOW);
//}
```

```
27
28 /* Setup I2C Hub */
29 #define TCAADDR 0x70
30   void tcaselect(uint8_t i) {
31     if (i > 7) return;
32     Wire.beginTransmission(TCAADDR);
33     Wire.write(1 << i);
34     Wire.endTransmission();
35   }
36
37 /* Read Pressure Data */
38   void read_save_pressure(MS5837 s, int tsa_port, String n) {
39     tcaselect(tsa_port);
40     s.read();
41     myFile.print(n);
42     myFile.print(": ");
43     myFile.print(s.pressure());
44     myFile.print(" ");
45     Serial.print(n);
46     Serial.print(": ");
47     Serial.print(s.pressure());
48     Serial.print(" ");
49   }
50
51 /* Save IMU Data */
52   void save_IMU(sensors_event_t* event) {
53      double x = -1000000, y = -1000000 , z = -1000000;
54      if (event->type == SENSOR_TYPE_LINEAR_ACCELERATION) {
55        Serial.print(" LinAccl: ");
56        myFile.print(" LinAccl: ");
57        x = event->acceleration.x;
58        y = event->acceleration.y;
59        z = event->acceleration.z;
60        myFile.print(x);
61        myFile.print(" ");
62        myFile.print(y);
```

```
63        myFile.print("␣");
64        myFile.print(z);
65        myFile.print("␣");
66        Serial.print(x);
67        Serial.print("␣");
68        Serial.print(y);
69        Serial.print("␣");
70        Serial.print(z);
71        Serial.print("␣");
72      }
73      else if (event->type == SENSOR_TYPE_GRAVITY) {
74        Serial.print("␣Gravity:␣");
75        myFile.print("␣Gravity:␣");
76        x = event->acceleration.x;
77        y = event->acceleration.y;
78        z = event->acceleration.z;
79        myFile.print(x);
80        myFile.print("␣");
81        myFile.print(y);
82        myFile.print("␣");
83        myFile.print(z);
84        myFile.print("␣m^2/s");
85        Serial.print(x);
86        Serial.print("␣");
87        Serial.print(y);
88        Serial.print("␣");
89        Serial.print(z);
90        Serial.print("␣m^2/s");
91      }
92      else if (event->type == SENSOR_TYPE_GYROSCOPE) {
93        Serial.print("␣Gyro:␣");
94        myFile.print("␣Gyro:␣");
95        x = event->gyro.x;
96        y = event->gyro.y;
97        z = event->gyro.z;
98        myFile.print(x);
```

```
99          myFile.print("␣");
100         myFile.print(y);
101         myFile.print("␣");
102         myFile.print(z);
103         myFile.print("␣rps");
104         Serial.print(x);
105         Serial.print("␣");
106         Serial.print(y);
107         Serial.print("␣");
108         Serial.print(z);
109         Serial.print("␣rps");
110       }
111       else if (event->type == SENSOR_TYPE_MAGNETIC_FIELD) {
112         Serial.print("␣Mag:␣");
113         myFile.print("␣Mag:␣");
114         x = event->magnetic.x;
115         y = event->magnetic.y;
116         z = event->magnetic.z;
117         myFile.print(x);
118         myFile.print("␣");
119         myFile.print(y);
120         myFile.print("␣");
121         myFile.print(z);
122         myFile.println("␣uT");
123         Serial.print(x);
124         Serial.print("␣");
125         Serial.print(y);
126         Serial.print("␣");
127         Serial.print(z);
128         Serial.println("␣uT");
129       }
130
131   }
132
133 /* Setup communication & initialize SD and sensors */
134   void setup() {
```

```
135 //    pinMode(pinLED, OUTPUT);
136
137     Wire.begin();
138     //rtc.begin();
139     Serial.begin(9600);
140
141     /* Initialise SD */
142     Serial.println("Initializing␣SD␣card...");
143     if (!SD.begin(8)) {
144       Serial.println("initialization␣failed!");
145       while (1);
146     }
147     Serial.println("SD␣card␣initialization␣is␣done.");
148
149     /* Initialise IMU */
150     Serial.println("Initializing␣IMU...");
151     tcaselect(4);
152     while (!bno.begin()){
153     Serial.println("BNO055␣Init␣failed!");
154     Serial.print("Ooops,␣no␣BNO055␣detected!");
155     Serial.println("\n");
156     delay(500);
157     }
158
159       Serial.println("IMU␣initialization␣is␣done.");
160       delay(500);
161
162     /* Initialise the 1st sensor */
163       tcaselect(0);
164       while (!sensor_0.init()) {
165         Serial.println("Init␣failed!");
166         Serial.println("Are␣SDA/SCL␣connected␣correctly?");
167         Serial.println("Blue␣Robotics␣Bar30:␣White=SDA,␣Green=SCL
              ");
168         Serial.println("\n");
169         delay(500);
```

```
170         }
171          sensor_0.setModel(MS5837::MS5837_30BA);
172          sensor_0.setFluidDensity(997); // kg/m^3 (1.225 for air,
                997 freshwater, 1029 for seawater)
173          //myFile.println("Sensor 1 initialization completed.");
174          Serial.println("Sensor 1 initialization completed.");
175          delay(500);
176
177        /* Initialise the 2nd sensor */
178         tcaselect(3);
179         while (!sensor_1.init()) {
180           Serial.println("Init failed!");
181           Serial.println("Are SDA/SCL connected correctly?");
182           Serial.println("Blue Robotics Bar30: White=SDA, Green=SCL
                ");
183           Serial.println("\n");
184           delay(500);
185         }
186          sensor_1.setModel(MS5837::MS5837_30BA);
187          sensor_1.setFluidDensity(997); // kg/m^3 (1.225 for air,
                997 freshwater, 1029 for seawater)
188          //myFile.println("Sensor 2 initialization completed.");
189          Serial.println("Sensor 2 initialization completed.");
190          delay(500);
191
192        /* Initialise the 3rd sensor */
193         tcaselect(6);
194         while (!sensor_2.init()) {
195           Serial.println("Init failed!");
196           Serial.println("Are SDA/SCL connected correctly?");
197           Serial.println("Blue Robotics Bar30: White=SDA, Green=SCL
                ");
198           Serial.println("\n");
199           delay(500);
200         }
201          sensor_2.setModel(MS5837::MS5837_30BA);
```

```
202         sensor_2.setFluidDensity(997); // kg/m^3 (1.225 for air,
                997 freshwater, 1029 for seawater)
203         //myFile.println("Sensor 3 initialization completed.");
204         Serial.println("Sensor␣3␣initialization␣completed.");
205         delay(500);
206
207       /* Initialise the 4th sensor */
208         tcaselect(7);
209         while (!sensor_3.init()) {
210           Serial.println("Init␣failed!");
211           Serial.println("Are␣SDA/SCL␣connected␣correctly?");
212           Serial.println("Blue␣Robotics␣Bar30:␣White=SDA,␣Green=SCL
                ");
213           Serial.println("\n");
214           delay(500);
215         }
216         sensor_3.setModel(MS5837::MS5837_30BA);
217         sensor_3.setFluidDensity(997); // kg/m^3 (1.225 for air,
                997 freshwater, 1029 for seawater)
218         //myFile.println("Sensor 4 initialization completed.");
219         Serial.println("Sensor␣4␣initialization␣completed.");
220         delay(500);
221
222 }
223
224
225 /* Measure and record time, dP, Acc, and Gravity */
226   void loop() {
227     myTime = millis()/1000.0;
228     if (myTime <= triallength){ /*&& fmod(myTime,1)==0){*/
229
230     myFile = SD.open("N_1209.txt", FILE_WRITE);
231     Serial.print(myTime);
232     Serial.print("␣s␣");
233     myFile.print(myTime);
234     myFile.print("␣s␣");
```

```
235
236     /*Read & Save Pressure */
237     read_save_pressure(sensor_0, 0, "RF");
238     read_save_pressure(sensor_1, 3, "RR");
239     read_save_pressure(sensor_2, 6, "LR");
240     read_save_pressure(sensor_3, 7, "LF");
241     myFile.print("mbar ");
242     Serial.print("mbar ");
243     /*Read & Save IMU */
244     sensors_event_t  linearAccelData, gravityData, gyroData,
          magnetData;
245   tcaselect(4);
246   bno.getEvent(&linearAccelData, Adafruit_BNO055::
       VECTOR_LINEARACCEL);
247   bno.getEvent(&gravityData, Adafruit_BNO055::VECTOR_GRAVITY);
248   bno.getEvent(&gyroData, Adafruit_BNO055::VECTOR_GYROSCOPE);
249   bno.getEvent(&magnetData, Adafruit_BNO055::VECTOR_MAGNETOMETER)
       ;
250   save_IMU(&linearAccelData);
251   save_IMU(&gravityData);
252   save_IMU(&gyroData);
253   save_IMU(&magnetData);
254
255     myFile.close();
256 //    blinkLED();
257     //delay(1000);
258 }
259   }
```

APPENDIX D

Pressure Tag Data Transmission Code

```
import serial
import time
import tqdm

filename = 'H_1209.txt'
block_size = 512

ser = serial.Serial('COM9', 9800, timeout=15)

try:
    # Get size of file
    file_size_as_string = ser.readline()
    file_size = int(file_size_as_string)

    bytes_left = file_size
    print(bytes_left)

    # Set up the loading bar settings, allowing for printing B,
       KB, MB as needed while printing
    download_bar = tqdm.tqdm(
                      total = file_size,
                      desc = 'Downloading file...',
                      unit = 'B',
                      unit_scale = True,
                      unit_divisor = 1024,
                      leave = True)
```

```
26
27      #Get the start time of the file download
28      t_start = time.time()
29
30      # Write to the file
31      with open(filename, 'wb') as file:
32          while bytes_left > 0:
33              trans_size = min(block_size, bytes_left)
34              bytes_read = ser.read(trans_size)
35              bytes_written = file.write(bytes_read)
36              bytes_left -= bytes_written
37              download_bar.update(bytes_written)
38
39      # Get the end time
40      t_end = time.time()
41      print("File␣downloaded␣in␣{}␣seconds␣(Avg␣download␣speed␣{}␣
           KB/sec)".format(t_end-t_start, (file_size/(t_end-t_start))
           /1024))
42      ser.close()
43  except:
44      ser.close()
45      raise
```

BIBLIOGRAPHY

[1] Evolution of man (homo habilis). https://yoo.rs/evolution-of-man-homo-habilis. Accessed 22 Feb 2023. vii, 2

[2] D Francisci. The olynthus mill in the alps: New hypotheses from two unidentified millstones discovered in veneto region (italy). *Journal of Lithic Studies*, 7(3):20–p, Dec. 2020. vii, 2

[3] Armor. https://www.quora.com/What-is-the-easiest-plate-armor-to-be-made. Accessed 22 Feb 2023. vii, 2

[4] Steam engine. https://www.environmentandsociety.org/mml/steam-engine. Accessed 22 Feb 2023. vii, 2

[5] Falcon rocket. https://en.wikipedia.org/wiki/Falcon9. Accessed 22 Feb 2023. vii, 2

[6] Teeth aligner. https://www.byte.com/community/resources/aligners. Accessed 22 Feb 2023. vii, 3

[7] Plaster casting. https://www.springwise.com/innovation/health-wellbeing. Accessed 22 Feb 2023. vii, 3

[8] Prosthesis. https://m.indiamart.com/proddetail/carbon-fiber-prosthetic-leg. Accessed 22 Feb 2023. vii, 3

[9] Ear tag on livestock. https://www.pinterest.com/pin/bichinhos. Accessed 22 Feb 2023. vii, 3

[10] Horseshoe. https://www.thesprucepets.com/horseshoe. Accessed 22 Feb 2023. vii, 3

[11] Fishhook. https://www.sportfishingmag.com/techniques/bait. Accessed 22 Feb 2023. vii, 3

[12] Apple watch. https://www.amazon.com/Apple-Aluminum-Fitness. Accessed 22 Feb 2023. vii, 4

[13] Continuous glucose monitoring. https://www.medtronic-diabetes.com/cgm. Accessed 22 Feb 2023. vii, 4

[14] D Roetenberg, H Luinge, and P Slycke. Xsens mvn: Full 6dof human motion tracking using miniature inertial sensors. *Xsens Motion Technologies BV, Tech. Rep.*, 1:1–7, Apr. 2009. vii, 4

[15] Gait assessment. https://neurosoft.com/en/catalog/gait-assessment. Accessed 22 Feb 2023. vii, 4

[16] Koala with collar tag. https://lx-group.com.au/trackercollar. Accessed 22 Feb 2023. vii, 5

[17] Wolf with collar tag. https://oregonwild.org//collared-wolves. Accessed 22 Feb 2023. vii, 5

[18] Bat with tracker. https://www.theverge.com//bat-tracking-sensors. Accessed 22 Feb 2023. vii, 5

[19] Bird with tracker. https://www.bto.org/understanding-birds/articles. Accessed 22 Feb 2023. vii, 5

[20] Seal with non-invasive bio-logging tag. https://www.deutschlandfunk.de/bio-logging-wir-wollen. Accessed 22 Feb 2023. vii, 5

[21] Squid with non-invasive bio-logging tag. https://news.mongabay.com/2019/01/a-fitbit-for-squid. Accessed 22 Feb 2023. vii, 5

[22] Orca waering a suction cup bio-logging tag. https://www.huck.psu.edu/news/killer-whale-conservation. Accessed 22 Feb 2023. vii, 6

[23] Biologist attaching bio-logging tag with a pole. https://www.bbc.co.uk/programmes/studying-orca. Accessed 22 Feb 2023. vii, 6

[24] D K Wainwright, F E Fish, S Ingersoll, T M Williams, J St Leger, A J Smits, and G V Lauder. How smooth is a dolphin? the ridged skin of odontocetes. *Biology letters*, 15(7), Jul. 2019. vii, 8

[25] Sperm whale with sloughed skin. https://www.newscientist.com/article/sperm-whales-skin/. Accessed 22 Feb 2023. vii, 8

[26] A variety of suction cup designs. https://www.allvacindustries.com/vacuum-suction-cups/. Accessed 22 Feb 2023. viii, 11

[27] Egypt wooden toe. https://www.smithsonianmag.com/ancient-cairo-toe. Accessed 22 Feb 2023. xii, 87, 88

[28] C Tribolo, N Mercier, M Selo, H Valladas, J L Joron, J L Reyss, C Henshilwood, J Sealy, and R Yates. Tl dating of burnt lithics from blombos cave (south africa): further evidence for the antiquity of modern human behaviour. *Archaeometry*, 48(2):341–357, May. 2006. 1

[29] Z Jacobs, G A Duller, A G Wintle, and C S Henshilwood. Extending the chronology of deposits at blombos cave, south africa, back to 140 ka using optical dating of single and multiple grains of quartz. *Journal of Human Evolution*, 51(3):255–273, Sep. 2006. 1

[30] C S Henshilwood, F d'Errico, K L Van Niekerk, Y Coquinot, Z Jacobs, S E Lauritzen, M Menu, and R García-Moreno. A 100,000-year-old ochre-processing workshop at blombos cave, south africa. *Science*, 334(6053):219–222, Oct. 2011. 1

[31] Z Jacobs, E H Hayes, R G Roberts, R F Galbraith, and C S Henshilwood. An improved osl chronology for the still bay layers at blombos cave, south africa: further tests of single-grain dating procedures and a re-evaluation of the timing of the still bay industry across southern africa. *Journal of archaeological science*, 40(1):579–594, Jan. 2013. 1

[32] R Frankel. The olynthus mill, its origin, and diffusion: typology and distribution. *American Journal of Archaeology*, 107(1):1–21, Jan. 2003. 1

[33] C Rutz and G C Hays. New frontiers in biologging science. *Biologer Letters*, 5(3):289–292, Jun. 2009. 4

[34] H J Williams, L A Taylor, S Benhamou, A I Bijleveld, T A Clay, S de Grissac, U Demšar, H M English, N Franconi, A Gómez-Laich, and R C Griffiths. Optimizing the use of biologgers for movement ecology research. *Journal of Animal Ecology*, 89(1):186–206, Aug. 2020. 4

[35] M Hebblewhite and D T. Haydon. Distinguishing technology from biology: a critical review of the use of gps telemetry data in ecology. *Philosophical Transactions of the Royal Society B: Biological Sciences*, 365(1550):2303–2312, Jul. 2010. 4

[36] P Goulet, C Guinet, R Swift, P T Madsen, and M Johnson. A miniature biomimetic sonar and movement tag to study the biotic environment and predator-prey interactions in aquatic animals. *Deep Sea Research Part I: Oceanographic Research Papers*, 1(148):1–1, Jun. 2019. 4

[37] T M Brown and K Krishnamurthy. *Histology, Dermis*. StatPearls Publishing, Internet, 2022. 4, 8

[38] M Fedak, P Lovell, B McConnell, and C Hunter. Overcoming the constraints of long range radio telemetry from animals: getting more useful data from smaller packages. *Integrative and Comparative Biology*, 42(1):3–10, Feb. 2002. 4

[39] L Boehme, P Lovell, M Biuw, F Roquet, J Nicholson, S E Thorpe, M P Meredith, and M Fedak. Animal-borne ctd-satellite relay data loggers for real-time oceanographic data collection. *Ocean Science*, 5(4):685–695, Dec. 2009. 4

[40] C Ware, A W Trites, D A Rosen, and J Potvin. Averaged propulsive body acceleration (apba) can be calculated from biologging tags that incorporate gyroscopes and accelerometers to estimate swimming speed, hydrodynamic drag and energy expenditure for steller sea lions. *PloS one*, 11(6):e0157326, Jun. 2016. 4, 70

[41] K Yoda, Y Naito, K Sato, A Takahashi, J Nishikawa, Y Ropert-Coudert, M Kurita, and Y Le Maho. A new technique for monitoring the behaviour of free-ranging adelie penguins. *Journal of Experimental Biology*, 204(4):685–690, Feb. 2001. 4

[42] H J Williams, M D Holton, E L Shepard, N Largey, B Norman, P G Ryan, O Duriez, M Scantlebury, F Quintana, E A Magowan, and N J Marks. Identification of animal movement patterns using tri-axial magnetometry. *Movement ecology*, 5:1–4, Dec. 2017. 4

[43] D Godyń, P Herbut, and S Angrecka. Measurements of peripheral and deep body temperature in cattle–a review. *Journal of Thermal Biology*, 1(79):42–49, Janr. 2019. 4

[44] J M Nassar, S M Khan, S J Velling, A Diaz-Gaxiola, S F Shaikh, N R Geraldi, G A Torres Sevilla, C M Duarte, and M M Hussain. Compliant lightweight non-invasive standalone "marine skin" tagging system. *npj Flexible Electronics*, 2(1):13–13, May. 2018. 4

[45] H J Williams, E L Shepard, M D Holton, P A Alarcón, R P Wilson, and S A Lambertucci. Physical limits of flight performance in the heaviest soaring bird. *Proceedings of the National Academy of Sciences*, 117(30):17884–17890, Jul. 2020. 4

[46] J A Green. The heart rate method for estimating metabolic rate: review and recommendations. *Comparative Biochemistry and Physiology Part A: Molecular & Integrative Physiology*, 158(3):287–304, Mar. 2011. 4

[47] E S Bridge, J F Kelly, A Contina, R M Gabrielson, R B MacCurdy, and D W Winkler. dvances in tracking small migratory birds: a technical review of light-level geolocation. *Journal of Field Ornithology*, 84(2):121–137, Jun. 2013. 4

[48] D Cazau, J Bonnel, J Jouma'a, Y Le Bras, and C Guinet. Measuring the marine soundscape of the indian ocean with southern elephant seals used as acoustic gliders of opportunity. *Journal of Atmospheric and Oceanic Technology*, 34(1):207–223, Jan. 2017. 4

[49] S J Cooke, S G Hinch, M Wikelski, R D Andrews, L J Kuchel, Wolcott. T G, and P J Butler. Biotelemetry: a mechanistic approach to ecology. *Trends in ecology & evolution*, 19(6):334–343, Jun. 2004. 5, 37

[50] Y Ropert-Coudert and R P Wilson. Trends and perspectives in animal-attached remote sensing. *Frontiers in Ecology and the Environment*, 3(8):437–444, Oct. 2005. 5, 37

[51] M P Johnson and P L Tyack. A digital acoustic recording tag for measuring the response of wild marine mammals to sound. *IEEE journal of oceanic engineering*, 28(1):3–12, Apr. 2003. 5, 15, 16, 37

[52] M B Hanson and R W Baird. Dall's porpoise reactions to tagging attempts using a remotely-deployed suction-cup tag. *Marine Technology Society Journal*, 32(2):18–23, Jun. 1998. 5, 15, 37

[53] S K Hooker and R W Baird. Diving and ranging behaviour of odontocetes: a methodological review and critique. *Mammal Review*, 31(1):81–105, Mar. 2001. 5, 15, 37

[54] K V Kardong. *Vertebrates: Comparative Anatomy, Function, Evolution*. McGraw-Hill, New York, 2018. 8

[55] D A Pabst. Springs in swimming animals. *American Zoologist*, 36(6):723–735, Dec. 1996. 8, 16

[56] D A Pabst. Morphology of the subdermal connective tissue sheath of dolphins: a new fibre-wound, thin-walled, pressurized cylinder model for swimming vertebrates. *Journal of Zoology*, 238(1):35–52, Jan. 1996. 8, 16

[57] E O Carew, F W Cooke, J E Lemons, B D Ratner, I Vesely, and Vogle E. Bulk properties of materials. In B D Ratner, A S Hoffman, F J Schoen, and J E Lemons, editors, *Biomaterials science: an introduction to materials in medicine*, pages 25–32. Elsevier Academic Press, Amsterdam, Boston, 2nd edition, 2004. 8, 16, 36

[58] F E Fish and J J Rohr. Review of dolphin hydrodynamics and swimming performance. *Technical Report 1801, SPAWAR Systems Center, San Diego*, Aug. 1999. 9, 16, 37

[59] V V Pavlov. Dolphin skin as a natural anisotropic compliant wall. *Bioinspiration & biomimetics*, 1(2):31–40, Jul. 2006. 9, 16, 37

[60] E R Fitzgerald and J W Fitzgerald. Blubber and compliant coatings for drag reduction in water i. viscoelastic properties of blubber and compliant coating materials. *Materials Science and Engineering: C*, 2(4):209–214, Sep. 1995. 9, 16, 17, 37, 39

[61] N A Qureshi, G I Ali, T S Abushanab, A T El-Olemy, M S Alqaed, I S El-Subai, and A M Al-Bedah. History of cupping (hijama): a narrative review of literature. *Journal of integrative medicine*, 15(3):172–181, May. 2017. 10, 11

[62] M M Rutkowski, P J Smolinski, and M C Miller. The geometry of vacuum assisted interface adhesion: Resistance to axial moment. *Vacuum*, 83(5):869–872, Jan. 2009. 11, 16

[63] Dean M. Aslam and Girish D. Dangi. Design, fabrication and testing of a smart robotic foot. *Robotics and Autonomous Systems*, 51(2-3):207–214, 2005. 11, 16

[64] Yu Kuwajima, Hiroki Shigemune, Vito Cacucciolo, Matteo Cianchetti, Cecilia Laschi, and Shingo Maeda. Active suction cup actuated by electrohydrodynamics phenomenon. *IEEE International Conference on Intelligent Robots and Systems*, 2017:470–475, Sep. 2017. 11

[65] P Zhang, M Kamezaki, K Otsuki, Z He, H Sakamoto, and S Sugano. Development of a vacuum suction cup by applying magnetorheological elastomers for objects with flat surfaces. *IEEE/ASME International Conference on Advanced Intelligent Mechatronics, AIM*, 2020:777–782, Jul. 2020. 11

[66] T Miyake, Hidenori Ishihara, and Tatsuya Tomino. Vacuum-based wet adhesion system for wall climbing robots -lubricating action and seal action by the liquid. *2008 IEEE International Conference on Robotics and Biomimetics, ROBIO*, pages 1824–1829, Feb. 2009. 11, 16

[67] T S Aboushanab and S AlSanad. Cupping therapy: an overview from a modern medicine perspective. *Journal of acupuncture and meridian studies*, 11(3):83–87, Jun. 2018. 11

[68] A M Al-Bedah, T S Aboushanab, M S Alqaed, N A Qureshi, I Suhaibani, G Ibrahim, and M Khalil. Classification of cupping therapy: a tool for modernization and standardization. *Journal of Complementary and Alternative Medical Research*, 1(1):1–10, Jun. 2016. 11

[69] M Horning, R D Andrews, A M Bishop, P L Boveng, D P Costa, D E Crocker, M Haulena, M Hindell, A G Hindle, R R Holser, and S K Hooker. Best practice recommendations for the use of external telemetry devices on pinnipeds. *Animal Biotelemetry*, 7(1):1–7, Dec. 2019. 15

[70] D N Wiley, C J Zadra, A S Friedlaender, S E Parks, A Pensarosa, A Rogan, Shorter K Alex, J Urbán, and I Kerr. Deployment of biologging tags on free swimming large whales using uncrewed aerial systems. *Royal Society Open Science*, 10(4):221376, Apr. 2023. 15

[71] S Isojunno, K Aoki, C Curé, P H Kvadsheim, and P J Miller. Breathing patterns indicate cost of exercise during diving and response to experimental sound exposures in long-finned pilot whales. *Frontiers in physiology*, page 1462, 2018. 15

[72] G Mantriota and A Messina. Theoretical and experimental study of the performance of flat suction cups in the presence of tangential loads. *Mechanism and machine theory*, 46(5):607–617, May. 2018. 16

[73] B Bahr, Y Li, and M Najafi. Design and suction cup analysis of a wall climbing robot. *Computers & electrical engineering*, 22(3):193–209, May. 1996. 16

[74] J Liu, K Tanaka, L M Bao, and I Yamaura. Analytical modelling of suction cups used for window-cleaning robots. *Vacuum*, 80(6):593–598, Mar. 2006. 16

[75] T Miyake, H Ishihara, and M Yoshimura. Basic studies on wet adhesion system for wall climbing robots. *2007 IEEE/RSJ International Conference on Intelligent Robots and Systems*, pages 1920–1925, Oct. 2007. 16

[76] D Ge, T Matsuno, Y Sun, C Ren, Y Tang, and S Ma. Quantitative study on the attachment and detachment of a passive suction cup. *Vacuum*, 1(116):13–20, Jun. 2015. 16, 24

[77] P E Nachtigall. Glossary. In K M Kovacs, J G Thewissen, and B G Würsig, editors, *Encyclopedia of Marine Mammals*, page 1105. Academic Press, London, UK, 3rd edition, 2018. 16, 36

[78] C Pailler-Mattei, S Bec, and H Zahouani. In vivo measurements of the elastic mechanical properties of human skin by indentation tests. *Medical engineering & physics*, 30(5):599–606, Jun. 2008. 17, 39

[79] R Sanders. Torsional elasticity of human skin in vivo. *Pflügers Archiv.*, 342(3):255–260, Sep. 1973. 17, 39

[80] C Escoffier, J de Rigal, A Rochefort, R Vasselet, J L Lévêque, and P G Agache. Age-related mechanical properties of human skin: an in vivo study. *Journal of Investigative Dermatology*, 93(3):353–357, Sep. 1989. 17, 39

[81] K Nightingale, M S Soo, R Nightingale, and G Trahey. Acoustic radiation force impulse imaging: in vivo demonstration of clinical feasibility. *Ultrasound in medicine & biology*, 28(2):227–235, Feb. 2002. 17, 39

[82] J Bercoff, M Tanter, and M Fink. Supersonic shear imaging: a new technique for soft tissue elasticity mapping. *IEEE transactions on ultrasonics, ferroelectrics, and frequency control*, 51(4):396–409, Apr. 2004. 17, 39

[83] L Sandrin, B Fourquet, J M Hasquenoph, S Yon, C Fournier, F Mal, C Christidis, M Ziol, B Poulet, F. Kazemi, and M. Beaugrand. Transient elastography: a new noninvasive method for assessment of hepatic fibrosis. *Ultrasound in medicine & biology*, 29(12):1705–1713, Dec. 2003. 17, 39

[84] S Diridollou, F Patat, F Gens, L Vaillant, D Black, J M Lagarde, Y Gall, and M Berson. In vivo model of the mechanical properties of the human skin under suction. *Skin Research and technology*, 6(4):214–221, Nov. 2000. 17, 39

[85] A B Cua, K P Wilhelm, and H I Maibach. Elastic properties of human skin: relation to age, sex, and anatomical region. *Archives of Dermatological Research*, 282(5):283–288, Aug. 1990. 17, 39

[86] P Elsner, D Wilhelm, and H I Maibach. Mechanical properties of human forearm and vulvar skin. *British Journal of Dermatology*, 122(5):.607–614, May 1990. 17, 39

[87] J Weickenmeier, M Jabareen, and E Mazza. Suction based mechanical characterization of superficial facial soft tissues. *JJournal of biomechanics*, 48(16):4279–4286, Dec. 2015. 17, 39

[88] F M Hendriks, D Brokken, C W Oomens, D L Bader, and F P Baaijens. The relative contributions of different skin layers to the mechanical behavior of human skin in vivo using suction experiments. *Medical engineering & physics*, 28(3):259–266, Apr. 2006. 17, 39

[89] S L Evans and C A Holt. Measuring the mechanical properties of human skin in vivo using digital image correlation and finite element modelling. *The Journal of Strain Analysis for Engineering Design*, 44(5):337–345, Jul. 2009. 17, 39

[90] D Solav, K M Moerman, A M Jaeger, K Genovese, and H M Herr. Multidic: An open-source toolbox for multi-view 3d digital image correlation. *IEEE Access*, 6:30520–30535, Jun. 2018. 17, 39

[91] Y Takema, Y Yorimoto, M Kawai, and G Imokawa. Age-related changes in the elastic properties and thickness of human facial skin. *British Journal of Dermatology*, 131(5):641–648, Nov. 1994. 17, 39

[92] R S Wells. Learning from nature: bottlenose dolphin care and husbandry. *Zoo Biology: Published in affiliation with the American Zoo and Aquarium Association*, 28(6):635–651, Nov. 2009. 19

[93] R S Wells, H L Rhinehart, L J Hansen, J C Sweeney, F I Townsend, R Stone, D R Casper, M D Scott, A A Hohn, and T K Rowles. Bottlenose dolphins as marine ecosystem sentinels: developing a health monitoring system. *EcoHealth*, 1:246–254, Sep. 2004. 19

[94] N Özkaya, D Leger, D Goldsheyder, and M Nordin. *Fundamentals of biomechanics: equilibrium, motion, and deformation*. Springer, New Haven, 2016. 21

[95] M Nordin and V H Frankel. *Basic biomechanics of the musculoskeletal system*. Lippincott Williams & Wilkins, Philadelphia, PA, 2001. 24

[96] R S Lakes. *Viscoelastic materials*. Cambridge university press, Cambridge, UK, 2009. 24, 33

[97] J T Gabaldon, D Zhang, J Rocho-Levine, M J Moore, J Van der Hoop, K Barton, and Shorter K A. Tag-based estimates of bottlenose dolphin swimming behavior and energetics. *Journal of Experimental Biology*, 225(22):jeb244599, Nov. 2022. 33

[98] K A Shorter, Murray M M, M Johnson, M Moore, and L E Howle. Drag of suction cup tags on swimming animals: modeling and measurement. *Marine Mammal Science*, 30(2):726–746, Apr. 2014. 33, 70, 76

[99] M E Grear, M R Motley, S B Crofts, A E Witt, A P Summers, and P Ditsche. Mechanical properties of harbor seal skin and blubber- a test of anisotropy. *Zoology*, 126:137–144, Feb. 2018. 35

[100] D Y Yang, K A Shorter, M Moore, J Rocho-Levine, R Wells, K Barton, and M Johnson. In vivo viscoelastic properties of cetacean integument: an experimental characterization. *Marine Mammal Science*, 2023. 39

[101] M A Sutton, J J Orteu, and H Schreier. *Image correlation for shape, motion and deformation measurements: basic concepts, theory and applications*. Springer Science & Business Media, New York, 2009. 40

[102] S Diridollou, M Berson, V Vabre, D Black, B Karlsson, F Auriol, J M Gregoire, C Yvon, L Vaillant, Y Gall, and F Patat. An in vivo method for measuring the mechanical properties of the skin using ultrasound. *Ultrasound in medicine & biology*, 24(2):215–224, Feb. 1998. 40

[103] P Neto, M Ferreira, F Bahia, and P Costa. Improvement of the methods for skin mechanical properties evaluation through correlation between different techniques and factor analysis. *Skin Research and Technology*, 19(4):405–416, Nov. 2013. 40

[104] L Pedersen, B Hansen, and G B Jemec. Mechanical properties of the skin: a comparison between two suction cup methods. *Skin Research and Technology*, 9(2):111–115, May. 2003. 40

[105] G E Piérard, S Piérard, P Delvenne, and C Piérard-Franchimont. In vivo evaluation of the skin tensile strength by the suction method: pilot study coping with hysteresis and creep extension. *International Scholarly Research Notices*, Jul. 2013. 40

[106] H Dobrev. In vivo study of skin mechanical properties in raynaud's phenomenon. *Skin Research and Technology*, 13(1):91–94, Feb. 2007. 40

[107] International Digital Image Correlation Society, Jones, E M C and Iadicola, M A(Eds.). A good practices guide for digital image correlation. https://doi.org/10.32720/idics/gpg.ed1, 2018. 41

[108] A Pissarenko and M A Meyers. The materials science of skin: Analysis, characterization, and modeling. *Progress in Materials Science*, 110:100634, May. 2020. 43

[109] S D Łagan and A Liber-Kneć. Experimental testing and constitutive modeling of the mechanical properties of the swine skin tissue. *Acta of bioengineering and biomechanics*, 19(2):93–102, 2017. 43

[110] r R J Lapee, P D Gasson, and V Karri. Simulating plastic surgery: From human skin tensile tests, through hyperelastic finite element models to real-time haptics. *Progress in Biophysics and Molecular Biology*, 103(2-3):208–216, Dec. 2010. 43

[111] Y C Fung. Elasticity of soft tissues in simple elongation. *American Journal of Physiology-Legacy Content*, 213(6):1532–1544, Dec. 1967. 43

[112] P A Martins, R M Natal Jorge, and Ferreira A J. A comparative study of several material models for prediction of hyperelastic properties: Application to silicone-rubber and soft tissues. *Strain*, 42(3):135–147, Aug. 2006. 43

[113] R W Ogden. Large deformation isotropic elasticity–on the correlation of theory and experiment for incompressible rubberlike solids. *Proceedings of the Royal Society of London - A Mathematical and Physical Sciences*, 326(1567):565–584, Feb. 1972. 43

[114] M Mooney. A theory of large elastic deformation. *Journal of applied physics*, 11(9):582–592, Sep. 1940. 43

[115] N W Tschoegl. Representation of linear viscoelastic behavior by series-parallel models. In *The Phenomenological Theory of Linear Viscoelastic Behavior: An Introduction*, pages 69–156. Springer Berlin Heidelberg, Berlin, Heidelberg, 1989. 43

[116] J S Bergström and M C Boyce. Constitutive modeling of the large strain time-dependent behavior of elastomers. *Journal of the Mechanics and Physics of Solids*, 46(5):931–954, May. 1998. 43

[117] C M Zener and S Siegel. Elasticity and anelasticity of metals. *The Journal of Physical Chemistry*, 53(9):1468–1468, Sep. 1949. 44

[118] M A Meyers and K K Chawla. *Mechanical behavior of materials*. Cambridge university press, New York, 2008. 45

[119] L M Martín López, N Aguilar de Soto, P Miller, and M Johnson. Tracking the kinematics of caudal-oscillatory swimming: a comparison of two on-animal sensing methods. *Journal of Experimental Biology*, 219(14):2103–2109, Jul. 2016. 70

[120] K Aoki, Y Y Watanabe, D E Crocker, P W Robinson, M Biuw, D P Costa, N Miyazaki, M A Fedak, and P J Miller. Northern elephant seals adjust gliding and stroking patterns with changes in buoyancy: validation of at-sea metrics of body density. *Journal of experimental biology*, 214(17):2973–2987, Sep. 2011. 70

[121] P J Miller, M P Johnson, P L Tyack, and E A Terray. Swimming gaits, passive drag and buoyancy of diving sperm whales physeter macrocephalus. *Journal of Experimental Biology*, 207(11):1953–1967, May. 2004. 70

[122] D Zhang, J Gabaldon, L Lauderdale, M Johnson-Roberson, L J Miller, K Barton, and K A Shorter. Localization and tracking of uncontrollable underwater agents: Particle filter based fusion of on-body imus and stationary cameras. *In2019 International Conference on Robotics and Automation (ICRA), IEEE*, pages 6575–6581, May. 2019. 70

[123] B C Balmer, R S Wells, L E Howle, A A Barleycorn, W A McLellan, D Ann Pabst, T K Rowles, L H Schwacke, F I Townsend, A J Westgate, and E S Zolman. Advances in cetacean telemetry: A review of single-pin transmitter attachment techniques on small cetaceans and development of a new satellite-linked transmitter design. *Marine Mammal Science*, 30(2):656–673, Apr. 2014. 70

[124] A A Hazekamp, R Mayer, and N Osinga. Flow simulation along a seal: the impact of an external device. *European Journal of Wildlife Research*, 56(2):131–140, Apr. 2010. 70

[125] V V Pavlov and A M Rashad. A non-invasive dolphin telemetry tag: Computer design and numerical flow simulation. *Marine Mammal Science*, 28(1):E16–E27, Jan. 2012. 70

[126] J M van der Hoop, A Fahlman, T Hurst, J Rocho-Levine, K A Shorter, V Petrov, and M J Moore. Bottlenose dolphins modify behavior to reduce metabolic effect of tag attachment. *Journal of Experimental Biology*, 217(23):4229–4236, Dec. 2014. 70

[127] J M Van der Hoop, A Fahlman, K A Shorter, J Gabaldon, J Rocho-Levine, V Petrov, and M J Moore. Swimming energy economy in bottlenose dolphins under variable drag loading. *Frontiers in Marine Science*, 5:465, Dec. 2018. 70

[128] A Tsipenyuk and M Varenberg. Use of biomimetic hexagonal surface texture in friction against lubricated skin. *Journal of the Royal Society Interface*, 11(94):20140113, May. 2014. 89

[129] J O Wolff and S N Gorb. *Attachment Structures and Adhesive Secretions in Arachnids*. Springer Cham, Switzerland, 2016. 89

[130] B Chan, N J Balmforth, and A E Hosoi. Building a better snail: Lubrication and adhesive locomotion. *Physics of fluids*, 17(11):113101, Nov. 2005. 89

[131] P Ditsche and A Summers. Learning from northern clingfish (gobiesox maeandricus): bioinspired suction cups attach to rough surfaces. *Philosophical Transactions of the Royal Society B*, 374(1784):20190204, Oct. 2019. 89

[132] M K Choi, O K Park, C Choi, S Qiao, R Ghaffari, J Kim, D J Lee, M Kim, W Hyun, S J Kim, and H J Hwang. Cephalopod-inspired miniaturized suction cups for smart medical skin. *Advanced healthcare materials*, 5(1):80–87, Jan. 2016. 89

[133] S Baik, J Kim, H J Lee, T H Lee, and C Pang. Highly adaptable and biocompatible octopus-like adhesive patches with meniscus-controlled unfoldable 3d microtips for underwater surface and hairy skin. *Advanced Science*, 5(8):1800100, Aug. 2018. 89

[134] S Baik, H J Lee, D W Kim, J W Kim, Y Lee, and C Pang. Bioinspired adhesive architectures: from skin patch to integrated bioelectronics. *Advanced Materials*, 31(34):1803309, Aug. 2019. 89

[135] S Baik, H J Lee, D W Kim, H Min, and C Pang. Capillarity-enhanced organ-attachable adhesive with highly drainable wrinkled octopus-inspired architectures. *ACS applied materials & interfaces*, 11(29):25674–25681, Jun. 2019. 89

[136] S Chun, D W Kim, S Baik, H J Lee, J H Lee, S H Bhang, and C Pang. Conductive and stretchable adhesive electronics with miniaturized octopus-like suckers against dry/wet skin for biosignal monitoring. *Advanced Functional Materials*, 28(52):1805224, Dec. 2018. 89

[137] J H Oh, S Y Hong, H Park, S W Jin, Y R Jeong, S Y Oh, J Yun, H Lee, J W Kim, and J S Ha. Fabrication of high-sensitivity skin-attachable temperature sensors with bioinspired microstructured adhesive. *ACS applied materials & interfaces*, 10(8):7263–7270, Feb. 2018. 89

[138] Y Wang, X Yang, Y Chen, D K Wainwright, C P Kenaley, Z Gong, Z Liu, H Liu, J Guan, T Wang, and J C Weaver. A biorobotic adhesive disc for underwater hitchhiking inspired by the remora suckerfish. science robotics. *ACS applied materials & interfaces*, 2(10):eaan8072, Sep. 2017. 89

[139] K M Gamel, A M Garner, and B E Flammang. Bioinspired remora adhesive disc offers insight into evolution. *Bioinspiration & Biomimetics*, 14(5):056014, Aug. 2019. 89, 91

[140] S Su, S Wang, L Li, Z Xie, F Hao, J Xu, S Wang, J Guan, and L Wen. Vertical fibrous morphology and structure-function relationship in natural and biomimetic suction-based adhesion discs. *Matter*, 2(5):1207–1221, May. 2019. 89

[141] S Wang, L Li, W Sun, D Wainwright, H Wang, W Zhao, Y Chen, B amd Chen, and L Wen. Detachment of the remora suckerfish disc: kinematics and a bio-inspired robotic model. *Bioinspiration & Biomimetics*, 15(5):056018, Aug. 2020. 89

[142] E W Gudger. On the use of the sucking-fish for catching fish and turtles: Studies in echeneis or remora, ii. *The American Naturalist*, 53(628):446–467, Sep. 1919. 91

[143] D Weihs, F E Fish, and A J Nicastro. Mechanics of remora removal by dolphin spinning. *Marine mammal science*, 23(3):707–714, Jul. 2007. 91

[144] E H Williams Jr, A A Mignucci-Giannoni, L Bunkley-Williams, R K Bonde, C Self-Sullivan, A Preen, and V G Cockcroft. Echeneid–sirenian associations, with information on sharksucker diet. *Journal of Fish Biology*, 63(5):1176–1183, Nov. 2003. 91

[145] Á B Andrade. Echeneis naucrates (linnaeus)(perciformes, echeneidae), unusual interaction with a diver. *Pan-American Journal of Aquatic Sciences*, 2(1), 2007. 91

[146] J M Brunnschweiler and I Sazima. A new and unexpected host for the sharksucker (echeneis naucrates) with a brief review of the echeneid–host interactions. *Marine Biodiversity Records*, 1:e41, Jan. 2008. 91

[147] D Fertl and A M Landry Jr. Sharksucker (echeneis naucrates) on a bottlenose dolphin (tursiops truncatus) and a review of other cetacean-remora associations. *Marine Mammal Science*, 15(3):859–863, Jul. 1999. 91